

Overflow metabolism originates from growth optimization and cell heterogeneity

Xin Wang^{1*}

¹School of Physics, Sun Yat-sen University, Guangzhou 510275, China

*For correspondence: wangxin36@mail.sysu.edu.cn

Abstract

A classic problem in metabolism is that fast-proliferating cells use seemingly wasteful fermentation for energy biogenesis in the presence of sufficient oxygen. This counterintuitive phenomenon, known as overflow metabolism or the Warburg effect, is universal across various organisms. Despite extensive research, its origin and function remain unclear. Here, we show that overflow metabolism can be understood through growth optimization combined with cell heterogeneity. A model of optimal protein allocation, coupled with heterogeneity in enzyme catalytic rates among cells, quantitatively explains why and how cells choose between respiration and fermentation under different nutrient conditions. Our model quantitatively illustrates the growth rate dependence of fermentation flux and enzyme allocation under various perturbations and is fully validated by experimental results in *Escherichia coli*. Our work provides a quantitative explanation for the Crabtree effect in yeast and the Warburg effect in cancer cells and can be broadly used to address heterogeneity-related challenges in metabolism.

Introduction

A prominent feature of cancer metabolism is that tumor cells excrete large quantities of fermentation products in the presence of sufficient oxygen (Hanahan and Weinberg, 2011; Liberti and Locasale, 2016; Vander Heiden et al., 2009). This process, discovered by Otto Warburg in the 1920s (Warburg et al., 1924) and known as the Warburg effect, aerobic glycolysis, or overflow metabolism (Basan et al., 2015; Hanahan and Weinberg, 2011; Liberti and Locasale, 2016; Vander Heiden et al., 2009), is ubiquitous among fast-proliferating cells across a broad spectrum of organisms (Vander Heiden et al., 2009), ranging from bacteria (Basan et al., 2015; Holms, 1996; Meyer et al., 1984; Nanchen et al., 2006; Neidhardt et al., 1990) and fungi (De Deken, 1966) to mammalian cells (Hanahan and Weinberg, 2011; Liberti and Locasale, 2016; Vander Heiden et al., 2009). For microbes, cells use standard respiration when nutrients are scarce, while they use the counterintuitive aerobic glycolysis when nutrients are adequate, just analogous to normal tissues and cancer cells, respectively (Vander Heiden et al., 2009).

Over the past century, and particularly through extensive studies in the last two decades (Liberti and Locasale, 2016), various rationales for overflow metabolism have been proposed (Basan et al., 2015; Chen and Nielsen, 2019; Majewski and Domach, 1990; Molenaar et al., 2009; Niebel et al., 2019; Peebo et al., 2015; Pfeiffer et al., 2001; Shlomi et al., 2011; Vander Heiden et al., 2009; Varma and Palsson, 1994; Vazquez et al., 2010; Vazquez and Oltvai, 2016; Zhuang et al., 2011). Notably, Basan *et al.* (Basan et al., 2015) provided a systematic characterization of this process, including various types of experimental perturbations. Currently, prevalent explanations (Basan et al., 2015; Chen and Nielsen, 2019) hold that overflow metabolism arises from the proteome efficiency in fermentation being consistently higher than that in respiration. However, recent studies have shown that the measured proteome efficiency in respiration is actually higher than in fermentation for many yeast and cancer cells (Shen et al., 2024), even though these cells generate fermentation products through aerobic glycolysis. This finding (Shen et al., 2024) apparently contradicts the prevalent explanations (Basan et al., 2015; Chen and Nielsen, 2019). Furthermore, most explanations (Basan et al., 2015; Chen and Nielsen, 2019; Majewski and Domach, 1990; Shlomi et al., 2011; Varma and Palsson, 1994; Vazquez et al., 2010; Vazquez and Oltvai, 2016; Zhuang et al., 2011) rely on the assumption that cells optimize their growth rate for a given rate of carbon influx (i.e., nutrient uptake rate) under each nutrient condition (or its equivalents). However, this assumption remains open to further scrutiny, as the given factors in a nutrient condition are the identities and concentrations of the carbon sources (Molenaar et al., 2009; Scott et al., 2010; Wang et al., 2019), rather than the carbon influx. Therefore, the origin and function of overflow metabolism still remain unclear (DeBerardinis and Chandel, 2020; Hanahan and Weinberg, 2011; Liberti and Locasale, 2016; Vander Heiden et al., 2009).

Why have microbes and cancer cells evolved to possess the seemingly wasteful strategy of aerobic glycolysis? For unicellular organisms, there is evolutionary pressure (Vander Heiden et al., 2009) to optimize cellular resources for rapid growth (Dekel and Alon, 2005; Edwards et al., 2001; Hui et al., 2015; Li et al., 2018; Scott et al., 2010; Towbin et al., 2017; Wang et al., 2019;

You et al., 2013). In particular, it has been shown that cells allocate protein resources for optimal growth (Hui et al., 2015; Scott et al., 2010; Wang et al., 2019; You et al., 2013), and the most efficient protein allocation corresponds to elementary flux mode (Müller et al., 2014; Wortel et al., 2014). For cancer cells, disrupting the growth control system and evading immune destruction from the host are prominent hallmarks of their survival (Hanahan and Weinberg, 2011), which in certain ways mimic the evolutionary pressure on microbes to optimize cell growth rate. In this study, we apply the optimal growth principle of microbes, which also roughly holds for cancer cells, to a heterogeneous framework to address the puzzle of aerobic glycolysis. We use *Escherichia coli* as a typical example to show that overflow metabolism can be understood from optimal protein allocation combined with heterogeneity in enzyme catalytic rates. The optimal growth strategy varies between respiration and fermentation depending on the concentration and type of the nutrient, and the combination with cell heterogeneity results in the standard picture (Basan et al., 2015; Holms, 1996; Meyer et al., 1984; Nanchen et al., 2006; van Hoek et al., 1998) of overflow metabolism. Our model quantitatively illustrates the growth rate dependence of fermentation/respiration flux and enzyme allocation under various types of perturbations in *E. coli*. Furthermore, it provides a quantitative explanation for the data on the Crabtree effect in yeast and the Warburg effect in cancer cells (Bartman et al., 2023; Shen et al., 2024).

Results

Coarse-grained model

Based on the topology of the metabolic network (Neidhardt et al., 1990; Nelson et al., 2008) (see Fig. 1A), we classify the carbon sources that enter from the upper part of glycolysis into Group A (Wang et al., 2019) and the precursors of biomass components (such as amino acids) into five pools. Specifically, each pool is designated according to its entry point (see Fig. 1A and Appendix 1.2 for details): a1 (entry point: G6P/F6P), a2 (entry point: GA3P/3PG/PEP), b (entry point: pyruvate/acetyl-CoA), c (entry point: α -ketoglutarate), and d (entry point: oxaloacetate). Pools a1 and a2 are also combined as Pool a due to the joint synthesis of precursors. Then, the metabolic network for Group A carbon source utilization (see Fig. 1A) can be coarse-grained into a model shown in Fig. 1B (see Appendix 2.1 for details), where node A represents an arbitrary carbon source of Group A. Evidently, Fig. 1B is topologically identical to Fig. 1A. Each coarse-grained arrow in Fig. 1B represents a stoichiometric flux J_i , which delivers carbon flux and may be accompanied by energy consumption or biogenesis (e.g., J_1, J_{a1} , see Figs. 1A-B and Appendix-fig. 1A).

In fact, the stoichiometric flux J_i scales with the cell population. For comparison with experiments, we define the normalized flux $J_i^{(N)} \equiv J_i \cdot m_0 / M_{\text{carbon}}$, which can be regarded as the flux per unit of biomass (the superscript “(N)” stands for normalized; see Appendix 1.3-1.4 for details). Here, M_{carbon} represents the carbon mass of the cell population, and m_0 is the weighted average carbon mass of metabolite molecules at the entry of precursor pools (see Eq. S17). Then, the cell growth rate λ can be represented by the total outflow of the normalized fluxes:

$\lambda = \sum_i^{a1,a2,b,c,d} J_i^{(N)}$ (see Appendix 1.4). The normalized fluxes of respiration and fermentation are $J_r^{(N)} \equiv J_4^{(N)}$ and $J_f^{(N)} \equiv J_6^{(N)}$, respectively (see Fig. 1A-B). In practice, each $J_i^{(N)}$ is characterized by two quantities: the proteomic mass fraction ϕ_i of the enzyme dedicated to carrying the flux and the substrate quality κ_i , such that $J_i^{(N)} = \phi_i \cdot \kappa_i$. We take the Michaelis-Menten form for the enzyme kinetics (Nelson et al., 2008), and then $\kappa_i \equiv k_i \cdot \frac{[S_i]}{[S_i] + K_i}$ (see Eq. S12 and Appendix 1.4 for details), where $[S_i]$ is the concentration of substrate S_i , and K_i is the Michaelis constant. For each intermediate node and reaction along the pathway (e.g., node M_1 in J_{a1}), the substrate quality κ_i can be approximated as a constant (see Appendix 1.5): $\kappa_i \equiv k_i \cdot \frac{[S_i]}{[S_i] + K_i} \approx k_i$, where $[S_i] \geq K_i$ generally holds true in bacteria (Bennett et al., 2009; Park et al., 2016). However, the nutrient quality κ_A is a variable that depends on the nutrient type and concentration of a Group A carbon source (see Eq. S27).

Generally, there are three independent fates for a Group A carbon source in the metabolic network (Chen and Nielsen, 2019): fermentation, respiration, and biomass generation (see Appendix-fig. 1C-E). Each draws a distinct proteome fraction of ϕ_f , ϕ_r and ϕ_{BM} , with no overlap between them (see Appendix 2.1). The net effect of the first two fates is energy biogenesis, while the last one generates precursors for biomass, accompanied by energy biogenesis. By applying the proteomic constraint (Scott et al., 2010) that there is a maximum fraction ϕ_{max} for proteome allocation ($\phi_{\text{max}} \approx 0.48$ (Scott et al., 2010)), we have:

$$\phi_f + \phi_r + \phi_{\text{BM}} = \phi_{\text{max}}. \quad (1)$$

In fact, Eq. 1 is equivalent to $\phi_{\text{R}} + \phi_A + \sum_{j=1}^6 \phi_j + \sum_i^{a1,a2,b,c,d} \phi_i = \phi_{\text{max}}$ (see Appendix 2.1 for derivation details), where ϕ_{R} and ϕ_A represent the proteomic mass fractions of the active ribosome-affiliated proteins and the cargo proteins responsible for the uptake of the Group A carbon source, respectively. During cell proliferation, ribosomes serve as the factories for protein synthesis and are primarily composed of proteins (Neidhardt et al., 1990; Nelson et al., 2008), while other biomass components, such as RNA, are optimally produced (Kostinski and Reuveni, 2020) in accordance with the growth rate determined by protein synthesis. Thus, the cell growth rate is proportional to ϕ_{R} : $\lambda = \phi_{\text{R}} \cdot \kappa_t$, where κ_t is a parameter set by the translation rate (Scott et al., 2010) (see Appendix 1.1 for details), which can be approximated as a constant within the growth rate range of interest (Dai et al., 2017).

For balanced cell growth in bacteria, the energy demand J_E , expressed as the stoichiometric energy flux in ATP, is generally proportional to the biomass production rate (Ebenhöh et al., 2024), since the proportion of maintenance energy is roughly negligible (Locasale and Cantley, 2010) (see Appendix 9 for the cases of yeast and tumor cells). Thus, the normalized flux of energy demand in ATP, denoted as $J_E^{(N)}$, representing the energy demand per unit of biomass, is proportional to the growth rate λ (see Appendix 2.1 for details):

$$J_E^{(N)} = \eta_E \cdot \lambda, \quad (2)$$

where η_E is an energy coefficient (see Eqs. S25-S26 for details). By converting all energy currencies (such as NADH, FADH₂, etc.) into ATP, the normalized energy fluxes for respiration and fermentation are given by $J_r^{(E)} = \beta_r^{(A)} \cdot J_r^{(N)} / 2$ and $J_f^{(E)} = \beta_f^{(A)} \cdot J_f^{(N)} / 2$, where $\beta_r^{(A)}$ and $\beta_f^{(A)}$ are the stoichiometric coefficients of ATP production per glucose in each pathway (see Appendix-fig. 1C-E and Appendix 2.1 for details). The denominator coefficient of “2” is derived from the stoichiometry of the coarse-grained reaction $M_1 \rightarrow 2M_2$ (see Fig. 1A-B). Applying the criteria of flux balance (i.e., mass conservation; see Appendix 1.3) at each intermediate node (M_i , $i = 1, \dots, 5$) and precursor pool (Pool i , $i = a1, a2, b, c, d$), along with the constraints of proteome allocation (see Eq. 1) and energy demand (see Eq. 2), we obtain the relations between normalized energy fluxes and growth rate for a given nutrient condition with a fixed κ_A (see Appendix 2.1 for details):

$$\begin{cases} J_r^{(E)} + J_f^{(E)} = \varphi \cdot \lambda, \\ \frac{J_r^{(E)}}{\varepsilon_r} + \frac{J_f^{(E)}}{\varepsilon_f} = \phi_{\max} - \psi \cdot \lambda, \end{cases} \quad (3)$$

where φ is a constant coefficient primarily determined by the coefficient η_E (see Eq. S33), and $\varphi \cdot \lambda$ represents the normalized flux of energy demand, excluding energy biogenesis from the biomass synthesis pathway. The coefficients ψ , ε_r and ε_f are functions of κ_A , such that their values are highly dependent on nutrient conditions. ψ^{-1} denotes the proteome efficiency for biomass generation in the biomass synthesis pathway (see Eq. S32), defined as $\psi^{-1} \equiv \lambda / \phi_{\text{BM}}$ (see Appendix 2.1). ε_r and ε_f represent the proteome efficiencies for energy biogenesis in the respiration and fermentation pathways, respectively, defined as the normalized energy fluxes expressed in ATP generated per proteomic mass fraction, with $\varepsilon_r \equiv J_r^{(E)} / \phi_r$ and $\varepsilon_f \equiv J_f^{(E)} / \phi_f$. Hence,

$$\begin{cases} \varepsilon_r = \frac{\beta_r^{(A)}}{1/\kappa_A + 1/\kappa_r^{(A)}}, \\ \varepsilon_f = \frac{\beta_f^{(A)}}{1/\kappa_A + 1/\kappa_f^{(A)}}, \end{cases} \quad (4)$$

where both $\kappa_r^{(A)}$ and $\kappa_f^{(A)}$ are composite parameters that can be approximated as constants, with $1/\kappa_r^{(A)} \equiv 1/\kappa_1 + 2/\kappa_2 + 2/\kappa_3 + 2/\kappa_4$ and $1/\kappa_f^{(A)} \equiv 1/\kappa_1 + 2/\kappa_2 + 2/\kappa_6$ (see Appendices 1.5 and 2.1 for details).

Origin of overflow metabolism

The standard picture of overflow metabolism (Basan et al., 2015; Holms, 1996; Meyer et al., 1984; Nanchen et al., 2006; van Hoek et al., 1998) is exemplified by the experimental data (Basan et al., 2015) presented in Fig. 1C, where the fermentation flux exhibits a threshold-analog dependence on the growth rate λ . It is well established that respiration is significantly more efficient than fermentation in terms of energy biogenesis per unit of carbon (i.e., $\beta_r^{(A)} > \beta_f^{(A)}$) (Nelson et al., 2008; Vander Heiden et al., 2009). Then, why do cells bother to use the seemingly wasteful fermentation pathway? We proceed to address this issue by applying optimal protein allocation (Scott et al., 2010; Wang et al., 2019) within the framework of optimal growth.

For cell proliferation in a given nutrient condition (i.e., with a fixed κ_A), the values of ε_r , ε_f and ψ are determined (Eqs. 4 and S32). However, the growth rate λ can be influenced by protein allocation between respiration and fermentation, specifically ϕ_r and ϕ_f , according to the governing equation (Eq. 3). If $\varepsilon_r > \varepsilon_f$, that is, if the proteome efficiency in respiration is higher than that in fermentation, then $\lambda = \frac{\phi_{\max} - J_f^{(E)}(1/\varepsilon_f - 1/\varepsilon_r)}{\psi + \phi/\varepsilon_r} \leq \frac{\phi_{\max}}{\psi + \phi/\varepsilon_r}$. The optimal growth strategy is $\phi_f = J_f^{(E)} = 0$, meaning that the cell exclusively uses respiration. Conversely, if $\varepsilon_f > \varepsilon_r$, then $\phi_r = J_r^{(E)} = 0$ is optimal, and the cell solely uses fermentation. In either case, the choice between respiration and fermentation for growth optimization is determined by comparing their proteome efficiencies.

In practice, both proteome efficiencies ε_r and ε_f are functions of nutrient quality κ_A , which can be significantly influenced by the nutrient type and concentration of the carbon source (see Eqs. 4 and S27). Therefore, the optimal growth strategy may vary depending on the nutrient conditions. In nutrient-poor conditions where $\kappa_A \ll \kappa_r^{(A)}$ and $\kappa_A \ll \kappa_f^{(A)}$, the proteome efficiencies can be approximated by $\varepsilon_r \approx \beta_r^{(A)} \cdot \kappa_A$ and $\varepsilon_f \approx \beta_f^{(A)} \cdot \kappa_A$ (see Eq. 4), and hence $\varepsilon_r(\kappa_A) > \varepsilon_f(\kappa_A)$

(since $\beta_r^{(A)} > \beta_f^{(A)}$), meaning that the proteome efficiency of respiration is higher than that of fermentation under these conditions. In contrast, in rich media, using parameters for κ_i derived from in vivo/in vitro experimental data for *E. coli* (see Appendix-tables 1-2 and Appendix 6.1-6.2), we obtain $\varepsilon_r(\kappa_{\text{glucose}}^{(\text{ST})}) < \varepsilon_f(\kappa_{\text{glucose}}^{(\text{ST})})$ with Eq. 4 (see also Eqs. S39-S40), where $\kappa_{\text{glucose}}^{(\text{ST})}$ represents the substrate quality of glucose at saturated concentration (abbreviated as “ST” in the superscript). This indicates that the proteome efficiency in fermentation is higher than that in respiration for bacteria in rich media. Indeed, recent studies have validated that the measured proteome efficiency in fermentation is higher than in respiration for *E. coli* in lactose at saturated concentration (Basan et al., 2015), i.e., $\varepsilon_r(\kappa_{\text{lactose}}^{(\text{ST})}) < \varepsilon_f(\kappa_{\text{lactose}}^{(\text{ST})})$. In Fig. 1E, we present the growth rate dependence of proteome efficiencies ε_r and ε_f in a three-dimensional (3D) format using the collected data shown in Appendix-table 1, where ε_r , ε_f and the growth rate λ all vary as functions of nutrient quality κ_A . Furthermore, the ratio Δ (defined as $\Delta(\kappa_A) \equiv \varepsilon_f(\kappa_A)/\varepsilon_r(\kappa_A)$) is a monotonically increasing function of κ_A , and there exists a critical value of κ_A (denoted as $\kappa_A^{(\text{C})}$; see Appendix 2.2 for details) satisfying $\Delta(\kappa_A^{(\text{C})}) = 1$. Below $\kappa_A^{(\text{C})}$, where the nutrient is poorer and the cell grows slowly, the proteome efficiency of fermentation is lower than that of respiration (i.e., $\varepsilon_f < \varepsilon_r$), hence respiration is the optimal choice (with $\lambda = \phi_{\text{max}} \cdot (\psi + \varphi/\varepsilon_r)^{-1}$). Above $\kappa_A^{(\text{C})}$, where the nutrient is richer and the cell grows faster, fermentation is more efficient than respiration in terms of proteome efficiency (i.e., $\varepsilon_f > \varepsilon_r$) and becomes the optimal growth strategy (with $\lambda = \phi_{\text{max}} \cdot (\psi + \varphi/\varepsilon_f)^{-1}$). This analysis qualitatively explains the phenomenon of aerobic glycolysis.

For a quantitative understanding of overflow metabolism, let us first consider the homogeneous case, where all cells share identical biochemical parameters. For optimal protein allocation, the relation between fermentation flux and growth rate under nutrient variation (with significantly varying κ_A) is given by $J_f^{(\text{E})} = \varphi \cdot \lambda \cdot \theta(\lambda - \lambda_c)$, where “ θ ” represents the Heaviside step function, and λ_c denotes the critical growth rate corresponding to the nutrient condition with nutrient quality $\kappa_A^{(\text{C})}$ (i.e., $\lambda_c \equiv \lambda(\kappa_A^{(\text{C})})$). Similarly, the growth rate dependence of respiration flux is $J_r^{(\text{E})} = \varphi \cdot \lambda \cdot [1 - \theta(\lambda - \lambda_c)]$. These digital response outcomes are consistent with the numerical simulation findings of Molenaar *et al.* (Molenaar et al., 2009). However, they are clearly incompatible with the threshold-analog response observed in the standard picture of overflow metabolism (Basan et al., 2015; Holms, 1996; Meyer et al., 1984; Nanchen et al., 2006; van Hoek et al., 1998).

To address this issue, we take into account cell heterogeneity, which is ubiquitous in both microbes (Ackermann, 2015; Bagamery et al., 2020; Balaban et al., 2004; Nikolic et al., 2013;

Solopova et al., 2014; Wallden et al., 2016; Yaginuma et al., 2014; Zhang et al., 2018) and tumor cells (Duraj et al., 2021; Hanahan and Weinberg, 2011; Hensley et al., 2016; Shibao et al., 2018). In the context of the Warburg effect or overflow metabolism, experimental studies have reported significant metabolic heterogeneity in the choice between respiration and fermentation within a cell population (Bagamery et al., 2020; Duraj et al., 2021; Hensley et al., 2016; Nikolic et al., 2013). Motivated by the observation that the turnover number (k_{cat} value) of a catalytic enzyme varies considerably between in vitro and in vivo measurements (Davidi et al., 2016; García-Contreras et al., 2012), we note that the concentrations of potassium and phosphate, which vary from cell to cell, have a significant impact on the k_{cat} values of metabolic enzymes (García-Contreras et al., 2012). Therefore, within a cell population, there is a distribution of k_{cat} values for a catalytic enzyme, commonly referred to as extrinsic noise (Elowitz et al., 2002). For simplicity, we assume that the k_{cat} values for each enzyme follow a Gaussian distribution. Consequently, the proteome efficiencies ε_r and ε_f , which are crucial for determining the choice between respiration and fermentation, also follow Gaussian distributions (see Appendix 7 for details). This variability leads to diverse distributions of single-cell growth rates across different carbon sources (see Eqs. S155-S157, S163-S165), which has been fully verified by recent experiments using isogenic *E. coli* at single-cell resolution (Wallden et al., 2016) (Appendix-fig. 2B). Accordingly, the critical growth rate λ_c is expected to follow a Gaussian distribution $\mathcal{N}(\mu_{\lambda_c}, \sigma_{\lambda_c}^2)$ within a cell population (see Appendix 7 for details), where μ_{λ_c} is approximated by the deterministic result of λ_c (Eq. S43). Assuming the coefficient of variation (CV) of λ_c is $\sigma_{\lambda_c} / \mu_{\lambda_c} = 12\%$, or equivalently that the CV for the catalytic rate of each metabolic enzyme is 25%, we derive the growth rate dependence of fermentation and respiration fluxes (see Appendix 2.3 for details):

$$\begin{cases} J_f^{(N)}(\lambda) = \frac{\varphi \cdot \lambda}{\beta_f^{(A)}} \cdot \left[\text{erf} \left(\frac{\lambda - \mu_{\lambda_c}}{\sqrt{2}\sigma_{\lambda_c}} \right) + 1 \right], \\ J_r^{(N)}(\lambda) = \frac{\varphi \cdot \lambda}{\beta_r^{(A)}} \cdot \left[1 - \text{erf} \left(\frac{\lambda - \mu_{\lambda_c}}{\sqrt{2}\sigma_{\lambda_c}} \right) \right], \end{cases} \quad (5)$$

where “erf” represents the error function. The fermentation flux exhibits a threshold-analog relation with the growth rate (the red curves in Figs. 1C-D, 2B-C, and 3B, D, F), while the respiration flux (the blue curve in Fig. 1D) decreases as the fermentation flux increases. In Fig. 1C-D, we observe that the model results (see Eq. 5 and Appendix 8; parameters are set based on the experimental data shown in Appendix-table 1) quantitatively agree with the experimental data from *E. coli* (Basan et al., 2015; Holms, 1996). The fermentation flux is represented by the acetate secretion rate $J_{\text{acetate}}^{(M)} = 2J_f^{(N)}$, and the respiration flux is exemplified by the carbon dioxide flux $J_{\text{CO}_2, r}^{(M)} = 6J_r^{(N)}$ (the superscript “(M)” represents the measurable flux in the unit of mM/OD600/h;

see Appendix 8.1 for details). By incorporating cell heterogeneity, our model of optimal protein allocation quantitatively explains overflow metabolism.

Testing the model through perturbations

To further test our model, we systematically investigate its predictions under various types of perturbations and compare them with experimental data from existing studies (Basan et al., 2015; Holms, 1996) (see Appendices 3 and 4.1 for details).

First, we consider the proteomic perturbation caused by overexpression of useless proteins encoded by the *lacZ* gene (i.e., ϕ_Z perturbation) in *E. coli*. The net effect of the ϕ_Z perturbation is that the maximum fraction of the proteome available for resource allocation changes from ϕ_{\max} to $\phi_{\max} - \phi_Z$ (Basan et al., 2015), where ϕ_Z is the proteomic mass fraction of useless proteins. In a cell population, the critical growth rate $\lambda_c(\phi_Z)$ still follows a Gaussian distribution $\mathcal{N}(\mu_{\lambda_c}(\phi_Z), \sigma_{\lambda_c}(\phi_Z)^2)$, where the CV of $\lambda_c(\phi_Z)$ remains unchanged. Consequently, the growth

rate dependence of fermentation flux changes to $J_f^{(N)} = \frac{\varphi \cdot \lambda}{\beta_f^{(A)}} \cdot \left[\operatorname{erf} \left(\frac{\lambda - \mu_{\lambda_c}(\phi_Z)}{\sqrt{2}\sigma_{\lambda_c}(\phi_Z)} \right) + 1 \right]$ (see

Appendix 3 for model perturbation results regarding respiration flux), where both the growth rate $\lambda(\kappa_A, \phi_Z)$ and the normalized fermentation flux $J_f^{(N)}(\kappa_A, \phi_Z)$ are bivariate functions of κ_A and ϕ_Z (see Eqs. S49 and S56-S57). For each degree of LacZ expression (with fixed ϕ_Z), similar to wild-type strains, the fermentation flux exhibits a threshold-analog response to growth rate as κ_A varies (see Fig. 2C), which agrees quantitatively with experimental results (Basan et al., 2015). The shifts in the critical growth rate $\lambda_c(\phi_Z)$ are fully captured by $\mu_{\lambda_c}(\phi_Z) = \mu_{\lambda_c}(0)(1 - \phi_Z/\phi_{\max})$. In contrast, for nutrient conditions with each fixed κ_A , since the growth rate changes with ϕ_Z just like $\lambda_c(\phi_Z)$: $\lambda(\kappa_A, \phi_Z) = \lambda(\kappa_A, 0)(1 - \phi_Z/\phi_{\max})$, the fermentation flux is then proportional to the

growth rate for the varying levels of LacZ expression: $J_f^{(N)} = \frac{\varphi}{\beta_f^{(A)}} \cdot \left[\operatorname{erf} \left(\frac{\lambda(\kappa_A, 0) - \mu_{\lambda_c}(0)}{\sqrt{2}\sigma_{\lambda_c}(0)} \right) + 1 \right] \cdot \lambda$,

where the slope is a monotonically increasing function of the substrate quality κ_A . These scaling relations are well validated by the experimental data (Basan et al., 2015) shown in Fig. 2B. Finally, in the case where both κ_A and ϕ_Z are free to vary, the growth rate dependence of fermentation flux presents a threshold-analog response surface in a 3D plot, where ϕ_Z appears explicitly as the y -axis (see Fig. 2A). Experimental data points (Basan et al., 2015) lie right on this surface, which is highly consistent with the model predictions.

Next, we study the influence of energy dissipation, which introduces an energy dissipation coefficient w to Eq. 2: $J_E^{(N)} = \eta_E \cdot \lambda + w$. Similarly, the critical growth rate in this case, $\lambda_c(w)$, follows a Gaussian distribution $\mathcal{N}(\mu_{\lambda_c}(w), \sigma_{\lambda_c}(w)^2)$ in a cell population. The relation between the growth rate and fermentation flux can be characterized by (see Appendix 3.2 for details):

$$J_f^{(N)} = \frac{\varphi \cdot \lambda + w}{\beta_f^{(A)}} \cdot \left[\operatorname{erf} \left(\frac{\lambda - \mu_{\lambda_c}(w)}{\sqrt{2} \sigma_{\lambda_c}(w)} \right) + 1 \right].$$

In Fig. 3A-B, we present a comparison between the model results and experimental data (Basan et al., 2015) in 3D and 2D plots, which demonstrate good agreement. A notable characteristic of energy dissipation, as distinguished from ϕ_Z perturbation, is that the fermentation flux increases despite a decrease in the growth rate when κ_A is fixed.

We proceed to analyze the impact of translation inhibition with different sub-lethal doses of chloramphenicol on *E. coli*. This type of perturbation introduces an inhibition coefficient ι to the translation rate, thus turning κ_t into $\kappa_t / (\iota + 1)$. Still, the critical growth rate $\lambda_c(\iota)$ follows a Gaussian distribution $\mathcal{N}(\mu_{\lambda_c}(\iota), \sigma_{\lambda_c}(\iota)^2)$, and then, the growth rate dependence of fermentation

$$\text{flux is given by: } J_f^{(N)} = \frac{\varphi \cdot \lambda}{\beta_f^{(A)}} \cdot \left[\operatorname{erf} \left(\frac{\lambda - \mu_{\lambda_c}(\iota)}{\sqrt{2} \sigma_{\lambda_c}(\iota)} \right) + 1 \right] \text{ (see Appendix 3.3 for details).}$$

In Appendix-fig. 2D-E, we observe that the model predictions are generally consistent with the experimental data (Basan et al., 2015). However, a noticeable systematic discrepancy arises when the translation rate is low. Therefore, we consider maintenance energy, which is typically tiny and generally negligible for bacteria over the growth rate range of interest (Basan et al., 2015; Locasale and Cantley, 2010; Neidhardt, 1996). Encouragingly, by assigning a very small value to the maintenance energy coefficient w_0 (where $w_0 = 2.5 \text{ (h}^{-1}\text{)}$), the model results for the growth rate-

$$\text{fermentation flux relation } J_f^{(N)} = \frac{\varphi \cdot \lambda + w_0}{\beta_f^{(A)}} \cdot \left[\operatorname{erf} \left(\frac{\lambda - \mu_{\lambda_c}(\iota)}{\sqrt{2} \sigma_{\lambda_c}(\iota)} \right) + 1 \right] \text{ quantitatively agree with}$$

experiments (Basan et al., 2015) (see Fig. 3C-D and Appendix 3.3 for details).

Finally, we consider the alteration of nutrient categories by switching to a non-Group A carbon source: pyruvate, which enters the metabolic network from the endpoint of glycolysis (Neidhardt et al., 1990; Nelson et al., 2008). The coarse-grained model for pyruvate utilization is shown in Fig. 3E (see also Fig. 1A), which shares identical precursor pools with those for Group A carbon sources, yet has several differences in the coarse-grained reactions. The growth rate dependencies of both the proteome efficiencies (see Appendix-fig. 2H) and energy fluxes (see Fig. 3F) are qualitatively similar to those of Group A carbon source utilization, while there are quantitative differences in the coarse-grained parameters (see Appendices 4.1 and 8 for derivation details).

Most notably, the critical growth rate $\lambda_c^{(\text{py})}$ and the ATP production per glucose in the fermentation pathway $\beta_f^{(\text{py})}$ for pyruvate utilization are noticeably smaller than those for Group A sources (i.e., λ_c and $\beta_f^{(A)}$, respectively). Consequently, the growth rate dependence of fermentation flux in pyruvate should present a distinctly different curve from that of Group A carbon sources (see Eqs. 5 and S105), which is fully validated by experimental results (Holms, 1996) (see Fig. 3F).

Enzyme allocation under perturbations

As mentioned above, our coarse-grained model is topologically identical to the central metabolic network (Fig. 1A) and can thus predict enzyme allocation for each gene in glycolysis and the TCA cycle (see Appendix-fig. 1B and Appendix-table 1) under various types of perturbations. In Fig. 1B, the intermediate nodes M_1 , M_2 , M_3 , M_4 , and M_5 represent G6P, PEP, acetyl-CoA, α -ketoglutarate, and oxaloacetate, respectively. Therefore, ϕ_1 and ϕ_2 correspond to enzymes involved in glycolysis (or at the junction of glycolysis and the TCA cycle), while ϕ_3 and ϕ_4 correspond to enzymes in the TCA cycle (see Fig. 1A-B and Appendix 2.1).

We first consider enzyme allocation under carbon limitation by varying the nutrient type and concentration of a Group A carbon source (i.e., κ_A perturbation). This has been extensively studied in more simplified models (Hui et al., 2015; You et al., 2013), where the growth rate dependence of enzyme allocation under κ_A perturbation is generally described by a C-line response (Hui et al., 2015; You et al., 2013). Specifically, the genes responsible for digesting carbon compounds exhibit a linear increase in gene expression as the growth rate decreases (Hui et al., 2015; You et al., 2013). However, when it comes to enzymes catalyzing reactions between intermediate nodes, we gathered experimental data from existing studies (Hui et al., 2015) and found that the enzymes in glycolysis exhibit a completely different response pattern compared to those in the TCA cycle (Appendix-fig. 3A-B). This discrepancy cannot be explained by the C-line response. To address this issue, we apply the coarse-grained model described above (see Fig. 1B) to calculate the growth rate dependence of enzyme allocation for each ϕ_i ($i = 1, 2, 3, 4$) using model settings for wild-type strains, with no fitting parameters influencing the shape (see Eqs. S118-S119 and Appendix 8). In Fig. 4A-B and Appendix-fig. 3C-D, we see that the model predictions overall match with the experimental data (Hui et al., 2015) for representative genes from either glycolysis or the TCA cycle, and maintenance energy (with $w_0 = 2.5 \text{ (h}^{-1}\text{)})$ has a negligible effect on this process. Still, there are minor discrepancies that arise from the basal expression of metabolic genes, which may be attributed to the fact that our model deals with relatively stable growth conditions while microbes need to be prepared for fluctuating environments (Basan et al., 2020; Kussell and Leibler, 2005; Mori et al., 2017).

We proceed to analyze the influence of ϕ_z perturbation and energy dissipation. In both cases, our model predicts a linear response to growth rate reduction for all genes in either glycolysis or the TCA cycle (see Appendix 5.2-5.3 for details). For ϕ_z perturbation, all predicted slopes are

positive, and there are no fitting parameters involved (Eqs. S120-S121). In Fig. 4C-D and Appendix-fig. 3E-J, we show that our model quantitatively illustrates the experimental data (Basan et al., 2015) for representative genes in the central metabolic network, and there is better agreement with experiments (Basan et al., 2015) by incorporating the maintenance energy (with $w_0 = 2.5 \text{ (h}^{-1}\text{)}$ as aforementioned). For energy dissipation, however, the predicted slopes of the enzymes corresponding to ϕ_4 are negative, and there is a constraint that the slope signs of the enzymes corresponding to the same ϕ_i ($i = 1, 2, 3$) should be the same. In Appendix-fig. 3K-N, we see that the model results (Eqs. S127 and S123) are consistent with experiments (Basan et al., 2015).

Explanation of the Crabtree effect in yeast and the Warburg effect in cancer cells

We proceed to apply our model to explain the Crabtree effect in yeast (Bagamery et al., 2020; De Deken, 1966; Shen et al., 2024) and the Warburg effect in tumors (Bartman et al., 2023; Duraj et al., 2021; Hanahan and Weinberg, 2011; Liberti and Locasale, 2016; Shen et al., 2024; Vander Heiden et al., 2009) with slight modifications using the optimal growth principle combined with cell heterogeneity (see Appendix 9 and Appendix-fig. 5). For yeast and tumors, similar to the case of *E. coli*, the proteome efficiencies ε_r and ε_f are both increasing functions of nutrient quality κ_A (see Eq. S170). Under poor nutrient conditions (i.e., κ_A is small), the proteome efficiency in respiration is higher than that in fermentation: $\varepsilon_r > \varepsilon_f$ (see Eqs. S174-S175), making respiration the optimal choice for growth optimization (see Eq. S171). Conversely, when nutrients are abundant and $\varepsilon_f > \varepsilon_r$, aerobic glycolysis (i.e., fermentation) becomes the optimal growth strategy (see Eq. S172). Further combination with cell heterogeneity results in the standard picture of overflow metabolism, which has indeed been observed in yeast (van Hoek et al., 1998). However, it remains challenging to tune the growth rate of cancer cells in vivo.

Recently, Shen et al. (Shen et al., 2024) discovered that the proteome efficiency measured at the cell population level in respiration (i.e., $\langle \varepsilon_r \rangle$; where “ $\langle \rangle$ ” denotes the population average) is higher than that in fermentation (i.e., $\langle \varepsilon_f \rangle$) for many yeast and cancer cells, despite the presence of fermentation fluxes through aerobic glycolysis. Evidently, this finding (Shen et al., 2024) contradicts prevalent explanations (Basan et al., 2015; Chen and Nielsen, 2019), which hold that overflow metabolism arises because the proteome efficiency in fermentation is consistently higher than in respiration. Nevertheless, our model may resolve this puzzle due to the incorporation of two important features. First, our model predicts that the proteome efficiency in respiration is larger than that in fermentation when nutrient quality is low (see Eqs. S174-S175). Second, and crucially, by accounting for cell heterogeneity, our model allows a proportion of cells to have a higher proteome efficiency in fermentation than in respiration, even when the overall proteome efficiency in respiration at the cell population level is greater than that in fermentation (i.e., $\langle \varepsilon_r \rangle > \langle \varepsilon_f \rangle$).

To compare our model results quantitatively with experimental data on yeast and tumors (Shen et al., 2024), we define $\text{Pr}_f \equiv \frac{J_f^{(E)}}{J_f^{(E)} + J_r^{(E)}}$ as the fraction of ATP produced through fermentation.

To account for cell heterogeneity, we apply Gaussian distributions to enzyme turnover numbers, as described above. This yields the relationship between Pr_f (i.e., $\frac{J_f^{(E)}}{J_f^{(E)} + J_r^{(E)}}$) and $\langle \varepsilon_r \rangle$ and $\langle \varepsilon_f \rangle$ through derivations (see Eqs. S180-S190 and Appendix 9 for details):

$$\frac{J_f^{(E)}}{J_f^{(E)} + J_r^{(E)}} = \frac{1}{2} \left[\text{erf} \left(\frac{1 - \langle \varepsilon_r \rangle / \langle \varepsilon_f \rangle}{\sqrt{2} \cdot \sqrt{\chi_{\varepsilon_r}^2 + \chi_{\varepsilon_f}^2 \cdot (\langle \varepsilon_r \rangle / \langle \varepsilon_f \rangle)^2}} \right) + 1 \right], \quad (6)$$

where χ_{ε_r} and χ_{ε_f} represent the CVs of proteome efficiencies ε_r and ε_f , respectively. Due to the higher levels of cell heterogeneity in yeast (Bagamery et al., 2020) and cancer cells (Duraj et al., 2021; Hanahan and Weinberg, 2011; Hensley et al., 2016), the CVs of ε_r and ε_f (i.e., χ_{ε_r} and χ_{ε_f}) in these cells are expected to be significantly higher than those in *E. coli*, although their precise values are unknown. The values for the variables shown in Eq. 6 can be obtained from experiments. Therefore, we plot the theoretical results from Eq. 6 using χ_{ε_r} and χ_{ε_f} values of 0.25, 0.40, and 0.58 to compare with experimental data from yeast and in vivo mouse tumors (Bartman et al., 2023; Shen et al., 2024). As shown in Fig. 5A-B, the theoretical results with $\chi_{\varepsilon_r} = \chi_{\varepsilon_f} = 0.58$ align quantitatively with the experimental data (Bartman et al., 2023; Shen et al., 2024) on both logarithmic and linear scales, demonstrating that our model has the potential to quantitatively explain the Crabtree effect in yeast and the Warburg effect in cancer cells.

Discussion

The phenomenon of overflow metabolism, or the Warburg effect, has been a long-standing puzzle in cell metabolism. Although many rationales have been proposed over the past century (Basan et al., 2015; Chen and Nielsen, 2019; Majewski and Domach, 1990; Molenaar et al., 2009; Niebel et al., 2019; Peebo et al., 2015; Pfeiffer et al., 2001; Shlomi et al., 2011; Vander Heiden et al., 2009; Varma and Palsson, 1994; Vazquez et al., 2010; Vazquez and Oltvai, 2016; Zhuang et al., 2011), contradictions persist (Shen et al., 2024), leaving the origin and function of this phenomenon unclear (DeBerardinis and Chandel, 2020; Hanahan and Weinberg, 2011; Liberti and Locasale, 2016; Vander Heiden et al., 2009). In this study, we use *E. coli* as a typical example and demonstrate that overflow metabolism can be understood through optimal protein allocation combined with cell heterogeneity. Under nutrient-poor conditions, the proteome efficiency of respiration is higher than that of fermentation (see Fig. 1E), and thus the cell uses respiration to optimize growth. In rich media, however, the proteome efficiency of fermentation increases more

rapidly and surpasses that of respiration (see Fig. 1E), leading the cell to adopt fermentation as the optimal growth strategy. In further combination with cell heterogeneity in enzyme catalytic rates (Davidi et al., 2016; García-Contreras et al., 2012), our model quantitatively illustrates the threshold-analog response (Basan et al., 2015; Holms, 1996) in overflow metabolism (see Fig. 1C). Furthermore, it quantitatively explains the data on the Crabtree effect in yeast and the Warburg effect in cancer cells (Bartman et al., 2023; Shen et al., 2024).

Mechanistically, the optimal growth strategy for the binary choice between respiration and fermentation can be facilitated by the direct sensing and comparison of proteome efficiencies between the two pathways (see Appendix 2.4). A growing body of evidence suggests that the cyclic AMP (cAMP)-cAMP receptor protein (CRP) system plays a crucial role in sensing proteome efficiency and executing the optimal strategy (Basan et al., 2015; Towbin et al., 2017; Valgepea et al., 2010; Wehrens et al., 2023). However, it has also been suggested that the cAMP-CRP system alone is insufficient, and that additional regulators remain to be identified to fully elucidate this mechanism (Basan et al., 2015; Valgepea et al., 2010). Furthermore, since the binary choice between respiration and fermentation is driven by the comparison of proteome efficiencies, the optimal growth principle in our model can be relaxed to the case where efficient protein allocation is required only for enzymes, rather than ribosomes. This allows our model to remain applicable under suboptimal growth conditions (see Appendix 2.4 for details), where recent experimental studies have shown that the inactive portion of ribosomes (i.e., ribosomes not bound to mRNAs) may vary with culturing conditions (Dai et al., 2017; Li et al., 2018) and between individual cells within the same culture (Pavlou et al., 2025), despite an overall trend toward growth optimization.

In existing rationales (Basan et al., 2015; Chen and Nielsen, 2019; Majewski and Domach, 1990; Shlomi et al., 2011; Varma and Palsson, 1994; Vazquez and Oltvai, 2016), the standard picture of overflow metabolism (Basan et al., 2015; Holms, 1996; Meyer et al., 1984; Nanchen et al., 2006; van Hoek et al., 1998) has primarily been illustrated by a threshold-linear response, which largely relies on the assumption that cells optimize their growth rate for a given rate of carbon influx under each nutrient condition (or similar equivalents, see Appendix 6.3). However, in practice, for microbes or tumor cells grown *in vitro* or *in vivo*, the given factors are the identity and concentration of the nutrient (Molenaar et al., 2009; Scott et al., 2010; Wang et al., 2019), rather than the rate of carbon influx. Additionally, prevalent explanations (Basan et al., 2015; Chen and Nielsen, 2019) suggest that overflow metabolism originates from the proteome efficiency in fermentation always being higher than that in respiration (see Appendix 6.3 for details). While it has been observed in *E. coli* that proteome efficiency in fermentation is higher than that in respiration for cells cultured in lactose at saturated concentration (Basan et al., 2015), Shen et al. (Shen et al., 2024) reported that for many yeast and cancer cells, the proteome efficiency in fermentation is noticeably lower than that in respiration, despite the presence of aerobic glycolytic fermentation flux. This observation (Shen et al., 2024) evidently contradicts the prevalent explanations (Basan et al., 2015; Chen and Nielsen, 2019). Our model resolves this puzzle by significantly differing from existing rationales in its optimization principle, where we optimize

cell growth rate purely through protein allocation without imposing a special constraint on carbon influx (see Appendix 6.3 for details). More importantly, our model incorporates cell heterogeneity, which is crucial for both explaining the threshold-analog response in overflow metabolism and for resolving this puzzle raised by Shen et al. (Shen et al., 2024).

In the homogeneous case, the optimal growth strategy for growth rate dependent fermentation flux results in a digital response (see Eq. S44), corresponding to an elementary flux mode (Müller et al., 2014; Wortel et al., 2014), which aligns with the numerical study by Molenaar *et al.* (Molenaar et al., 2009) but is incompatible with the standard picture of overflow metabolism (Basan et al., 2015; Holms, 1996; Meyer et al., 1984; Nanchen et al., 2006; van Hoek et al., 1998). Furthermore, in this case, cells would not generate fermentation flux if the proteome efficiency in fermentation were lower than that in respiration, under the optimal growth framework. By incorporating heterogeneity in enzyme catalytic rates (Davidi et al., 2016; García-Contreras et al., 2012), the critical growth rate (i.e., threshold) shifts from a single value to a Gaussian distribution (see Eq. S45 and Appendix 7 for details; see also Appendix-fig. 4) across a cell population, thereby turning a digital response into the threshold-analog response observed in overflow metabolism (see Fig. 1C). Moreover, cell heterogeneity allows a fraction of cells to possess a larger proteome efficiency in fermentation than in respiration despite the overall proteome efficiency in respiration at the cell population level is higher than in fermentation. This mechanism facilitates the fermentation flux in yeast and cancer cells observed by Shen et al. (Shen et al., 2024) (see Fig. 5A-B).

Our model results, based on cell heterogeneity, are further supported by observed distributions of single-cell growth rates in *E. coli* (Wallden et al., 2016) (see Appendix-fig. 2B), as well as by experiments involving various types of perturbations (Basan et al., 2015; Holms, 1996; Hui et al., 2015), both in terms of acetate secretion patterns and gene expression in the central metabolic network (see Fig. 2-4, Appendix-figs. 2D-E and 3). Furthermore, the heterogeneity patterns predicted by our model for fermentation and respiration modes in an isogenic cell population under the same culturing conditions are highly consistent with the non-genetic heterogeneity observed in single-cell experiments with *E. coli* (Nikolic et al., 2013) and *S. cerevisiae* (Bagamery et al., 2020), and align with experiments on intra-tumor heterogeneity in glioblastoma (Duraj et al., 2021; Shibao et al., 2018). Finally, our model can be broadly applied to address heterogeneity-related challenges in metabolism on a quantitative basis, including diverse metabolic strategies of cells in various environments (Bagamery et al., 2020; Duraj et al., 2021; Escalante-Chong et al., 2015; Hensley et al., 2016; Liu et al., 2015; Solopova et al., 2014; Wang et al., 2019).

Author contributions

X.W. conceived and designed the project, developed the model, carried out the analytical and numerical calculations, and wrote the paper.

Competing Interest Statement:

The author declares no competing interests.

Data, Materials, and Software Availability.

All study data are included in the article and/or appendices.

Acknowledgements

The author thanks Chao Tang, Qi Ouyang, Yang-Yu Liu and Kang Xia for helpful discussions. This work was supported by National Natural Science Foundation of China (Grant Nos.12004443 and 12474207), Guangzhou Municipal Innovation Fund (Grant No.202102020284) and the Hundred Talents Program of Sun Yat-sen University.

References

- Ackermann, M. (2015). A functional perspective on phenotypic heterogeneity in microorganisms. *Nature Reviews Microbiology* *13*, 497-508.
- Bagamery, L.E., Justman, Q.A., Garner, E.C., and Murray, A.W. (2020). A putative bet-hedging strategy buffers budding yeast against environmental instability. *Current Biology* *30*, 4563-4578.
- Balaban, N.Q., Merrin, J., Chait, R., Kowalik, L., and Leibler, S. (2004). Bacterial persistence as a phenotypic switch. *Science* *305*, 1622-1625.
- Bartman, C.R., Weilandt, D.R., Shen, Y., Lee, W.D., Han, Y., TeSlaa, T., Jankowski, C.S.R., Samarah, L., Park, N.R., da Silva-Diz, V., et al. (2023). Slow TCA flux and ATP production in primary solid tumours but not metastases. *Nature* *614*, 349-357.
- Basan, M., Honda, T., Christodoulou, D., Hörl, M., Chang, Y.-F., Leoncini, E., Mukherjee, A., Okano, H., Taylor, B.R., Silverman, J.M., et al. (2020). A universal trade-off between growth and lag in fluctuating environments. *Nature* *584*, 470-474.
- Basan, M., Hui, S., Okano, H., Zhang, Z., Shen, Y., Williamson, J.R., and Hwa, T. (2015). Overflow metabolism in *Escherichia coli* results from efficient proteome allocation. *Nature* *528*, 99-104.
- Bennett, B.D., Kimball, E.H., Gao, M., Osterhout, R., Van Dien, S.J., and Rabinowitz, J.D. (2009). Absolute metabolite concentrations and implied enzyme active site occupancy in *Escherichia coli*. *Nature Chemical Biology* *5*, 593-599.
- Chen, Y., and Nielsen, J. (2019). Energy metabolism controls phenotypes by protein efficiency and allocation. *Proceedings of the National Academy of Sciences* *116*, 17592-17597.
- Dai, X., Zhu, M., Warren, M., Balakrishnan, R., Patsalo, V., Okano, H., Williamson, J.R., Fredrick, K., Wang, Y.-P., and Hwa, T. (2017). Reduction of translating ribosomes enables *Escherichia coli* to maintain elongation rates during slow growth. *Nature Microbiology* *2*, 16231.
- Davidi, D., Noor, E., Liebermeister, W., Bar-Even, A., Flamholz, A., Tummler, K., Barenholz, U., Goldenfeld, M., Shlomi, T., and Milo, R. (2016). Global characterization of in vivo enzyme catalytic rates and their correspondence to in vitro kcat measurements. *Proceedings of the National Academy of Sciences* *113*, 3401-3406.

De Deken, R. (1966). The Crabtree effect: a regulatory system in yeast. *Microbiology* *44*, 149-156.

DeBerardinis, R.J., and Chandel, N. (2020). We need to talk about the Warburg effect. *Nature Metabolism* *2*, 127-129.

Dekel, E., and Alon, U. (2005). Optimality and evolutionary tuning of the expression level of a protein. *Nature* *436*, 588-592.

Duraj, T., García-Romero, N., Carrión-Navarro, J., Madurga, R., Ortiz de Mendivil, A., Prat-Acin, R., Garcia-Cañamaque, L., and Ayuso-Sacido, A. (2021). Beyond the Warburg effect: Oxidative and glycolytic phenotypes coexist within the metabolic heterogeneity of glioblastoma. *Cells* *10*, 202.

Ebenhöh, O., Ebeling, J., Meyer, R., Pohlkotte, F., and Nies, T. (2024). Microbial Pathway Thermodynamics: Stoichiometric Models Unveil Anabolic and Catabolic Processes. *Life* *14*, 247.

Edwards, J.S., Ibarra, R.U., and Palsson, B.O. (2001). In silico predictions of Escherichia coli metabolic capabilities are consistent with experimental data. *Nature Biotechnology* *19*, 125-130.

Elowitz, M.B., Levine, A.J., Siggia, E.D., and Swain, P.S. (2002). Stochastic gene expression in a single cell. *Science* *297*, 1183-1186.

Escalante-Chong, R., Savir, Y., Carroll, S.M., Ingraham, J.B., Wang, J., Marx, C.J., and Springer, M. (2015). Galactose metabolic genes in yeast respond to a ratio of galactose and glucose. *Proceedings of the National Academy of Sciences* *112*, 1636-1641.

García-Contreras, R., Vos, P., Westerhoff, H.V., and Boogerd, F.C. (2012). Why in vivo may not equal in vitro—new effectors revealed by measurement of enzymatic activities under the same in vivo-like assay conditions. *The FEBS Journal* *279*, 4145-4159.

Hanahan, D., and Weinberg, R.A. (2011). Hallmarks of cancer: the next generation. *Cell* *144*, 646-674.

Hensley, C.T., Faubert, B., Yuan, Q., Lev-Cohain, N., Jin, E., Kim, J., Jiang, L., Ko, B., Skelton, R., Loudat, L., et al. (2016). Metabolic heterogeneity in human lung tumors. *Cell* *164*, 681-694.

Holms, H. (1996). Flux analysis and control of the central metabolic pathways in Escherichia coli. *FEMS Microbiology Reviews* *19*, 85-116.

Hui, S., Silverman, J.M., Chen, S.S., Erickson, D.W., Basan, M., Wang, J., Hwa, T., and Williamson, J.R. (2015). Quantitative proteomic analysis reveals a simple strategy of global resource allocation in bacteria. *Molecular Systems Biology* *11*, 784.

Kostinski, S., and Reuveni, S. (2020). Ribosome composition maximizes cellular growth rates in E. coli. *Physical Review Letters* *125*, 028103.

Kussell, E., and Leibler, S. (2005). Phenotypic diversity, population growth, and information in fluctuating environments. *Science* *309*, 2075-2078.

Li, S.H.-J., Li, Z., Park, J.O., King, C.G., Rabinowitz, J.D., Wingreen, N.S., and Gitai, Z. (2018). Escherichia coli translation strategies differ across carbon, nitrogen and phosphorus limitation conditions. *Nature Microbiology* *3*, 939-947.

Liberti, M.V., and Locasale, J.W. (2016). The Warburg effect: how does it benefit cancer cells? *Trends in Biochemical Sciences* *41*, 211-218.

Liu, X., Wang, X., Yang, X., Liu, S., Jiang, L., Qu, Y., Hu, L., Ouyang, Q., and Tang, C. (2015). Reliable cell cycle commitment in budding yeast is ensured by signal integration. *eLife* 4, e03977.

Locasale, J.W., and Cantley, L.C. (2010). Altered metabolism in cancer. *BMC Biology* 8, 88.

Majewski, R., and Domach, M. (1990). Simple constrained-optimization view of acetate overflow in *E. coli*. *Biotechnology and Bioengineering* 35, 732-738.

Meyer, H.-P., Leist, C., and Fiechter, A. (1984). Acetate formation in continuous culture of *Escherichia coli* K12 D1 on defined and complex media. *Journal of Biotechnology* 1, 355-358.

Molenaar, D., Van Berlo, R., De Ridder, D., and Teusink, B. (2009). Shifts in growth strategies reflect tradeoffs in cellular economics. *Molecular Systems Biology* 5, 323.

Mori, M., Schink, S., Erickson, D.W., Gerland, U., and Hwa, T. (2017). Quantifying the benefit of a proteome reserve in fluctuating environments. *Nature Communications* 8, 1225.

Müller, S., Regensburger, G., and Steuer, R. (2014). Enzyme allocation problems in kinetic metabolic networks: Optimal solutions are elementary flux modes. *Journal of Theoretical Biology* 347, 182-190.

Nanchen, A., Schicker, A., and Sauer, U. (2006). Nonlinear dependency of intracellular fluxes on growth rate in miniaturized continuous cultures of *Escherichia coli*. *Applied and Environmental Microbiology* 72, 1164-1172.

Neidhardt, F.C. (1996). *Escherichia coli* and *Salmonella*: cellular and molecular biology. (Washington, DC: ASM Press).

Neidhardt, F.C., Ingraham, J.L., and Schaechter, M. (1990). *Physiology of the bacterial cell*. (Sinauer associates).

Nelson, D.L., Lehninger, A.L., and Cox, M.M. (2008). *Lehninger principles of biochemistry*. (Macmillan).

Niebel, B., Leupold, S., and Heinemann, M. (2019). An upper limit on Gibbs energy dissipation governs cellular metabolism. *Nature Metabolism* 1, 125-132.

Nikolic, N., Barner, T., and Ackermann, M. (2013). Analysis of fluorescent reporters indicates heterogeneity in glucose uptake and utilization in clonal bacterial populations. *BMC Microbiology* 13, 258.

Park, J.O., Rubin, S.A., Xu, Y.-F., Amador-Noguez, D., Fan, J., Shlomi, T., and Rabinowitz, J.D. (2016). Metabolite concentrations, fluxes and free energies imply efficient enzyme usage. *Nature Chemical Biology* 12, 482-489.

Pavlou, A., Cinquemani, E., Pinel, C., Giordano, N., Mathilde, V.M.-G., Mihalcescu, I., Geiselmann, J., and de Jong, H. (2025). Single-cell data reveal heterogeneity of investment in ribosomes across a bacterial population. *Nature Communications* 16, 285.

Peebo, K., Valgepea, K., Maser, A., Nahku, R., Adamberg, K., and Vilu, R. (2015). Proteome reallocation in *Escherichia coli* with increasing specific growth rate. *Molecular BioSystems* 11, 1184-1193.

Pfeiffer, T., Schuster, S., and Bonhoeffer, S. (2001). Cooperation and competition in the evolution of ATP-producing pathways. *Science* 292, 504-507.

Scott, M., Gunderson, C.W., Mateescu, E.M., Zhang, Z., and Hwa, T. (2010). Interdependence of cell growth and gene expression: origins and consequences. *Science* *330*, 1099-1102.

Shen, Y., Dinh, H.V., Cruz, E.R., Chen, Z., Bartman, C.R., Xiao, T., Call, C.M., Ryseck, R.-P., Pratas, J., Weilandt, D., et al. (2024). Mitochondrial ATP generation is more proteome efficient than glycolysis. *Nature Chemical Biology* *20*, 1123-1132.

Shibao, S., Minami, N., Koike, N., Fukui, N., Yoshida, K., Saya, H., and Sampetean, O. (2018). Metabolic heterogeneity and plasticity of glioma stem cells in a mouse glioblastoma model. *Neuro-Oncology* *20*, 343-354.

Shlomi, T., Benyamini, T., Gottlieb, E., Sharan, R., and Ruppin, E. (2011). Genome-scale metabolic modeling elucidates the role of proliferative adaptation in causing the Warburg effect. *PLoS Computational Biology* *7*, e1002018.

Solopova, A., Van Gestel, J., Weissing, F.J., Bachmann, H., Teusink, B., Kok, J., and Kuipers, O.P. (2014). Bet-hedging during bacterial diauxic shift. *Proceedings of the National Academy of Sciences* *111*, 7427-7432.

Towbin, B.D., Korem, Y., Bren, A., Doron, S., Sorek, R., and Alon, U. (2017). Optimality and sub-optimality in a bacterial growth law. *Nature Communications* *8*, 14123.

Valgepea, K., Adamberg, K., Nahku, R., Lahtvee, P.-J., Arike, L., and Vilu, R. (2010). Systems biology approach reveals that overflow metabolism of acetate in *Escherichia coli* is triggered by carbon catabolite repression of acetyl-CoA synthetase. *BMC Systems Biology* *4*, 166.

van Hoek, P., Flikweert, M.T., van der Aart, Q.J., Steensma, H.Y., van Dijken, J.P., and Pronk, J.T. (1998). Effects of pyruvate decarboxylase overproduction on flux distribution at the pyruvate branch point in *Saccharomyces cerevisiae*. *Applied and Environmental Microbiology* *64*, 2133-2140.

Vander Heiden, M.G., Cantley, L.C., and Thompson, C.B. (2009). Understanding the Warburg effect: the metabolic requirements of cell proliferation. *Science* *324*, 1029-1033.

Varma, A., and Palsson, B.O. (1994). Stoichiometric flux balance models quantitatively predict growth and metabolic by-product secretion in wild-type *Escherichia coli* W3110. *Applied and Environmental Microbiology* *60*, 3724-3731.

Vazquez, A., Liu, J., Zhou, Y., and Oltvai, Z.N. (2010). Catabolic efficiency of aerobic glycolysis: the Warburg effect revisited. *BMC Systems Biology* *4*, 58.

Vazquez, A., and Oltvai, Z.N. (2016). Macromolecular crowding explains overflow metabolism in cells. *Scientific Reports* *6*, 31007.

Wallden, M., Fange, D., Lundius, E.G., Baltekin, Ö., and Elf, J. (2016). The synchronization of replication and division cycles in individual *E. coli* cells. *Cell* *166*, 729-739.

Wang, X., Xia, K., Yang, X., and Tang, C. (2019). Growth strategy of microbes on mixed carbon sources. *Nature Communications* *10*, 1279.

Warburg, O., Posener, K., and Negelein, E. (1924). Über den Stoffwechsel der Carcinomzelle. *Biochemische Zeitschrift* *152*, 309-344.

- Wehrens, M., Krahl, L.H., Towbin, B.D., Hermsen, R., and Tans, S.J. (2023). The interplay between metabolic stochasticity and cAMP-CRP regulation in single *E. coli* cells. *Cell Reports* 42, 113284.
- Wortel, M.T., Peters, H., Hulshof, J., Teusink, B., and Bruggeman, F.J. (2014). Metabolic states with maximal specific rate carry flux through an elementary flux mode. *The FEBS Journal* 281, 1547-1555.
- Yaginuma, H., Kawai, S., Tabata, K.V., Tomiyama, K., Kakizuka, A., Komatsuzaki, T., Noji, H., and Imamura, H. (2014). Diversity in ATP concentrations in a single bacterial cell population revealed by quantitative single-cell imaging. *Scientific Reports* 4, 6522.
- You, C., Okano, H., Hui, S., Zhang, Z., Kim, M., Gunderson, C.W., Wang, Y.-P., Lenz, P., Yan, D., and Hwa, T. (2013). Coordination of bacterial proteome with metabolism by cyclic AMP signalling. *Nature* 500, 301-306.
- Zhang, Z., Miliadis-Argenteis, A., and Heinemann, M. (2018). Dynamic single-cell NAD (P) H measurement reveals oscillatory metabolism throughout the *E. coli* cell division cycle. *Scientific Reports* 8, 2162.
- Zhuang, K., Vemuri, G.N., and Mahadevan, R. (2011). Economics of membrane occupancy and respiro-fermentation. *Molecular Systems Biology* 7, 500.

Figures

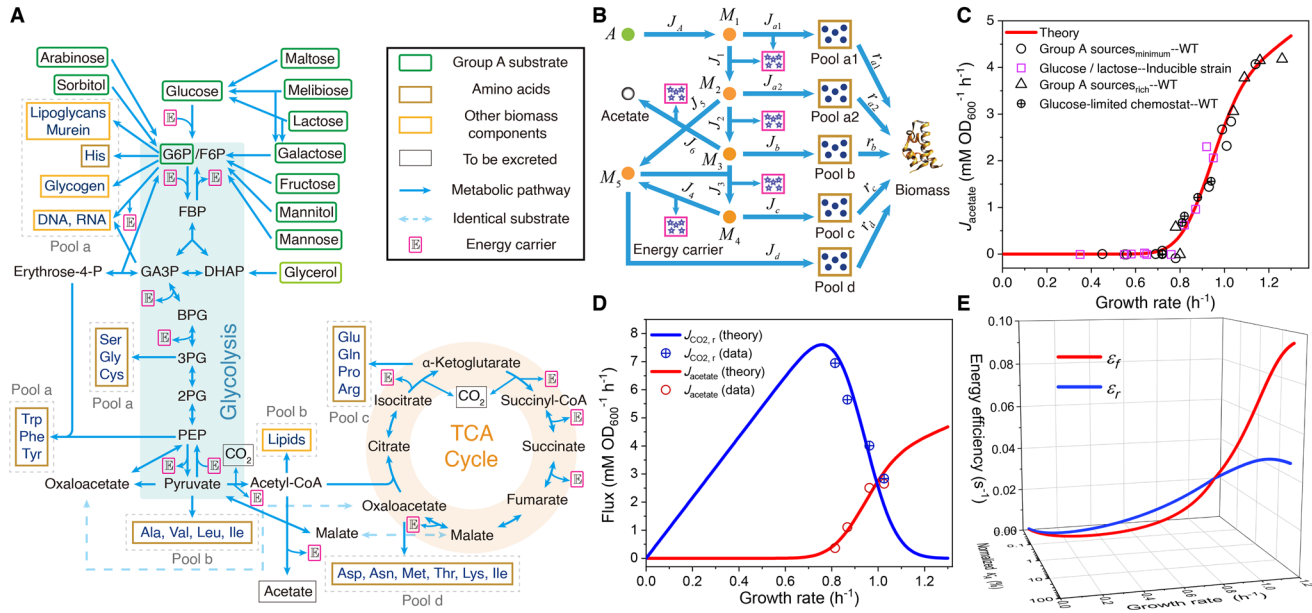


Fig. 1 | Model and results of overflow metabolism in *E. coli*. (A) The central metabolic network of carbon source utilization. The Group A carbon sources (Wang et al., 2019) are labeled with green squares. (B) Coarse-grained model for Group A carbon source utilization. (C) Model predictions (see Eqs. S47 and S160) and experimental results (Basan et al., 2015; Holms, 1996) of overflow metabolism, covering the data for all the Group A carbon sources shown in (A). (D) Growth rate dependence of respiration and fermentation fluxes (see Eqs. S47 and S160). (E) The proteome efficiencies for energy biogenesis in the respiration and fermentation pathways vary with growth rate as functions of the substrate quality of a Group A carbon source (see Eqs. S31 and S36). See Appendices 8 and 10 for model parameter settings and experimental data sources (Basan et al., 2015; Holms, 1996; Hui et al., 2015) for Figs. 1-4 of *E. coli*.

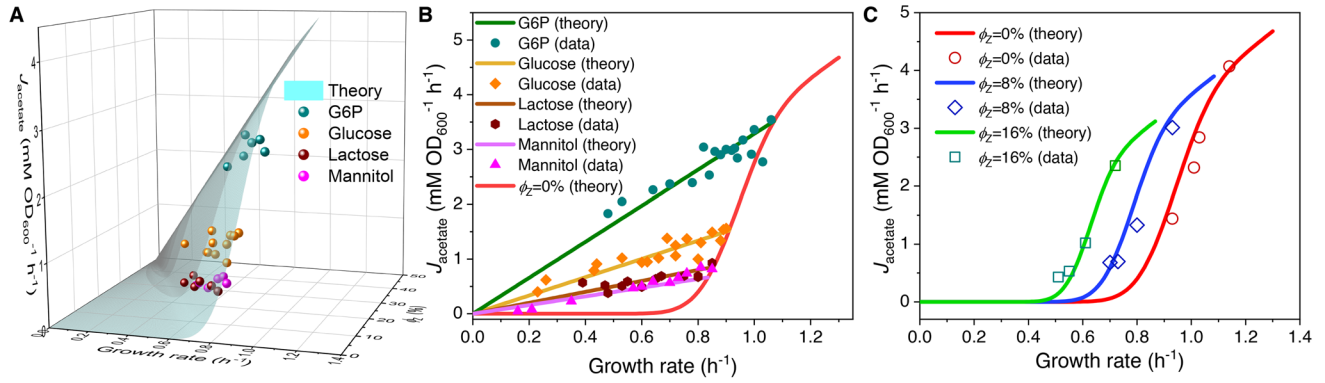


Fig. 2 | Influence of protein overexpression on overflow metabolism in *E. coli*. (A) A 3D plot of the relations among fermentation flux, growth rate, and the expression level of useless proteins. In this plot, both the acetate excretion rate and growth rate vary as bivariate functions of the nutrient quality of a Group A carbon source (denoted as κ_A) and the useless protein expression encoded by *lacZ* gene (denoted as ϕ_z perturbation; see Eqs. S57 and S160). (B) Growth rate dependence of the acetate excretion rate upon ϕ_z perturbation for each fixed nutrient condition (see Eqs. S58 and S160). (C) Growth rate dependence of the acetate excretion rate as κ_A varies (see Eqs. S57 and S160), with each fixed expression level of LacZ.

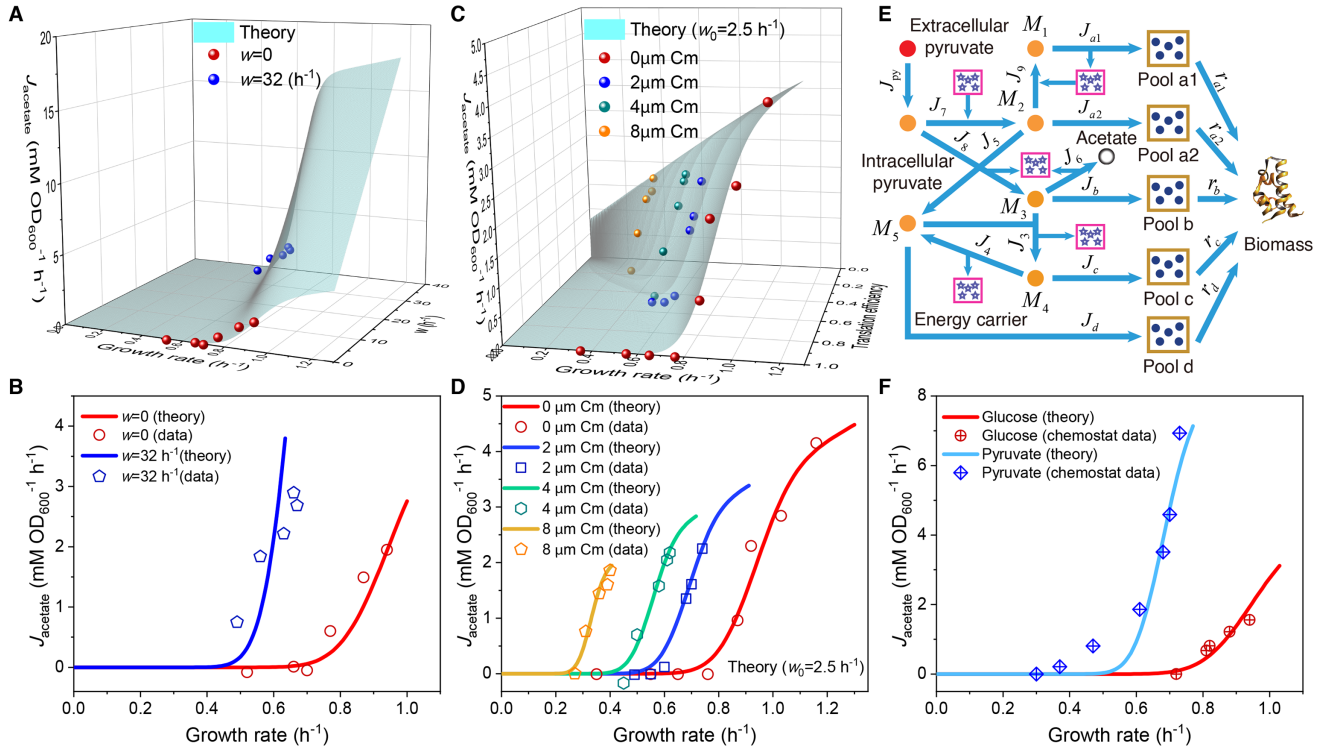


Fig. 3 | Influence of energy dissipation, translation inhibition, and carbon source category alteration on overflow metabolism in *E. coli*. (A) A 3D plot of the relations among fermentation flux, growth rate, and the energy dissipation coefficient (see Eqs. S70 and S160). (B) Growth rate dependence of the acetate excretion rate as the nutrient quality κ_A varies, with each fixed energy dissipation coefficient determined by or fitted from experimental data. (C) A 3D plot of the relations among fermentation flux, growth rate, and the translation efficiency (see Eqs. 85 and S160). Here, the translation efficiency is adjusted by the dose of chloramphenicol (Cm). (D) Growth rate dependence of the acetate excretion rate as κ_A varies, with each fixed dose of Cm. (E) Coarse-grained model for pyruvate utilization. (F) The growth rate dependence of fermentation flux in pyruvate (see Eqs. 105 and S160) significantly differs from that of the Group A carbon sources (see Eqs. 47 and S160).

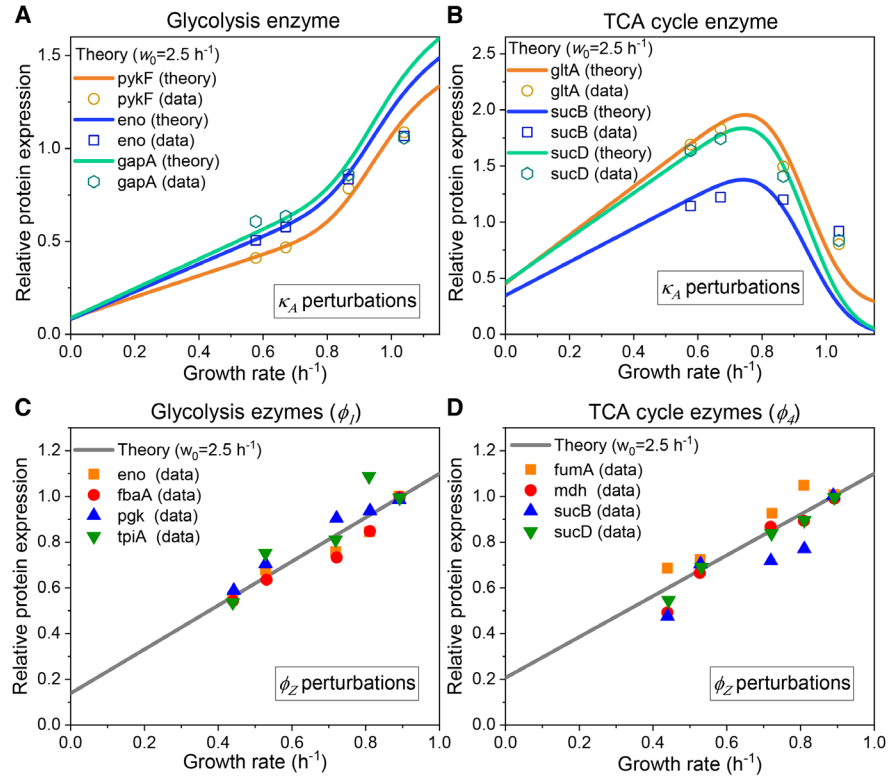


Fig. 4 | Relative protein expression of central metabolic enzymes in *E. coli* under nutrient limitation and proteomic perturbation. (A, C) Relative protein expression of representative genes from glycolysis. (B, D) Relative protein expression of representative genes from the TCA cycle. (A, B) Results of the perturbation through changes in nutrient quality κ_A (see Eq. S119). (C, D) Results of proteomic perturbation via varied levels of expression of the useless protein LacZ (i.e., ϕ_Z perturbation; see Eq. S121).

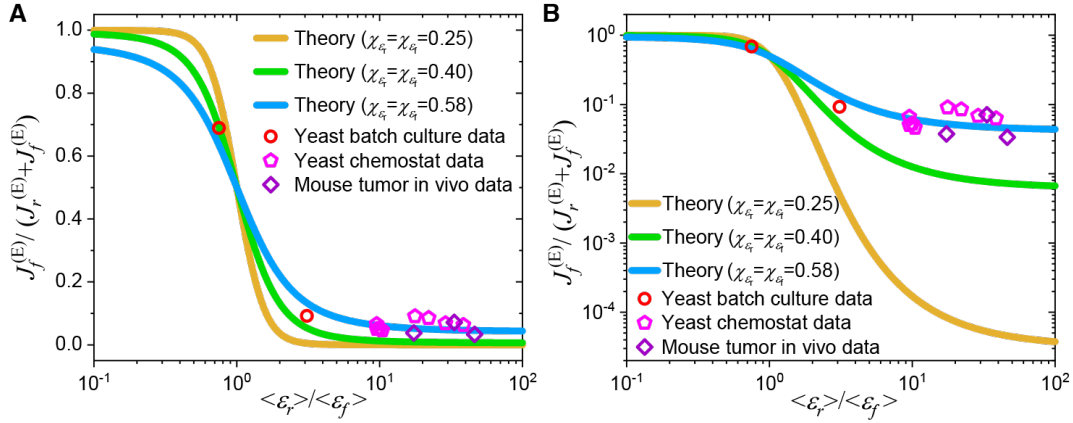


Fig. 5 | Model comparison with data on the Crabtree effect in yeast and the Warburg effect in tumors. (A) A linear scale representation on the y-axis. (B) A log scale representation on the y-axis. In (A-B), $\langle \varepsilon_r \rangle$ and $\langle \varepsilon_f \rangle$ represent the population averages of ε_r and ε_f , while χ_{ε_r} and χ_{ε_f} are the coefficients of variation (CVs) of ε_r and ε_f . $\langle \varepsilon_r \rangle / \langle \varepsilon_f \rangle$ represents the ratio of proteome efficiency between respiration and fermentation at the population-averaged level, while $J_f^{(E)} / (J_r^{(E)} + J_f^{(E)})$ stands for the fraction of energy flux generated by the fermentation pathway (see Eq. 6). The data for yeast in batch culture and chemostat were calculated from experimental data of *S. cerevisiae* and *I. orientalis* (Shen et al., 2024). The data for mouse tumors were calculated from in vivo experimental data of pancreatic ductal adenocarcinoma (PDAC) and leukemic spleen of mice (Bartman et al., 2023; Shen et al., 2024). See Appendix 10 for detailed information on the experimental data sources (Bartman et al., 2023; Shen et al., 2024).

Appendices for

Overflow metabolism originates from growth optimization and cell heterogeneity

Xin Wang*

*Correspondence: wangxin36@mail.sysu.edu.cn

This PDF file includes:

Appendices 1-10
Appendix-figures 1-5
Appendix-tables 1-3
Appendix References

Other supporting materials for this manuscript include the following:

Appendix-source data 1-2

Appendix 1 Model framework.....	1
Appendix 1.1 Proteome partition.....	1
Appendix 1.2 Precursor pools	1
Appendix 1.3 Stoichiometric flux	2
Appendix 1.4 Carbon flux and cell growth rate	2
Appendix 1.5 Intermediate nodes.....	4
Appendix 2 Model and analysis.....	4
Appendix 2.1 Coarse-grained model	4
Appendix 2.2 The reason for overflow metabolism.....	8
Appendix 2.3 The relation between respiration/fermentation flux and growth rate	10
Appendix 2.4 Dependence of the model on optimization principles	12
Appendix 3 Model perturbations	13
Appendix 3.1 Overexpression of useless proteins.....	13
Appendix 3.2 Energy dissipation.....	15
Appendix 3.3 Translation inhibition.....	17
Appendix 4 Overflow metabolism in substrates other than Group A carbon sources.....	21
Appendix 4.1 Pyruvate	21
Appendix 4.2 Mixture of a Group A carbon source with extracellular amino acids.....	25
Appendix 5 Enzyme allocation upon perturbations.....	28
Appendix 5.1 Carbon limitation within Group A carbon sources.....	28
Appendix 5.2 Overexpression of useless proteins.....	29
Appendix 5.3 Energy dissipation.....	30
Appendix 6 Other aspects of the model.....	32
Appendix 6.1 A coarse-grained model with more details	32
Appendix 6.2 Estimation of the in vivo enzyme catalytic rates	33
Appendix 6.3 Comparison with existing models that illustrate experimental results	34
Appendix 7 Probability density functions of variables and parameters	36
Appendix 7.1 Probability density function of κ_i	36
Appendix 7.2 Probability density function of the growth rate λ	39

Appendix 8 Model comparison with experiments on <i>E. coli</i>	40
Appendix 8.1 Flux comparison with experiments on <i>E. coli</i>	40
Appendix 8.2 Model parameter settings using experimental data of <i>E. coli</i>	41
Appendix 9 Explanation of the Crabtree effect in yeast and the Warburg effect in tumors.....	44
Appendix 10 Notes on the application of reference data.....	50
Appendix Tables	52
Appendix-table 1. Molecular weight and in vivo/ in vitro k_{cat} data for <i>E. coli</i>	52
Appendix-table 2. Proteome and flux data used to calculate the in vivo k_{cat} of <i>E. coli</i>	54
Appendix-table 3. Illustrations of symbols in this manuscript.....	55
Appendix Figures.....	59
Appendix-figure 1. Central metabolic network and carbon utilization pathways of <i>E. coli</i> ..	59
Appendix-figure 2. Model and results for experimental comparison of <i>E. coli</i>	60
Appendix-figure 3. Relative protein expression of central metabolic enzymes in <i>E. coli</i> under various types of perturbations.	62
Appendix-figure 4. Asymptotic distributions of inverse Gaussian distribution and the inverse of Gaussian distribution.....	64
Appendix-figure 5. Carbon utilization in yeast and mammalian cells.	65
Appendix References	66

Appendix 1 Model framework

Appendix 1.1 Proteome partition

Here we adopt the proteome partition framework similar to that introduced by Scott *et al.* (Scott *et al.*, 2010). All proteins in a cell are classified into three classes: the fixed portion Q-class, the active ribosome-affiliated R-class, and the remaining catabolic/anabolic enzymes C-class. Each proteome class has a mass $M_i^{(P)}$ ($i = Q, R, C$) and mass fraction ϕ_i , where ϕ_Q is a constant, and we define $\phi_{\max} \equiv 1 - \phi_Q$. In the exponential growth phase, the ribosome allocation for protein synthesis of each class is f_i , with $f_Q + f_R + f_C = 1$.

To analyze cell growth optimization, we first consider the homogeneous case where all cells share identical biochemical parameters, simplifying the mass accumulation of the cell population into a “big cell”. This simplification does not affect the value of growth rate λ . For bacteria, the protein turnover is negligible, so the mass accumulation of each class follows:

$$dM_i^{(P)}/dt = f_i \cdot k_T \cdot N_R \cdot m_{AA} \quad (i = Q, R, C), \quad (S1)$$

where m_{AA} stands for the average molecular weight of amino acids, k_T is the translation rate, $N_R = M_{ip}^{(P)}/m_R$ is the number of ribosomes, m_R is the protein mass of a single ribosome, and $M_{ip}^{(P)}$ is the total protein mass of ribosomes, with $M_R^{(P)}/M_{ip}^{(P)} = \zeta \approx 1.67$ (Neidhardt, 1996; Scott *et al.*, 2010). For a specific stable nutrient environment, f_R and k_T are temporal invariants. Thus,

$$M_i^{(P)}(t) = M_i^{(P)}(0) + f_i/f_R \cdot M_R^{(P)}(0) \cdot [\exp(\lambda \cdot t) - 1] \quad (i = Q, R, C), \quad (S2)$$

where $\lambda = f_R \cdot k_T \cdot m_{AA}/(\zeta \cdot m_R)$, and the total protein mass of the cell population $M_{\text{protein}} \equiv \sum_i^{Q,R,C} M_i^{(P)}$ follows:

$$M_{\text{protein}}(t) = M_{\text{protein}}(0) + M_R(0) \cdot [\exp(\lambda \cdot t) - 1]/f_R. \quad (S3)$$

Over a long period in the exponential growth phase (i.e., $t \rightarrow +\infty$), we have $\phi_i = f_i$ ($i = Q, R, C$), and

$$\lambda = \phi_R \cdot \kappa_t, \quad (S4)$$

where $\kappa_t = k_T \cdot m_{AA}/(\zeta \cdot m_R)$.

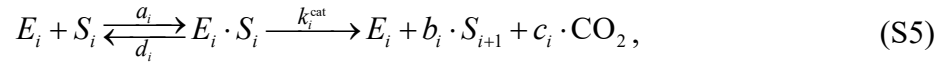
Appendix 1.2 Precursor pools

Based on the entry points of the metabolic network, we classify the precursors of biomass components into five pools (Fig. 1A-B): a1 (entry point: G6P/F6P), a2 (entry point:

GA3P/3PG/PEP), b (entry point: pyruvate/acetyl-CoA), c (entry point: α -ketoglutarate), and d (entry point: oxaloacetate). These five pools draw approximately $r_{a1} = 24\%$, $r_{a2} = 24\%$, $r_b = 28\%$, $r_c = 12\%$ and $r_d = 12\%$ of the carbon flux (Nelson et al., 2008; Wang et al., 2019). There are overlapping components between Pools a1 and a2 due to the joint synthesis of some precursors. Therefore, we use Pool a to represent both Pools a1 and a2 in the descriptions.

Appendix 1.3 Stoichiometric flux

We consider the following biochemical reaction between substrate S_i and enzyme E_i :



where a_i , d_i and k_i^{cat} are the reaction parameters, S_{i+1} is the product, b_i and c_i are the stoichiometric coefficients. For most of the reactions in the central metabolism, $b_i = 1$ and $c_i = 0$. The reaction rate follows Michaelis–Menten kinetics (Nelson et al., 2008):

$$v_i = k_i^{\text{cat}} \cdot [E_i] \cdot \frac{[S_i]}{[S_i] + K_i}, \quad (\text{S6})$$

where $K_i \equiv (d_i + k_i^{\text{cat}})/a_i$, $[E_i]$ and $[S_i]$ are the Michaelis constant, and the concentrations of enzyme E_i and substrate S_i , respectively. For this reaction (Eq. S5), $d[S_{i+1}]/dt = b_i \cdot v_i$ and $d[S_i]/dt = -v_i$. In the cell population (the “big cell”), suppose that the cell volume is V_{cell} , then the stoichiometric flux of the reaction is:

$$J_i \equiv V_{\text{cell}} \cdot v_i. \quad (\text{S7})$$

The copy number of enzyme E_i is $N_{E_i} = V_{\text{cell}} \cdot [E_i]$ with a total weight of $M_{E_i} = N_{E_i} \cdot m_{E_i}$, where m_{E_i} is the molecular weight of E_i . By defining the enzyme cost of an E_i molecule as $n_{E_i} \equiv m_{E_i}/m_0$, where m_0 is a unit mass, then the cost of all E_i molecules is $\Phi_i \equiv N_{E_i} \cdot n_{E_i}$ (Wang et al., 2019). By further defining $\xi_i \equiv \frac{k_i^{\text{cat}}}{n_{E_i}} \cdot \frac{[S_i]}{[S_i] + K_i}$, then:

$$J_i = \Phi_i \cdot \xi_i. \quad (\text{S8})$$

The mass fraction of enzyme E_i in the proteome is $\phi_i = M_{E_i}/M_{\text{protein}}$, and thus:

$$\phi_i = \Phi_i \cdot \frac{m_0}{M_{\text{protein}}}. \quad (\text{S9})$$

Appendix 1.4 Carbon flux and cell growth rate

To clarify the relation between the stoichiometric flux J_i and growth rate λ , we consider the carbon flux in the biomass production. The carbon mass of the cell population (the “big cell”) is given by $M_{\text{carbon}} = M_{\text{protein}} \cdot r_{\text{carbon}} / r_{\text{protein}}$, where r_{carbon} and r_{protein} represent the mass fraction of carbon and protein within a cell. In the exponential growth phase, the carbon flux of the biomass production is given by:

$$J_{\text{BM}} = \frac{1}{m_{\text{carbon}}} \cdot \frac{dM_{\text{carbon}}}{dt} = \lambda \cdot \frac{M_{\text{carbon}}}{m_{\text{carbon}}}, \quad (\text{S10})$$

where m_{carbon} is the mass of a carbon atom. In fact, the carbon mass flux per stoichiometry varies depending on the entry point of the precursor pool. Taking Pool b as an example, there are three carbon atoms in a molecule of the entry point metabolite (i.e., pyruvate). Assuming that carbon atoms are conserved from pyruvate to Pool b, then the carbon flux of Pool b is given by $J_b^{\text{carbon}} = J_b \cdot N_{\text{py}}^{\text{carbon}}$, where J_b is the stoichiometric flux from pyruvate to Pool b (Fig. 1A-B) and $N_{\text{py}}^{\text{carbon}}$ stands for the carbon number of a pyruvate molecule. Combining with Eq. S10 and noting that $J_b^{\text{carbon}} = r_b \cdot J_{\text{BM}}$, we get $J_b \cdot N_{\text{py}}^{\text{carbon}} \cdot m_{\text{carbon}} = r_b \cdot \lambda \cdot M_{\text{carbon}}$. Similarly, for each precursor pool, we have:

$$J_i \cdot N_{\text{EP}_i}^{\text{carbon}} \cdot m_{\text{carbon}} = r_i \cdot \lambda \cdot M_{\text{carbon}} \quad (i = a1, a2, b, c, d), \quad (\text{S11})$$

where the subscript “EP_{*i*}” represents the entry point of Pool *i*, and $N_{\text{EP}_i}^{\text{carbon}}$ is the number of carbon atoms in a molecule of the entry-point metabolite.

For each substrate in intermediate steps of the metabolic network, we define κ_i as the substrate quality:

$$\kappa_i \equiv \xi_i \cdot \frac{r_{\text{protein}}}{r_{\text{carbon}}} = \frac{r_{\text{protein}}}{r_{\text{carbon}}} \cdot \frac{k_i^{\text{cat}}}{n_{E_i}} \cdot \frac{[S_i]}{[S_i] + K_i}, \quad (\text{S12})$$

and for each precursor pool, we define:

$$\eta_i \equiv r_i \cdot m_0 / (N_{\text{EP}_i}^{\text{carbon}} \cdot m_{\text{carbon}}) \quad (i = a1, a2, b, c, d). \quad (\text{S13})$$

Combining Eqs. S8, S9 and S11, we have

$$\phi_i \cdot \kappa_i = \eta_i \cdot \lambda \quad (i = a1, a2, b, c, d). \quad (\text{S14})$$

Then, we define the normalized flux, which can be regarded as the flux per unit of biomass:

$$J_i^{(\text{N})} \equiv \phi_i \cdot \kappa_i, \quad (\text{S15})$$

where the superscript “(N)” stands for normalized. Combined with Eqs. S8, S9 and S12, we have:

$$J_i^{(N)} \equiv J_i \cdot \frac{m_0}{M_{\text{carbon}}}. \quad (\text{S16})$$

Since $\sum_i^{a1,a2,b,c,d} r_i = 1$, by setting

$$m_0 = \left[\sum_i r_i / N_{EP_i}^{\text{carbon}} \right]^{-1} \cdot m_{\text{carbon}}, \quad (\text{S17})$$

we then obtain:

$$\eta_i = \frac{r_i}{N_{EP_i}^{\text{carbon}}} \cdot \left[\sum_j^{a1,a2,b,c,d} \frac{r_j}{N_{EP_j}^{\text{carbon}}} \right]^{-1} \quad (i = a1, a2, b, c, d), \quad (\text{S18})$$

and we have $\sum_i^{a1,a2,b,c,d} \eta_i = 1$, and

$$\sum_i^{a1,a2,b,c,d} \phi_i \cdot \kappa_i = \lambda. \quad (\text{S19})$$

Appendix 1.5 Intermediate nodes

In a metabolic network, the metabolites between the carbon source and precursor pools are referred to as intermediate nodes. As specified by Wang *et al.* (Wang et al., 2019), to optimize cell growth rate, the substrate of each intermediate node is nearly saturated, and thus:

$$\kappa_i \approx \frac{r_{\text{protein}}}{r_{\text{carbon}}} \cdot \frac{k_i^{\text{cat}}}{n_{E_i}}. \quad (\text{S20})$$

Real cases could be more complicated due to other forms of metabolic regulations. Recent quantitative studies (Bennett et al., 2009; Park et al., 2016) have shown that, at least in *E. coli*, for most of the substrate-enzyme pairs, K_i is lower than the substrate concentration (i.e.,

$[S_i] > K_i$), which implies $\kappa_i \approx \frac{r_{\text{protein}}}{r_{\text{carbon}}} \cdot \frac{k_i^{\text{cat}}}{n_{E_i}}$.

Appendix 2 Model and analysis

Appendix 2.1 Coarse-grained model

In the coarse-grained model shown in Fig. 1B, node *A* represents an arbitrary carbon source of Group A (Wang et al., 2019), which joins at the upper part of glycolysis. Nodes M1, M2, M3, M4, and M5 stand for G6P, PEP, acetyl-CoA, α -ketoglutarate, and oxaloacetate, respectively. In the analysis of carbon supply into precursor pools, we lump sum G6P/F6P as M1, GA3P/3PG/PEP as M2, and pyruvate/acetyl-CoA as M3 for approximation. For the biochemical

reactions, each follows Eq. S5 with $b_i = 1$ except for $M1 \rightarrow 2M2$ and $M3+M5 \rightarrow M4$. Basically, there are three independent possible fates for a Group A carbon source (e.g., glucose, see Appendix-fig. 1C-E) (Chen and Nielsen, 2019): energy biogenesis through fermentation; energy biogenesis via respiration (Appendix-fig.1C-D), or conversion into biomass components accompanied by energy biogenesis in the biomass pathway. Each fate involves a distinct fraction of the proteome, with no overlap between them (Appendix-fig. 1).

By applying flux balance to the stoichiometric fluxes and combining with Eq. S8, we have:

$$\begin{cases} \Phi_A \cdot \xi_A = \Phi_1 \cdot \xi_1 + \Phi_{a1} \cdot \xi_{a1}, \\ 2\Phi_1 \cdot \xi_1 = \Phi_2 \cdot \xi_2 + \Phi_5 \cdot \xi_5 + \Phi_{a2} \cdot \xi_{a2}, \\ \Phi_2 \cdot \xi_2 = \Phi_3 \cdot \xi_3 + \Phi_6 \cdot \xi_6 + \Phi_b \cdot \xi_b, \\ \Phi_5 \cdot \xi_5 + \Phi_4 \cdot \xi_4 = \Phi_3 \cdot \xi_3 + \Phi_d \cdot \xi_d, \\ \Phi_3 \cdot \xi_3 = \Phi_4 \cdot \xi_4 + \Phi_c \cdot \xi_c. \end{cases} \quad (\text{S21})$$

Obviously, the stoichiometric fluxes of respiration J_r and fermentation J_f (Appendix-fig. 1C-D) are:

$$\begin{cases} J_r \equiv J_4 = \Phi_4 \cdot \xi_4, \\ J_f \equiv J_6 = \Phi_6 \cdot \xi_6. \end{cases} \quad (\text{S22})$$

We further assume that the carbon atoms are conserved from each entry point metabolite to the precursor pool, and then,

$$\Phi_i \cdot \xi_i \cdot N_{EP_i}^{\text{carbon}} = r_i \cdot J_{\text{BM}} \quad (i = a1, a2, b, c, d). \quad (\text{S23})$$

In terms of energy biogenesis for the relevant reactions, for convenience, we convert all the energy currencies into ATPs, namely, $\text{NADH} \rightarrow 2\text{ATP}$ (Neidhardt et al., 1990), $\text{NADPH} \rightarrow 2\text{ATP}$ (Neidhardt et al., 1990; Sauer et al., 2004), $\text{FADH}_2 \rightarrow 1\text{ATP}$ (Neidhardt et al., 1990). Then, we have

$$\beta_1 \cdot \Phi_1 \cdot \xi_1 + \beta_2 \cdot \Phi_2 \cdot \xi_2 + \beta_3 \cdot \Phi_3 \cdot \xi_3 + \beta_4 \cdot \Phi_4 \cdot \xi_4 + \beta_6 \cdot \Phi_6 \cdot \xi_6 + \beta_{a1} \cdot \Phi_{a1} \cdot \xi_{a1} = J_E, \quad (\text{S24})$$

where J_E represents the energy demand for cell proliferation, expressed as the stoichiometric energy flux in ATP. β_i is the stoichiometric coefficient with $\beta_1 = 4$, $\beta_2 = 3$, $\beta_3 = 2$, $\beta_4 = 6$, $\beta_6 = 1$, and $\beta_{a1} = 4$ for *E. coli* (Neidhardt et al., 1990; Sauer et al., 2004). For bacteria, the energy demand is generally proportional to the carbon flux infused into biomass production, as the proportion of maintenance energy is roughly negligible (Locasale and Cantley, 2010). Thus,

$$J_E = r_E \cdot J_{\text{BM}}, \quad (\text{S25})$$

where r_E is the ratio and also a constant.

By applying the substitutions specified in Eqs. S9, S12, S14-S18, combined with Eqs. S4, S10, S21-S25, and the constraint of proteome resource allocation $\phi_R + \phi_C = \phi_{\max}$, we have:

$$\left\{ \begin{array}{l} \phi_A \cdot \kappa_A = \phi_1 \cdot \kappa_1 + \phi_{a1} \cdot \kappa_{a1}, \\ 2\phi_1 \cdot \kappa_1 = \phi_2 \cdot \kappa_2 + \phi_5 \cdot \kappa_5 + \phi_{a2} \cdot \kappa_{a2}, \\ \phi_2 \cdot \kappa_2 = \phi_3 \cdot \kappa_3 + \phi_6 \cdot \kappa_6 + \phi_b \cdot \kappa_b, \\ \phi_5 \cdot \kappa_5 + \phi_4 \cdot \kappa_4 = \phi_3 \cdot \kappa_3 + \phi_d \cdot \kappa_d, \\ \phi_3 \cdot \kappa_3 = \phi_4 \cdot \kappa_4 + \phi_c \cdot \kappa_c, \\ \phi_{a1} \cdot \kappa_{a1} = \eta_{a1} \cdot \lambda, \phi_{a2} \cdot \kappa_{a2} = \eta_{a2} \cdot \lambda, \phi_b \cdot \kappa_b = \eta_b \cdot \lambda, \phi_c \cdot \kappa_c = \eta_c \cdot \lambda, \phi_d \cdot \kappa_d = \eta_d \cdot \lambda, \\ \beta_1 \cdot \phi_1 \cdot \kappa_1 + \beta_2 \cdot \phi_2 \cdot \kappa_2 + \beta_3 \cdot \phi_3 \cdot \kappa_3 + \beta_4 \cdot \phi_4 \cdot \kappa_4 + \beta_6 \cdot \phi_6 \cdot \kappa_6 + \beta_{a1} \cdot \phi_{a1} \cdot \kappa_{a1} = J_E^{(N)}, \\ J_E^{(N)} = \eta_E \cdot \lambda, \lambda = \phi_R \cdot \kappa_t, J_r^{(N)} = \phi_4 \cdot \kappa_4, J_f^{(N)} = \phi_6 \cdot \kappa_6, \\ \phi_R + \phi_A + \phi_1 + \phi_2 + \phi_3 + \phi_4 + \phi_5 + \phi_6 + \phi_{a1} + \phi_{a2} + \phi_b + \phi_c + \phi_d = \phi_{\max}, \end{array} \right. \quad (\text{S26})$$

where $J_E^{(N)}$ and η_E are defined as $J_E^{(N)} \equiv J_E \cdot \frac{m_0}{M_{\text{carbon}}}$ and $\eta_E \equiv r_E \cdot \left[\sum_i r_i / N_{\text{EP}_i}^{\text{carbon}} \right]^{-1}$, respectively.

Here, for each intermediate node, κ_i follows Eq. S20, which can be approximated as a constant. The substrate quality of the Group A carbon source κ_A varies with the identity and concentration of the Group A carbon source:

$$\kappa_A \equiv \frac{r_{\text{protein}}}{r_{\text{carbon}}} \cdot \frac{k_A^{\text{cat}}}{m_{E_A}} \cdot \frac{[A]}{[A] + K_A} \cdot m_0, \quad (\text{S27})$$

which is determined externally by the culture condition. From Eq. S26, all ϕ_i and ϕ_R can be expressed in terms of $J_r^{(N)}$, $J_f^{(N)}$, and λ :

$$\left\{ \begin{array}{l} \phi_A = \left[J_r^{(N)} + J_f^{(N)} + (2\eta_{a1} + \eta_{a2} + \eta_b + 2\eta_c + \eta_d) \lambda \right] / (2 \cdot \kappa_A), \\ \phi_1 = \left[J_r^{(N)} + J_f^{(N)} + (\eta_{a2} + \eta_b + 2\eta_c + \eta_d) \lambda \right] / (2 \cdot \kappa_1), \\ \phi_2 = \left[J_r^{(N)} + J_f^{(N)} + (\eta_b + \eta_c) \lambda \right] / \kappa_2, \\ \phi_3 = (J_r^{(N)} + \eta_c \cdot \lambda) / \kappa_3, \phi_4 = J_r^{(N)} / \kappa_4, \\ \phi_5 = (\eta_c + \eta_d) \lambda / \kappa_5, \phi_6 = J_f^{(N)} / \kappa_6, \phi_R = \lambda / \kappa_t, \\ \phi_i = \eta_i \cdot \lambda / \kappa_i \quad (i = a1, a2, b, c, d). \end{array} \right. \quad (\text{S28})$$

In Eq. S28, for each ϕ_i or ϕ_R , the $J_r^{(N)}$ - and $J_f^{(N)}$ -related proteome fraction terms belong to the fractions of the proteome dedicated to respiration (denoted as ϕ_r) and fermentation (denoted as ϕ_f), respectively. The λ -related proteome fraction terms belong to those involved in the

biomass synthesis pathway (denoted as ϕ_{BM}). Thus, $\phi_r = J_r^{(N)} \cdot [1/(2 \cdot \kappa_A) + 1/(2 \cdot \kappa_1) + 1/\kappa_2 + 1/\kappa_3 + 1/\kappa_4]$, $\phi_f = J_f^{(N)} \cdot [1/(2 \cdot \kappa_A) + 1/(2 \cdot \kappa_1) + 1/\kappa_2 + 1/\kappa_6]$, and $\phi_{\text{BM}} = \lambda \cdot \left(\frac{1}{\kappa_t} + \frac{1 + \eta_{a1} + \eta_c}{2\kappa_A} + \frac{1 - \eta_{a1} + \eta_c}{2\kappa_1} + \frac{\eta_b + \eta_c}{\kappa_2} + \frac{\eta_c}{\kappa_3} + \frac{\eta_c + \eta_d}{\kappa_5} + \sum_i^{a1,a2,b,c,d} \frac{\eta_i}{\kappa_i} \right)$. By substituting Eq. S28 into Eq. S26, we have:

$$\begin{cases} J_r^{(E)} + J_f^{(E)} = \varphi \cdot \lambda, \\ \frac{J_r^{(E)}}{\varepsilon_r} + \frac{J_f^{(E)}}{\varepsilon_f} = \phi_{\text{max}} - \psi \cdot \lambda. \end{cases} \quad (\text{S29})$$

Here, $J_r^{(E)}$ and $J_f^{(E)}$ stand for the normalized energy fluxes of respiration and fermentation, with

$$\begin{cases} J_r^{(E)} = \beta_r^{(A)} \cdot J_r^{(N)} / 2, \\ J_f^{(E)} = \beta_f^{(A)} \cdot J_f^{(N)} / 2, \end{cases} \quad (\text{S30})$$

where $\beta_r^{(A)} = \beta_1 + 2(\beta_2 + \beta_3 + \beta_4)$ and $\beta_f^{(A)} = \beta_1 + 2(\beta_2 + \beta_6)$, with $\beta_r^{(A)} = 26$ and $\beta_f^{(A)} = 12$ for *E. coli*. ε_r and ε_f represent the proteome efficiencies for energy biogenesis in the respiration and fermentation pathways (Appendix-fig. 1C-D), defined as $\varepsilon_r \equiv J_r^{(E)} / \phi_r$ and $\varepsilon_f \equiv J_f^{(E)} / \phi_f$; that is, the normalized energy fluxes expressed in ATP generated per proteomic mass fraction dedicated to respiration and fermentation, respectively. Hence,

$$\begin{cases} \varepsilon_r = \frac{\beta_r^{(A)}}{1/\kappa_A + 1/\kappa_1 + 2/\kappa_2 + 2/\kappa_3 + 2/\kappa_4}, \\ \varepsilon_f = \frac{\beta_f^{(A)}}{1/\kappa_A + 1/\kappa_1 + 2/\kappa_2 + 2/\kappa_6}. \end{cases} \quad (\text{S31})$$

ψ^{-1} is the proteome efficiency for biomass generation in the biomass synthesis pathway (Appendix-fig. 1E), defined as $\psi^{-1} \equiv \lambda / \phi_{\text{BM}} = \sum_i^{a1,a2,b,c,d} J_i^{(N)} / \phi_{\text{BM}}$ (see Eqs. S15 and S19); that is, the normalized flux (which differs from the normalized energy flux used to define ε_r and ε_f) generated per proteomic mass fraction dedicated to biomass synthesis. Hence

$$\psi = \frac{1}{\kappa_t} + \frac{1 + \eta_{a1} + \eta_c}{2\kappa_A} + \frac{\eta_{a2} + \eta_b + 2\eta_c + \eta_d}{2\kappa_1} + \frac{\eta_b + \eta_c}{\kappa_2} + \frac{\eta_c}{\kappa_3} + \frac{\eta_c + \eta_d}{\kappa_5} + \sum_i^{a1,a2,b,c,d} \frac{\eta_i}{\kappa_i}. \quad (\text{S32})$$

φ is an energy demand coefficient (a constant), with

$$\varphi \equiv \eta_E - \beta_1 \cdot (\eta_{a2} + \eta_b + 2\eta_c + \eta_d) / 2 - \beta_2 \cdot (\eta_b + \eta_c) - \beta_3 \cdot \eta_c - \beta_{a1} \cdot \eta_{a1}, \quad (\text{S33})$$

and $\varphi \cdot \lambda$ stands for the normalized flux of energy demand other than the accompanying energy biogenesis from the biomass synthesis pathway.

Appendix 2.2 The reason for overflow metabolism

Microbes optimize their growth rate to survive through the evolutionary process (Vander Heiden et al., 2009). The optimal growth principle also roughly holds for tumor cells, which proliferate while ignoring growth restriction signals and evading immune destruction by the host (Vander Heiden et al., 2009). First, we consider the optimal growth strategy for a single cell. The coarse-grained model for bacteria is summarized in Eq. S26 and further simplified in Eq. S29. Here, ε_r , ε_f and ψ are functions of κ_A (see Eqs. S31, S32), so we also denote them as $\varepsilon_r(\kappa_A)$, $\varepsilon_f(\kappa_A)$, $\psi(\kappa_A)$. Evidently, the fluxes of both respiration and fermentation take non-negative values, i.e., $J_r^{(E)}, J_f^{(E)} \geq 0$, and all the coefficients are positive: $\varepsilon_r(\kappa_A), \varepsilon_f(\kappa_A), \psi(\kappa_A), \varphi > 0$.

Thus, if $\varepsilon_r > \varepsilon_f$, then $(\psi + \varphi/\varepsilon_r) \cdot \lambda = \phi_{\max} - J_f^{(E)}(1/\varepsilon_f - 1/\varepsilon_r) \leq \phi_{\max}$. Obviously, the solution for optimal growth is:

$$\begin{cases} J_f^{(E)} = 0, \\ J_r^{(E)} = \varphi \cdot \lambda. \end{cases} \quad \varepsilon_r > \varepsilon_f. \quad (\text{S34})$$

Similarly, if $\varepsilon_f > \varepsilon_r$, then the optimal growth solution is:

$$\begin{cases} J_f^{(E)} = \varphi \cdot \lambda, \\ J_r^{(E)} = 0. \end{cases} \quad \varepsilon_r < \varepsilon_f. \quad (\text{S35})$$

In both cases, the growth rate λ takes the maximum value for a given nutrient condition (i.e., given κ_A):

$$\lambda = \begin{cases} \lambda_r \equiv \frac{\phi_{\max}}{\varphi/\varepsilon_r(\kappa_A) + \psi(\kappa_A)} & \varepsilon_r(\kappa_A) > \varepsilon_f(\kappa_A), \\ \lambda_f \equiv \frac{\phi_{\max}}{\varphi/\varepsilon_f(\kappa_A) + \psi(\kappa_A)} & \varepsilon_r(\kappa_A) < \varepsilon_f(\kappa_A). \end{cases} \quad (\text{S36})$$

So, why do microbes use the seemingly wasteful fermentation pathway when the growth rate is large under aerobic conditions? Prevalent explanations (Basan et al., 2015; Chen and Nielsen, 2019) suggest that it originates from that the proteome efficiency in fermentation is consistently higher than in respiration (i.e., $\varepsilon_f > \varepsilon_r$). If this is the case, why do microbes still use the normal respiration pathway when the growth rate is small? The answer lies in the fact that both $\varepsilon_r(\kappa_A)$ and $\varepsilon_f(\kappa_A)$ are not constants, but are dependent on nutrient conditions. In Eq. S31, when κ_A is small, consider the extreme case of $\kappa_A \rightarrow 0$, and then

$$\begin{cases} \varepsilon_r(\kappa_A \rightarrow 0) \approx \beta_r^{(A)} \cdot \kappa_A, \\ \varepsilon_f(\kappa_A \rightarrow 0) \approx \beta_f^{(A)} \cdot \kappa_A. \end{cases} \quad (\text{S37})$$

Since $\beta_r^{(A)} \gg \beta_f^{(A)}$, clearly,

$$\varepsilon_r(\kappa_A \rightarrow 0) > \varepsilon_f(\kappa_A \rightarrow 0). \quad (\text{S38})$$

Combined with Eq. S36, thus cells would certainly use the respiration pathway when the growth rate is very small. Meanwhile, suppose that κ_A^{\max} is the maximum value of κ_A available across different Group A carbon sources, and if there exists a κ_A (with $\kappa_A \leq \kappa_A^{\max}$) satisfying $\varepsilon_r(\kappa_A) < \varepsilon_f(\kappa_A)$, specifically,

$$\frac{\beta_r^{(A)} - \beta_f^{(A)}}{\kappa_A} < \beta_f^{(A)} \left(\frac{1}{\kappa_1} + \frac{2}{\kappa_2} + \frac{2}{\kappa_3} + \frac{2}{\kappa_4} \right) - \beta_r^{(A)} \cdot \left(\frac{1}{\kappa_1} + \frac{2}{\kappa_2} + \frac{2}{\kappa_6} \right), \quad (\text{S39})$$

then $\Delta(\kappa_A) \equiv \varepsilon_f(\kappa_A) / \varepsilon_r(\kappa_A)$ is a monotonically increasing function of κ_A . Thus,

$$\varepsilon_r(\kappa_A^{\max}) < \varepsilon_f(\kappa_A^{\max}), \quad (\text{S40})$$

and cells would use the fermentation pathway when the growth rate is large.

In practice, experimental studies using *E. coli* (Basan et al., 2015) have demonstrated that proteome efficiency in fermentation is higher than in respiration when the Group A carbon source is lactose at a saturated concentration, i.e., $\varepsilon_r(\kappa_{\text{lactose}}^{(\text{ST})}) < \varepsilon_f(\kappa_{\text{lactose}}^{(\text{ST})})$. Here, $\kappa_{\text{lactose}}^{(\text{ST})}$ represents the substrate quality of lactose and the superscript “(ST)” signifies saturated concentration. In fact, *E. coli* grows much faster in G6p than lactose (Basan et al., 2015), thus, $\kappa_A^{\max} > \kappa_{\text{lactose}}^{(\text{ST})}$, and hence, Eq. S40 holds for *E. coli*. From a theoretical perspective, we can verify Eq. S39 and consequently Eq. S40 using Eq. S20, combined with the in vivo/in vitro biochemical parameters obtained from experimental data (see Appendix-tables 1-2). For example, it is straightforward to confirm that $\varepsilon_r(\kappa_{\text{glucose}}^{(\text{ST})}) < \varepsilon_f(\kappa_{\text{glucose}}^{(\text{ST})})$ using this method (see Appendix 8.2), further supporting the validity of Eqs. S39-S40 (see also Appendix 9).

Now that Eqs. S38-S40 are all valid, a critical value of κ_A , denoted as $\kappa_A^{(C)}$, exists, satisfying $\Delta(\kappa_A^{(C)}) = 1$. Thus,

$$\begin{cases} \varepsilon_f(\kappa_A) > \varepsilon_r(\kappa_A), & \kappa_A > \kappa_A^{(C)}; \\ \varepsilon_f(\kappa_A) = \varepsilon_r(\kappa_A), & \kappa_A = \kappa_A^{(C)}; \\ \varepsilon_f(\kappa_A) < \varepsilon_r(\kappa_A), & \kappa_A < \kappa_A^{(C)}. \end{cases} \quad (\text{S41})$$

Combined with Eq. S31, we have:

$$\kappa_A^{(C)} = \frac{\beta_r^{(A)} - \beta_f^{(A)}}{\beta_f^{(A)} (1/\kappa_1 + 2/\kappa_2 + 2/\kappa_3 + 2/\kappa_4) - \beta_r^{(A)} (1/\kappa_1 + 2/\kappa_2 + 2/\kappa_6)}. \quad (\text{S42})$$

By substituting Eq. S42 into Eqs. S31, S32 and S36, we obtain the expressions for $\varepsilon_r(\kappa_A^{(C)})$, $\varepsilon_f(\kappa_A^{(C)})$ and the critical growth rate at the transition point (i.e., $\lambda_c \equiv \lambda(\kappa_A^{(C)})$):

$$\begin{cases} \varepsilon_r(\kappa_A^{(C)}) = \varepsilon_f(\kappa_A^{(C)}) = \frac{\beta_r^{(A)} - \beta_f^{(A)}}{2(1/\kappa_3 + 1/\kappa_4 - 1/\kappa_6)} = \frac{\beta_3 + \beta_4 - \beta_6}{1/\kappa_3 + 1/\kappa_4 - 1/\kappa_6}, \\ \lambda_c = \frac{\phi_{\max}}{\varphi/\varepsilon_{r/f}(\kappa_A^{(C)}) + \psi(\kappa_A^{(C)})}, \end{cases} \quad (\text{S43})$$

where $\varepsilon_{r/f}$ represents either ε_r or ε_f . In Fig. 1E, we show the dependencies of $\varepsilon_r(\kappa_A)$, $\varepsilon_f(\kappa_A)$ and $\lambda(\kappa_A)$ on κ_A in a 3-dimensional form, as κ_A changes.

Appendix 2.3 The relation between respiration/fermentation flux and growth rate

We proceed to study the relation between the respiration/fermentation flux and the cell growth rate. From Eqs. S16 and S30, we see that the stoichiometric fluxes J_r , J_f , the normalized fluxes $J_r^{(N)}$, $J_f^{(N)}$ and the normalized energy fluxes $J_r^{(E)}$, $J_f^{(E)}$ are all interconvertible. For convenience, we first analyze the relations between $J_r^{(E)}$, $J_f^{(E)}$ and λ under growth rate optimization. In fact, all these terms are merely functions of κ_A (see Eqs. S34-S36), which is determined by the nutrient condition (Eq. S27).

In the homogeneous case, where all microbes share identical biochemical parameters, as $\lambda(\kappa_A)$ increases with κ_A , $J_f^{(E)}$ appear abruptly and $J_r^{(E)}$ vanish simultaneously as κ_A exceeds $\kappa_A^{(C)}$ (Fig. 1E, see also Eqs. S34-S35, S41). Combining Eqs. S34-S36 and S43, we obtain:

$$\begin{cases} J_f^{(E)} = \varphi \cdot \lambda \cdot \theta(\lambda - \lambda_c), \\ J_r^{(E)} = \varphi \cdot \lambda \cdot [1 - \theta(\lambda - \lambda_c)], \end{cases} \quad (\text{S44})$$

where “ θ ” stands for the Heaviside step function. Defining $\lambda_{\max} = \lambda(\kappa_A^{\max})$, and then, $[0, \lambda_{\max}]$ is the relevant range of the x axis. In fact, the digital responses in Eq. S44 are consistent with the numerical simulation results of Molenaar *et al.* (Molenaar et al., 2009). However, these results are incompatible with the threshold-analog response in the standard picture of overflow metabolism (Basan et al., 2015; Holms, 1996).

In practice, the values of k_i^{cat} can be greatly influenced by the concentrations of potassium and phosphate (García-Contreras et al., 2012), which vary from cell to cell. Consequently, there is a distribution of values for k_i^{cat} among cell populations, commonly referred to as extrinsic noise (Elowitz et al., 2002). For convenience, we assume that each k_i^{cat} (and thus κ_i) follows a Gaussian distribution with a coefficient of variation (CV) of 25%. Therefore, the distributions of proteome efficiencies that determine the choice between respiration and fermentation, ε_r and ε_f , and the critical growth rate for the transition, λ_c , can be approximated by Gaussian distributions for a cell population (see Appendix 7.1 for details). Specifically, λ_c follows:

$$\lambda_c \sim \mathcal{N}(\mu_{\lambda_c}, \sigma_{\lambda_c}^2), \quad (\text{S45})$$

where μ_{λ_c} and σ_{λ_c} represent the mean and standard deviation of λ_c , with the CV $\sigma_{\lambda_c}/\mu_{\lambda_c}$ calculated to be 12% (see Appendix 8.2 for details). Note that λ is κ_A dependent, while λ_c is independent of κ_A . Thus, given the growth rate of microbes in a culturing medium (e.g., in a chemostat), the normalized energy fluxes are:

$$\begin{cases} J_f^{(\text{E})}(\lambda) = \frac{1}{2} \varphi \cdot \lambda \cdot \left[\text{erf} \left(\frac{\lambda - \mu_{\lambda_c}}{\sqrt{2} \sigma_{\lambda_c}} \right) + 1 \right], \\ J_r^{(\text{E})}(\lambda) = \frac{1}{2} \varphi \cdot \lambda \cdot \left[1 - \text{erf} \left(\frac{\lambda - \mu_{\lambda_c}}{\sqrt{2} \sigma_{\lambda_c}} \right) \right], \end{cases} \quad (\text{S46})$$

where “erf” represents the error function. In practice, given a culturing medium, there is also a probability distribution for the growth rate (Appendix-fig. 2B, see also Eq. S157). For approximation, in plotting the growth rate-respiration/fermentation flux relations, we use the deterministic (noise-free) value of the growth rate as a proxy. To compare with experiments, we essentially compare the normalized fluxes, $J_r^{(\text{N})}$ and $J_f^{(\text{N})}$ (see Appendix 8.1 for details). Combining Eqs. S30 and S46, we obtain:

$$\begin{cases} J_f^{(\text{N})}(\lambda) = \frac{\varphi}{\beta_f^{(A)}} \cdot \lambda \cdot \left[\text{erf} \left(\frac{\lambda - \mu_{\lambda_c}}{\sqrt{2} \sigma_{\lambda_c}} \right) + 1 \right], \\ J_r^{(\text{N})}(\lambda) = \frac{\varphi}{\beta_r^{(A)}} \cdot \lambda \cdot \left[1 - \text{erf} \left(\frac{\lambda - \mu_{\lambda_c}}{\sqrt{2} \sigma_{\lambda_c}} \right) \right]. \end{cases} \quad (\text{S47})$$

In Fig. 1C-D, we see that Eq. S47 quantitatively illustrates the experimental data (Basan et al., 2015), where the model parameters were obtained using biochemical data for the catalytic enzymes (see Appendix-table 1 for details).

Appendix 2.4 Dependence of the model on optimization principles

In the derivation of the growth rate dependence of respiration/fermentation flux described above (Eq. S44 for the single-cell level and Eq. S47 for the population-averaged level), we applied the principles of optimal growth, incorporating both efficient protein allocation to enzymes and ribosomes (through ribosomal proteins). However, recent experimental studies show that the inactive portion of ribosomes (i.e., ribosomes not bound to mRNAs) may vary with culturing conditions (Dai et al., 2017; Li et al., 2018) and between individual cells within the same culture (Pavlou et al., 2025), despite an overall trend toward growth optimization. These findings (Dai et al., 2017; Li et al., 2018; Pavlou et al., 2025) suggest that ribosome allocation may be suboptimal under many culturing conditions, likely as a result of cells preparing for potential environmental changes (Li et al., 2018). Nevertheless, since our model's predictions regarding the binary choice between respiration and fermentation rely solely on comparing proteome efficiency between these two pathways, which involves only efficient protein allocation to enzymes, and because the active portion of ribosomes and the translation elongation rate can be approximated as constants within the growth rate range of interest for cells exhibiting overflow metabolism (Dai et al., 2017), our model remains applicable to suboptimal growth conditions. This can be achieved by incorporating suboptimal ribosome allocation factors, lowering the parameter κ_r (which results in a larger ψ through Eq. S32), to account for these influences. For convenience, we present results for optimal growth below, while all model results can be extended to cases of suboptimal ribosome allocation.

Regarding the mechanism by which cells sense and choose between respiration and fermentation, although the standard picture of overflow metabolism (Basan et al., 2015; Holms, 1996) presents a growth rate dependence of fermentation flux, it is the proteome efficiency of respiration and fermentation, rather than the growth rate, that a cell should sense directly. Due to stochasticity in gene expression and metabolic reactions, the cell growth rate may fluctuate within a cell cycle (Kiviet et al., 2014; Pavlou et al., 2025), and suboptimal factors related to ribosome allocation (Dai et al., 2017; Li et al., 2018) would further complicate the scheme if cells were sensing via growth rate. Essentially, to expedite cell growth and survive under evolutionary pressure, cells should adopt the optimal strategy by directly sensing and comparing proteome efficiencies between respiration and fermentation, choosing the pathway with higher efficiency. This is analogous to how microbes choose between two types of carbon sources in a mixture for nutrient uptake (Wang et al., 2019). Mechanistically, the cyclic AMP (cAMP)-cAMP receptor protein (CRP) system plays an important role in sensing proteome efficiency and executing the optimal strategy between respiration and fermentation (Basan et al., 2015; Towbin et al., 2017; Valgepea et al., 2010; Wehrens et al., 2023). However, the roles of additional unidentified regulators are required to fully elucidate this mechanism (Basan et al., 2015; Valgepea et al., 2010).

Appendix 3 Model perturbations

Appendix 3.1 Overexpression of useless proteins

Here, we consider the case of overexpression of the protein encoded by the *lacZ* gene (i.e., ϕ_Z perturbation) in *E. coli*. Effectively, this limits the proteome by altering ϕ_{\max} :

$$\phi_{\max} \xrightarrow{\text{LacZ overexpression}} \phi_{\max} - \phi_Z, \quad (\text{S48})$$

where ϕ_Z stands for the proteomic mass fraction of useless proteins, which is controllable in experiments. Then, the growth rate changes into a bivariate function of κ_A and ϕ_Z :

$$\lambda(\kappa_A, \phi_Z) = \begin{cases} \frac{\phi_{\max} - \phi_Z}{\varphi/\varepsilon_r(\kappa_A) + \psi(\kappa_A)} & \varepsilon_r(\kappa_A) > \varepsilon_f(\kappa_A), \\ \frac{\phi_{\max} - \phi_Z}{\varphi/\varepsilon_f(\kappa_A) + \psi(\kappa_A)} & \varepsilon_r(\kappa_A) < \varepsilon_f(\kappa_A), \end{cases} \quad (\text{S49})$$

and thus,

$$\lambda(\kappa_A, \phi_Z) = \lambda(\kappa_A, 0)(1 - \phi_Z/\phi_{\max}). \quad (\text{S50})$$

Obviously, $\kappa_A^{(C)}$ remains a constant (following Eq. S42), while $\lambda_c(\phi_Z) \equiv \lambda(\kappa_A^{(C)}, \phi_Z)$ and $\lambda_{\max}(\phi_Z) \equiv \lambda(\kappa_A^{\max}, \phi_Z)$ become functions of ϕ_Z :

$$\begin{cases} \lambda_c(\phi_Z) = \lambda_c(0)(1 - \phi_Z/\phi_{\max}), \\ \lambda_{\max}(\phi_Z) = \lambda_{\max}(0)(1 - \phi_Z/\phi_{\max}). \end{cases} \quad (\text{S51})$$

In the homogeneous case, $J_f^{(E)}$ and $J_r^{(E)}$ follow:

$$\begin{cases} J_f^{(E)}(\kappa_A, \phi_Z) = \varphi \cdot \lambda(\kappa_A, \phi_Z) \cdot \theta(\lambda(\kappa_A, \phi_Z) - \lambda_c(\phi_Z)), \\ J_r^{(E)}(\kappa_A, \phi_Z) = \varphi \cdot \lambda(\kappa_A, \phi_Z) \cdot [1 - \theta(\lambda(\kappa_A, \phi_Z) - \lambda_c(\phi_Z))]. \end{cases} \quad (\text{S52})$$

Combined with Eqs. S50-S51, we have:

$$\begin{cases} J_f^{(E)}(\kappa_A, \phi_Z) = \varphi \cdot \lambda(\kappa_A, \phi_Z) \cdot \theta(\lambda(\kappa_A, 0) - \lambda_c(0)), \\ J_r^{(E)}(\kappa_A, \phi_Z) = \varphi \cdot \lambda(\kappa_A, \phi_Z) \cdot [1 - \theta(\lambda(\kappa_A, 0) - \lambda_c(0))]. \end{cases} \quad (\text{S53})$$

To compare with experiments, we assume that each k_i^{cat} and κ_i follow the extrinsic noise with a CV of 25% specified in Appendix 2.3, and we neglect the noise on ϕ_Z and ϕ_{\max} . Combining Eqs. S45 and S51, $\lambda_c(\phi_Z)$ approximately follows a Gaussian distribution:

$$\lambda_c(\phi_Z) \sim \mathcal{N}\left(\mu_{\lambda_c}(\phi_Z), \sigma_{\lambda_c}(\phi_Z)^2\right), \quad (\text{S54})$$

where $\mu_{\lambda_c}(\phi_Z)$ and $\sigma_{\lambda_c}(\phi_Z)$ represent the mean and standard deviation of $\lambda_c(\phi_Z)$, with

$$\begin{cases} \mu_{\lambda_c}(\phi_Z) = \mu_{\lambda_c}(0)(1 - \phi_Z/\phi_{\max}), \\ \sigma_{\lambda_c}(\phi_Z) = \sigma_{\lambda_c}(0)(1 - \phi_Z/\phi_{\max}). \end{cases} \quad (\text{S55})$$

Here, $\mu_{\lambda_c}(0)$, $\sigma_{\lambda_c}(0)$, $\lambda_c(0)$, $\lambda_{\max}(0)$ and $\lambda(\kappa_A, 0)$ represent the parameters or variables free from ϕ_Z perturbation, just as those in Appendix 2.3. Since the noise on the multiplier term (i.e., $1 - \phi_Z/\phi_{\max}$) is negligible, the CV of $\lambda_c(\phi_Z)$ (i.e., $\sigma_{\lambda_c}(\phi_Z)/\mu_{\lambda_c}(\phi_Z)$) is unaffected by ϕ_Z . By combining Eqs. S46 and S48, we obtain the relations between the normalized energy fluxes and growth rate:

$$\begin{cases} J_f^{(E)}(\lambda(\kappa_A, \phi_Z), \phi_Z) = \frac{1}{2} \varphi \cdot \lambda(\kappa_A, \phi_Z) \cdot \left[\operatorname{erf}\left(\frac{\lambda(\kappa_A, \phi_Z) - \mu_{\lambda_c}(\phi_Z)}{\sqrt{2}\sigma_{\lambda_c}(\phi_Z)}\right) + 1 \right], \\ J_r^{(E)}(\lambda(\kappa_A, \phi_Z), \phi_Z) = \frac{1}{2} \varphi \cdot \lambda(\kappa_A, \phi_Z) \cdot \left[1 - \operatorname{erf}\left(\frac{\lambda(\kappa_A, \phi_Z) - \mu_{\lambda_c}(\phi_Z)}{\sqrt{2}\sigma_{\lambda_c}(\phi_Z)}\right) \right], \end{cases} \quad (\text{S56})$$

where $\lambda(\kappa_A, \phi_Z)$, $\mu_{\lambda_c}(\phi_Z)$ and $\sigma_{\lambda_c}(\phi_Z)$ follow Eqs. S50 and S55 accordingly. For a given value of ϕ_Z , i.e., ϕ_Z is fixed, then, $\lambda(\kappa_A, \phi_Z)$ changes monotonically with κ_A . Combining Eqs. S55-S56 and S30, we obtain the relation between the normalized fluxes $J_r^{(N)}$, $J_f^{(N)}$ and the growth rate (where ϕ_Z is a parameter):

$$\begin{cases} J_f^{(N)}(\lambda, \phi_Z) = \frac{\varphi}{\beta_f^{(A)}} \cdot \lambda \cdot \left[\operatorname{erf}\left(\frac{\lambda - \mu_{\lambda_c}(0)(1 - \phi_Z/\phi_{\max})}{\sqrt{2}\sigma_{\lambda_c}(0)(1 - \phi_Z/\phi_{\max})}\right) + 1 \right], \\ J_r^{(N)}(\lambda, \phi_Z) = \frac{\varphi}{\beta_r^{(A)}} \cdot \lambda \cdot \left[1 - \operatorname{erf}\left(\frac{\lambda - \mu_{\lambda_c}(0)(1 - \phi_Z/\phi_{\max})}{\sqrt{2}\sigma_{\lambda_c}(0)(1 - \phi_Z/\phi_{\max})}\right) \right]. \end{cases} \quad (\text{S57})$$

In Fig. 2C. we show that the model predictions (Eq. S57) quantitatively agree with the experiments (Basan et al., 2015).

Meanwhile, we can also perturb the growth rate by tuning ϕ_Z in a stable culturing environment with fixed concentration of a Group A carbon source (i.e., given $[A]$). In fact, for this case there is a distribution of κ_A values due to the extrinsic noise in k_A^{cat} , yet this distribution is fixed. For convenience of description, we still referred to it as fixed κ_A . Then, combining Eqs. S30, S50, S55 and S56, we get:

$$\begin{cases} J_f^{(N)}(\lambda, \phi_Z) = \frac{\varphi}{\beta_f^{(A)}} \cdot \left[\operatorname{erf} \left(\frac{\lambda(\kappa_A, 0) - \mu_{\lambda_c}(0)}{\sqrt{2}\sigma_{\lambda_c}(0)} \right) + 1 \right] \cdot \lambda, \\ J_r^{(N)}(\lambda, \phi_Z) = \frac{\varphi}{\beta_r^{(A)}} \cdot \left[1 - \operatorname{erf} \left(\frac{\lambda(\kappa_A, 0) - \mu_{\lambda_c}(0)}{\sqrt{2}\sigma_{\lambda_c}(0)} \right) \right] \cdot \lambda. \end{cases} \quad (\text{S58})$$

Here, $\lambda(\kappa_A, 0)$ remains unaltered as κ_A is fixed. Therefore, in this case, $J_f^{(N)}$ and $J_r^{(N)}$ are proportional to λ , where the slopes are both functions of κ_A . More specifically, the slope of $J_f^{(N)}$ is a monotonically increasing function of κ_A , while that of $J_r^{(N)}$ is a monotonically decreasing function of κ_A . In Fig. 2B, we see that the model predictions (Eq. S58) agree quantitatively with the experiments (Basan et al., 2015).

In fact, the growth rate can be altered by tuning ϕ_Z and κ_A simultaneously. Then, the relations among the energy fluxes, growth rate and ϕ_Z still follow Eq. S57 (where ϕ_Z is a variable). In a 3-D representation, these relations correspond to a surface. In Fig. 2A, we show that the model predictions (Eq. S57) match well with the experimental data (Basan et al., 2015).

Appendix 3.2 Energy dissipation

In practice, energy dissipation disrupts the proportional relationship between energy demand and biomass production. Thus, Eq. S25 becomes:

$$J_E = r_E \cdot J_{\text{BM}} + w \cdot \frac{M_{\text{carbon}}}{m_0}, \quad (\text{S59})$$

where w represents the dissipation coefficient. In fact, maintenance energy contributes to energy dissipation, and we define the maintenance energy coefficient as w_0 . In bacteria, the impact of maintenance energy is roughly negligible, yet in tumor cells, it plays a much more significant role (Locasale and Cantley, 2010).

The introduction of energy dissipation leads to a modification of Eq. S26: combining Eq. S59 and Eq. S16, we have:

$$J_E^{(N)} = \eta_E \cdot \lambda + w. \quad (\text{S60})$$

Then, Eq. S29 changes to:

$$\begin{cases} J_r^{(E)} + J_f^{(E)} = \varphi \cdot \lambda + w, \\ \frac{J_r^{(E)}}{\varepsilon_r} + \frac{J_f^{(E)}}{\varepsilon_f} = \phi_{\text{max}} - \psi \cdot \lambda. \end{cases} \quad (\text{S61})$$

Consequently, if $\varepsilon_r > \varepsilon_f$, the optimal growth strategy for the cell is:

$$\begin{cases} J_f^{(E)} = 0, \\ J_r^{(E)} = \varphi \cdot \lambda + w, \end{cases} \quad \varepsilon_r > \varepsilon_f, \quad (\text{S62})$$

and if $\varepsilon_f > \varepsilon_r$, the optimal growth strategy is:

$$\begin{cases} J_f^{(E)} = \varphi \cdot \lambda + w, \\ J_r^{(E)} = 0. \end{cases} \quad \varepsilon_r < \varepsilon_f. \quad (\text{S63})$$

Then, the growth rate becomes a bivariate function of both κ_A and w :

$$\lambda(\kappa_A, w) = \begin{cases} \frac{\phi_{\max} - w/\varepsilon_r(\kappa_A)}{\varphi/\varepsilon_r(\kappa_A) + \psi(\kappa_A)} & \varepsilon_r(\kappa_A) > \varepsilon_f(\kappa_A), \\ \frac{\phi_{\max} - w/\varepsilon_f(\kappa_A)}{\varphi/\varepsilon_f(\kappa_A) + \psi(\kappa_A)} & \varepsilon_r(\kappa_A) < \varepsilon_f(\kappa_A). \end{cases} \quad (\text{S64})$$

Clearly, $\kappa_A^{(C)}$ is still a constant, while $\lambda_c(w) \equiv \lambda(\kappa_A^{(C)}, w)$ and $\lambda_{\max}(w) \equiv \lambda(\kappa_A^{\max}, w)$ become functions of w :

$$\begin{cases} \lambda_c(w) = \lambda_c(0) \left\{ 1 - w / \left[\varepsilon_{r/f}(\kappa_A^{(C)}) \phi_{\max} \right] \right\}, \\ \lambda_{\max}(w) = \lambda_{\max}(0) \left\{ 1 - w / \left[\varepsilon_f(\kappa_A^{\max}) \phi_{\max} \right] \right\}. \end{cases} \quad (\text{S65})$$

For a cell population, in the homogeneous case, $J_f^{(E)}$ and $J_r^{(E)}$ follow:

$$\begin{cases} J_f^{(E)}(\kappa_A, w) = [\varphi \cdot \lambda(\kappa_A, w) + w] \cdot \theta(\lambda(\kappa_A, w) - \lambda_c(w)), \\ J_r^{(E)}(\kappa_A, w) = [\varphi \cdot \lambda(\kappa_A, w) + w] \cdot [1 - \theta(\lambda(\kappa_A, w) - \lambda_c(w))]. \end{cases} \quad (\text{S66})$$

To compare with experiments, we assume the same extent of extrinsic noise in k_i^{cat} (and thus κ_i) as that specified in Appendix 2.3. Combining Eqs. S45 and S65, $\lambda_c(w)$ approximately follows a Gaussian distribution:

$$\lambda_c(w) \sim \mathcal{N}(\mu_{\lambda_c}(w), \sigma_{\lambda_c}(w)^2), \quad (\text{S67})$$

where $\mu_{\lambda_c}(w)$ and $\sigma_{\lambda_c}(w)$ represent the mean and standard deviation of $\lambda_c(w)$, and

$$\begin{cases} \mu_{\lambda_c}(w) = \mu_{\lambda_c}(0) \left\{ 1 - w / \left[\varepsilon_{r/f}(\kappa_A^{(C)}) \phi_{\max} \right] \right\}, \\ \sigma_{\lambda_c}(w) \approx \sigma_{\lambda_c}(0) \left\{ 1 - w / \left[\varepsilon_{r/f}(\kappa_A^{(C)}) \phi_{\max} \right] \right\}. \end{cases} \quad (\text{S68})$$

Here, $\mu_{\lambda_c}(0)$, $\sigma_{\lambda_c}(0)$, $\lambda_c(0)$, $\lambda_{\max}(0)$ and $\lambda(\kappa_A, 0)$ represent parameters or variables unaffected by energy dissipation. In fact, there is a distribution of values for $\varepsilon_{r/f}(\kappa_A^{(C)})$. For approximation, we use the deterministic value of $\varepsilon_{r/f}(\kappa_A^{(C)})$ in Eq. S68, and then the CV of $\lambda_c(w)$ remains largely unperturbed by w . Combining Eqs. S46, S66 and S67, we have:

$$\begin{cases} J_f^{(E)}(\lambda(\kappa_A, w), w) = \frac{1}{2}(\varphi \cdot \lambda(\kappa_A, w) + w) \cdot \left[\operatorname{erf} \left(\frac{\lambda(\kappa_A, w) - \mu_{\lambda_c}(w)}{\sqrt{2}\sigma_{\lambda_c}(w)} \right) + 1 \right], \\ J_r^{(E)}(\lambda(\kappa_A, w), w) = \frac{1}{2}(\varphi \cdot \lambda(\kappa_A, w) + w) \cdot \left[1 - \operatorname{erf} \left(\frac{\lambda(\kappa_A, w) - \mu_{\lambda_c}(w)}{\sqrt{2}\sigma_{\lambda_c}(w)} \right) \right]. \end{cases} \quad (\text{S69})$$

Since the dissipation coefficient w is tunable in experiments, for a given value of w , $\lambda(\kappa_A, w)$ changes monotonically with κ_A . Combining Eqs. S68-S69 and S30, we have (here w is a parameter):

$$\begin{cases} J_f^{(N)}(\lambda, w) = \frac{\varphi \cdot \lambda + w}{\beta_f^{(A)}} \cdot \left[\operatorname{erf} \left(\frac{\lambda - \mu_{\lambda_c}(0) \left\{ 1 - w / \left[\varepsilon_{r/f}(\kappa_A^{(C)}) \phi_{\max} \right] \right\}}{\sqrt{2}\sigma_{\lambda_c}(0) \left\{ 1 - w / \left[\varepsilon_{r/f}(\kappa_A^{(C)}) \phi_{\max} \right] \right\}} \right) + 1 \right], \\ J_r^{(N)}(\lambda, w) = \frac{\varphi \cdot \lambda + w}{\beta_r^{(A)}} \cdot \left[1 - \operatorname{erf} \left(\frac{\lambda - \mu_{\lambda_c}(0) \left\{ 1 - w / \left[\varepsilon_{r/f}(\kappa_A^{(C)}) \phi_{\max} \right] \right\}}{\sqrt{2}\sigma_{\lambda_c}(0) \left\{ 1 - w / \left[\varepsilon_{r/f}(\kappa_A^{(C)}) \phi_{\max} \right] \right\}} \right) \right]. \end{cases} \quad (\text{S70})$$

The comparison between model predictions (Eq. S70) and experimental results (Basan et al., 2015) is shown in Fig. 3B, which shows quantitative agreement. Meanwhile, the growth rate can also be perturbed by changing κ_A and w simultaneously. The relations among the energy fluxes, growth rate and w follow Eq. S70 (here w is a variable). In a 3D representation, these relations form a surface. As shown in Fig. 3A, the model predictions (Eq. S70) agree quantitatively with the experimental results (Basan et al., 2015).

Appendix 3.3 Translation inhibition

In *E. coli*, the translation rate can be modified by adding different concentrations of translation inhibitors, e.g., chloramphenicol (Cm). The net effect of this perturbation is represented as:

$$\kappa_i \xrightarrow{\text{Translation inhibition}} \kappa_i / (\iota + 1), \quad (\text{S71})$$

where ι stands for the inhibition coefficient with $\iota > 0$, and $(1 + \iota)^{-1}$ represents the translation efficiency. Thus, Eq. S32 changes to:

$$\psi(\kappa_A, \iota) = \frac{\iota + 1}{\kappa_i} + \frac{1 + \eta_{a1} + \eta_c}{2\kappa_A} + \frac{\eta_{a2} + \eta_b + 2\eta_c + \eta_d}{2\kappa_1} + \frac{\eta_b + \eta_c}{\kappa_2} + \frac{\eta_c}{\kappa_3} + \frac{\eta_c + \eta_d}{\kappa_5} + \sum_i^{a1, a2, b, c, d} \frac{\eta_i}{\kappa_i}. \quad (\text{S72})$$

First, we consider the case where maintenance energy is neglected, i.e., $w_0 = 0$. In this case, the growth rate takes the following form:

$$\lambda(\kappa_A, \iota) = \begin{cases} \frac{\phi_{\max}}{\varphi / \varepsilon_r(\kappa_A) + \psi(\kappa_A, \iota)} & \varepsilon_r(\kappa_A) > \varepsilon_f(\kappa_A), \\ \frac{\phi_{\max}}{\varphi / \varepsilon_f(\kappa_A) + \psi(\kappa_A, \iota)} & \varepsilon_r(\kappa_A) < \varepsilon_f(\kappa_A), \end{cases} \quad (\text{S73})$$

where $\lambda(\kappa_A, 0)$ and $\psi(\kappa_A, 0)$ represent the terms unaffected by translation inhibition. Thus, $\lambda_c(\iota) \equiv \lambda(\kappa_A^{(C)}, \iota)$ and $\lambda_{\max}(\iota) \equiv \lambda(\kappa_A^{\max}, \iota)$ become functions of ι :

$$\begin{cases} \lambda_c(\iota) = \lambda_c(0) \frac{\varphi / \varepsilon_{r/f}(\kappa_A^{(C)}) + \psi(\kappa_A^{(C)}, 0)}{\varphi / \varepsilon_{r/f}(\kappa_A^{(C)}) + \psi(\kappa_A^{(C)}, \iota)}, \\ \lambda_{\max}(\iota) = \lambda_{\max}(0) \frac{\varphi / \varepsilon_f(\kappa_A^{\max}) + \psi(\kappa_A^{\max}, 0)}{\varphi / \varepsilon_f(\kappa_A^{\max}) + \psi(\kappa_A^{\max}, \iota)}. \end{cases} \quad (\text{S74})$$

In the homogeneous case, $J_f^{(E)}$ and $J_r^{(E)}$ follow:

$$\begin{cases} J_f^{(E)}(\kappa_A, \iota) = \varphi \cdot \lambda(\kappa_A, \iota) \cdot \theta(\lambda(\kappa_A, \iota) - \lambda_c(\iota)), \\ J_r^{(E)}(\kappa_A, \iota) = \varphi \cdot \lambda(\kappa_A, \iota) \cdot [1 - \theta(\lambda(\kappa_A, \iota) - \lambda_c(\iota))]. \end{cases} \quad (\text{S75})$$

To compare with experiments, we assume that extrinsic noise exists in k_i^{cat} and κ_i as specified in Appendix 2.3. Combining Eqs. S45 and S74, $\lambda_c(\iota)$ can be approximated by a Gaussian distribution:

$$\lambda_c(\iota) \sim \mathcal{N}(\mu_{\lambda_c}(\iota), \sigma_{\lambda_c}(\iota)^2), \quad (\text{S76})$$

where $\mu_{\lambda_c}(\iota)$ and $\sigma_{\lambda_c}(\iota)$ represent the mean and standard deviation of $\lambda_c(\iota)$, with

$$\begin{cases} \mu_{\lambda_c}(t) = \mu_{\lambda_c}(0) \frac{\varphi/\varepsilon_{r/f}(\kappa_A^{(c)}) + \psi(\kappa_A^{(c)}, 0)}{\varphi/\varepsilon_{r/f}(\kappa_A^{(c)}) + \psi(\kappa_A^{(c)}, t)}, \\ \sigma_{\lambda_c}(t) \approx \sigma_{\lambda_c}(0) \frac{\varphi/\varepsilon_{r/f}(\kappa_A^{(c)}) + \psi(\kappa_A^{(c)}, 0)}{\varphi/\varepsilon_{r/f}(\kappa_A^{(c)}) + \psi(\kappa_A^{(c)}, t)}. \end{cases} \quad (\text{S77})$$

Here, $\mu_{\lambda_c}(0)$, $\sigma_{\lambda_c}(0)$, $\psi(\kappa_A^{(c)}, 0)$, $\lambda_c(0)$ and $\lambda_{\max}(0)$ stand for the terms unaffected by translation inhibition. Essentially, there are distributions of values for $\varepsilon_{r/f}(\kappa_A^{(c)})$, $\psi(\kappa_A^{(c)}, 0)$ and $\psi(\kappa_A^{(c)}, t)$. For approximation, we use the deterministic values of these terms in Eq. S77, and then the CV of $\lambda_c(t)$ can be approximated by $\lambda_c(0)$. Combining Eqs. S46, S75 and S76, we have:

$$\begin{cases} J_f^{(E)}(\lambda(\kappa_A, t), t) = \frac{1}{2} \varphi \cdot \lambda(\kappa_A, t) \cdot \left[\operatorname{erf}\left(\frac{\lambda(\kappa_A, t) - \mu_{\lambda_c}(t)}{\sqrt{2}\sigma_{\lambda_c}(t)}\right) + 1 \right], \\ J_r^{(E)}(\lambda(\kappa_A, t), t) = \frac{1}{2} \varphi \cdot \lambda(\kappa_A, t) \cdot \left[1 - \operatorname{erf}\left(\frac{\lambda(\kappa_A, t) - \mu_{\lambda_c}(t)}{\sqrt{2}\sigma_{\lambda_c}(t)}\right) \right]. \end{cases} \quad (\text{S78})$$

In the experiments, the inhibition coefficient t is controllable by adjusting the concentration of the translation inhibitor. For a given value of t , $\lambda(\kappa_A, t)$ changes monotonically with κ_A . Combining Eqs. S30 and S78, we have (here t is a parameter):

$$\begin{cases} J_f^{(N)}(\lambda, t) = \frac{\varphi \cdot \lambda}{\beta_f^{(A)}} \cdot \left[\operatorname{erf}\left(\frac{\lambda - \mu_{\lambda_c}(t)}{\sqrt{2}\sigma_{\lambda_c}(t)}\right) + 1 \right], \\ J_r^{(N)}(\lambda, t) = \frac{\varphi \cdot \lambda}{\beta_r^{(A)}} \cdot \left[1 - \operatorname{erf}\left(\frac{\lambda - \mu_{\lambda_c}(t)}{\sqrt{2}\sigma_{\lambda_c}(t)}\right) \right], \end{cases} \quad (\text{S79})$$

where $\mu_{\lambda_c}(t)$ and $\sigma_{\lambda_c}(t)$ follow Eq. S77. The growth rate can also be perturbed by altering both κ_A and t simultaneously. In this case, the relations among the energy fluxes, growth rate and t still follow Eq. S79 (here t is a variable). The comparison between Eq. S79 and experimental data (Basan et al., 2015) is shown in Appendix-fig. 2D (3-D) and 2E (2-D). Overall, there is good consistency; however, there remains a noticeable discrepancy when t is large (i.e., at high concentration of the translation inhibitor). This led us to consider the maintenance energy through the coefficient w_0 , which is small but may account for this discrepancy. Then, $\lambda(\kappa_A, t)$ changes into:

$$\lambda(\kappa_A, t) = \begin{cases} \frac{\phi_{\max} - w_0/\varepsilon_r(\kappa_A)}{\varphi/\varepsilon_r(\kappa_A) + \psi(\kappa_A, t)} & \varepsilon_r(\kappa_A) > \varepsilon_f(\kappa_A), \\ \frac{\phi_{\max} - w_0/\varepsilon_f(\kappa_A)}{\varphi/\varepsilon_f(\kappa_A) + \psi(\kappa_A, t)} & \varepsilon_r(\kappa_A) < \varepsilon_f(\kappa_A), \end{cases} \quad (\text{S80})$$

while $\lambda_c(t) \equiv \lambda(\kappa_A^{(C)}, t)$ and $\lambda_{\max}(t) \equiv \lambda(\kappa_A^{\max}, t)$ still follow Eq. S74, though the forms of $\lambda_c(0)$ and $\lambda_{\max}(0)$ change to:

$$\begin{cases} \lambda_c(0) = \frac{\phi_{\max} - w_0/\varepsilon_{r/f}(\kappa_A^{(C)})}{\varphi/\varepsilon_{r/f}(\kappa_A^{(C)}) + \psi(\kappa_A^{(C)}, 0)}, \\ \lambda_{\max}(0) = \frac{\phi_{\max} - w_0/\varepsilon_f(\kappa_A^{\max})}{\varphi/\varepsilon_f(\kappa_A^{\max}) + \psi(\kappa_A^{\max}, 0)}. \end{cases} \quad (\text{S81})$$

In the homogeneous case, $J_f^{(E)}$ and $J_r^{(E)}$ follow:

$$\begin{cases} J_f^{(E)}(\kappa_A, t) = [\varphi \cdot \lambda(\kappa_A, t) + w_0] \cdot \theta(\lambda(\kappa_A, t) - \lambda_c(t)), \\ J_r^{(E)}(\kappa_A, t) = [\varphi \cdot \lambda(\kappa_A, t) + w_0] \cdot [1 - \theta(\lambda(\kappa_A, t) - \lambda_c(t))]. \end{cases} \quad (\text{S82})$$

To compare with experiments, we assume that the extrinsic noise follows the specification in Appendix 2.3. Combining Eqs. S45, S74 and S81, $\lambda_c(t)$ approximately follows a Gaussian distribution:

$$\lambda_c(t) \sim \mathcal{N}(\mu_{\lambda_c}(t), \sigma_{\lambda_c}(t)^2). \quad (\text{S83})$$

Here $\mu_{\lambda_c}(t)$ and $\sigma_{\lambda_c}(t)$ still follow Eq. S77, while $\mu_{\lambda_c}(0)$ and $\sigma_{\lambda_c}(0)$ change accordingly with $\lambda_c(0)$ (see Eq. S81). For approximation, we use the deterministic values of the relevant terms in Eq. S77, and then the CV of $\lambda_c(t)$ is roughly the same as $\lambda_c(0)$. Combining Eqs. S46, S82 and S83, we have:

$$\begin{cases} J_f^{(E)}(\lambda(\kappa_A, t), t) = \frac{1}{2}(\varphi \cdot \lambda(\kappa_A, t) + w_0) \cdot \left[\operatorname{erf}\left(\frac{\lambda(\kappa_A, t) - \mu_{\lambda_c}(t)}{\sqrt{2}\sigma_{\lambda_c}(t)}\right) + 1 \right], \\ J_r^{(E)}(\lambda(\kappa_A, t), t) = \frac{1}{2}(\varphi \cdot \lambda(\kappa_A, t) + w_0) \cdot \left[1 - \operatorname{erf}\left(\frac{\lambda(\kappa_A, t) - \mu_{\lambda_c}(t)}{\sqrt{2}\sigma_{\lambda_c}(t)}\right) \right]. \end{cases} \quad (\text{S84})$$

Thus, for a given t , $\lambda(\kappa_A, t)$ changes monotonically with κ_A . Combining Eqs. S30 and S84, we have (here t is a parameter):

$$\begin{cases} J_f^{(N)}(\lambda, \iota) = \frac{\varphi \cdot \lambda + w_0}{\beta_f^{(A)}} \cdot \left[\operatorname{erf} \left(\frac{\lambda - \mu_{\lambda_c}(\iota)}{\sqrt{2}\sigma_{\lambda_c}(\iota)} \right) + 1 \right] \\ J_r^{(N)}(\lambda, \iota) = \frac{\varphi \cdot \lambda + w_0}{\beta_r^{(A)}} \cdot \left[1 - \operatorname{erf} \left(\frac{\lambda - \mu_{\lambda_c}(\iota)}{\sqrt{2}\sigma_{\lambda_c}(\iota)} \right) \right] \end{cases} \quad (\text{S85})$$

The growth rate and fluxes can also be perturbed by altering both κ_A and ι simultaneously. The relations among the energy fluxes, growth rate and ι would still follow Eq. S85, except that ι is now regarded as a variable. Assuming a small amount of maintenance energy by assigning $w_0 = 2.5 \text{ (} h^{-1} \text{)}$, we find that the experimental results (Basan et al., 2015) agree quantitatively well with the model predictions (Fig. 3C-D).

Appendix 4 Overflow metabolism in substrates other than Group A carbon sources

Due to the topology of the metabolic network, for cells using Group A carbon sources, the behavior of overflow metabolism follows Eq. 5 (or Eq. S47) upon κ_A perturbation (i.e., varying the type or concentration of a Group A carbon source). This has been demonstrated clearly in the above analysis and agrees quantitatively with experiments. However, further analysis is required for cells using substrates other than Group A sources due to the topological differences in carbon utilization (Wang et al., 2019). In principle, substrates entering from glycolysis or the points before acetyl-CoA are potentially involved in overflow metabolism, while those joining from the TCA cycle are not relevant to this behavior. Still, mixed carbon sources are likely to induce a different profile of overflow metabolism, as long as there is a carbon source derived from glycolysis.

Appendix 4.1 Pyruvate

The coarse-grained model for pyruvate utilization is shown in Fig. 3E. Here, nodes M_1, M_2, M_3, M_4, M_5 follow the descriptions in Appendix 2.1. Each biochemical reaction follows Eq. S5 with $b_i = 1$ except that $2M_2 \rightarrow M_1$ and $M_3 + M_5 \rightarrow M_4$. By applying flux balance to the stoichiometric fluxes, combining with Eq. S8, we have:

$$\begin{cases} \Phi_{\text{py}} \cdot \xi_{\text{py}} = \Phi_7 \cdot \xi_7 + \Phi_8 \cdot \xi_8, \\ \Phi_7 \cdot \xi_7 = 2\Phi_9 \cdot \xi_9 + \Phi_5 \cdot \xi_5 + \Phi_{a2} \cdot \xi_{a2}, \\ \Phi_9 \cdot \xi_9 = \Phi_{a1} \cdot \xi_{a1}, \\ \Phi_8 \cdot \xi_8 = \Phi_3 \cdot \xi_3 + \Phi_6 \cdot \xi_6 + \Phi_b \cdot \xi_b, \\ \Phi_5 \cdot \xi_5 + \Phi_4 \cdot \xi_4 = \Phi_3 \cdot \xi_3 + \Phi_d \cdot \xi_d, \\ \Phi_3 \cdot \xi_3 = \Phi_4 \cdot \xi_4 + \Phi_c \cdot \xi_c. \end{cases} \quad (\text{S86})$$

For energy biogenesis, we convert all the energy currencies into ATPs, and then,

$$\beta_8 \cdot \Phi_8 \cdot \xi_8 + \beta_3 \cdot \Phi_3 \cdot \xi_3 + \beta_4 \cdot \Phi_4 \cdot \xi_4 + \beta_6 \cdot \Phi_6 \cdot \xi_6 + \beta_{a1} \cdot \Phi_{a1} \cdot \xi_{a1} - \beta_7 \cdot \Phi_7 \cdot \xi_7 - \beta_9 \cdot \Phi_9 \cdot \xi_9 = J_E, \quad (\text{S87})$$

where $\beta_7 = 1$, $\beta_8 = 2$, $\beta_3 = 2$, $\beta_4 = 6$, $\beta_6 = 1$, $\beta_9 = 6$, $\beta_{a1} = 4$ for *E. coli* (Neidhardt et al., 1990; Sauer et al., 2004), and J_E follows Eq. S25. By applying the substitutions specified in Eqs. S9, S12, S14-S18, combined with Eqs. S4, S10, S22, S23, S25, S86-S87, and the constraint of proteome resource allocation, we have:

$$\left\{ \begin{array}{l} \phi_{\text{py}} \cdot \kappa_{\text{py}} = \phi_7 \cdot \kappa_7 + \phi_8 \cdot \kappa_8, \\ \phi_7 \cdot \kappa_7 = 2\phi_9 \cdot \kappa_9 + \phi_5 \cdot \kappa_5 + \phi_{a2} \cdot \kappa_{a2}, \\ \phi_9 \cdot \kappa_9 = \phi_{a1} \cdot \kappa_{a1} \\ \phi_8 \cdot \kappa_8 = \phi_3 \cdot \kappa_3 + \phi_6 \cdot \kappa_6 + \phi_b \cdot \kappa_b \\ \phi_3 \cdot \kappa_3 = \phi_4 \cdot \kappa_4 + \phi_c \cdot \kappa_c \\ \phi_5 \cdot \kappa_5 + \phi_4 \cdot \kappa_4 = \phi_3 \cdot \kappa_3 + \phi_d \cdot \kappa_d \\ \phi_{a1} \cdot \kappa_{a1} = \eta_{a1} \cdot \lambda, \phi_{a2} \cdot \kappa_{a2} = \eta_{a2} \cdot \lambda, \phi_b \cdot \kappa_b = \eta_b \cdot \lambda, \phi_c \cdot \kappa_c = \eta_c \cdot \lambda, \phi_d \cdot \kappa_d = \eta_d \cdot \lambda, \\ \beta_8 \cdot \phi_8 \cdot \kappa_8 + \beta_3 \cdot \phi_3 \cdot \kappa_3 + \beta_4 \cdot \phi_4 \cdot \kappa_4 + \beta_6 \cdot \phi_6 \cdot \kappa_6 + \beta_{a1} \cdot \phi_{a1} \cdot \kappa_{a1} - \beta_7 \cdot \phi_7 \cdot \kappa_7 - \beta_9 \cdot \phi_9 \cdot \kappa_9 = J_E^{(N)}, \\ J_E^{(N)} = \eta_E \cdot \lambda, \lambda = \phi_R \cdot \kappa_r, J_r^{(N)} = \phi_4 \cdot \kappa_4, J_f^{(N)} = \phi_6 \cdot \kappa_6, \\ \phi_R + \phi_{\text{py}} + \phi_3 + \phi_4 + \phi_5 + \phi_6 + \phi_7 + \phi_8 + \phi_9 + \phi_{a1} + \phi_{a2} + \phi_b + \phi_c + \phi_d = \phi_{\text{max}}, \end{array} \right. \quad (\text{S88})$$

where $\eta_E = r_E \cdot \left[\sum_i r_i / N_{\text{EP}_i}^{\text{carbon}} \right]^{-1}$. κ_i is approximately a constant which follows Eq. S20 for each of the intermediate node. The substrate quality of κ_{py} varies with the external concentration of pyruvate ([py]),

$$\kappa_{\text{py}} \equiv \frac{r_{\text{protein}}}{r_{\text{carbon}}} \cdot \frac{k_{\text{py}}^{\text{cat}}}{m_{E_{\text{py}}}} \cdot \frac{[\text{py}]}{[\text{py}] + K_{\text{py}}} \cdot m_0. \quad (\text{S89})$$

From Eq. S88, all ϕ_i can be expressed by $J_r^{(N)}$, $J_f^{(N)}$, and λ :

$$\left\{ \begin{array}{l} \phi_{\text{py}} = \left[(2\eta_{a1} + \eta_{a2} + \eta_b + 2\eta_c + \eta_d) \lambda + J_r^{(N)} + J_f^{(N)} \right] / \kappa_{\text{py}}, \\ \phi_7 = (2\eta_{a1} + \eta_{a2} + \eta_c + \eta_d) \lambda / \kappa_7, \phi_9 = \eta_{a1} \cdot \lambda / \kappa_9 \\ \phi_8 = \left[J_r^{(N)} + J_f^{(N)} + (\eta_b + \eta_c) \lambda \right] / \kappa_8 \\ \phi_3 = (J_r^{(N)} + \eta_c \cdot \lambda) / \kappa_3, \phi_4 = J_r^{(N)} / \kappa_4, \\ \phi_5 = (\eta_c + \eta_d) \lambda / \kappa_5, \phi_6 = J_f^{(N)} / \kappa_6, \\ \phi_i = \eta_i \cdot \lambda / \kappa_i \quad (i = a1, a2, b, c, d). \end{array} \right. \quad (\text{S90})$$

By substituting Eq. S90 into Eq. S88, we have:

$$\begin{cases} J_r^{(E,py)} + J_f^{(E,py)} = \varphi_{py} \cdot \lambda, \\ \frac{J_r^{(E,py)}}{\varepsilon_r^{(py)}} + \frac{J_f^{(E,py)}}{\varepsilon_f^{(py)}} = \phi_{\max} - \psi_{py} \cdot \lambda. \end{cases} \quad (S91)$$

Here, $J_r^{(E,py)}$ and $J_f^{(E,py)}$ stand for the normalized energy fluxes of respiration and fermentation, respectively, with

$$\begin{cases} J_r^{(E,py)} = \beta_r^{(py)} \cdot J_r^{(N)}, \\ J_f^{(E,py)} = \beta_f^{(py)} \cdot J_f^{(N)}. \end{cases} \quad (S92)$$

where $\beta_r^{(py)} = \beta_3 + \beta_4 + \beta_8$ and $\beta_f^{(py)} = \beta_6 + \beta_8$, with $\beta_r^{(py)} = 10$ and $\beta_f^{(py)} = 3$ for *E. coli*. The coefficients $\varepsilon_r^{(py)}$ and $\varepsilon_f^{(py)}$ represent the proteome efficiencies for energy biogenesis using pyruvate in respiration and fermentation pathways, respectively, with

$$\begin{cases} \varepsilon_r^{(py)} = \frac{\beta_r^{(py)}}{1/\kappa_{py} + 1/\kappa_8 + 1/\kappa_3 + 1/\kappa_4}, \\ \varepsilon_f^{(py)} = \frac{\beta_f^{(py)}}{1/\kappa_{py} + 1/\kappa_8 + 1/\kappa_6}. \end{cases} \quad (S93)$$

ψ_{py}^{-1} is the proteome efficiency for biomass generation using pyruvate in the biomass synthesis pathway, with

$$\psi_{py} = \frac{1}{\kappa_t} + \frac{1 + \eta_{a1} + \eta_c}{\kappa_{py}} + \frac{1 - \eta_b + \eta_{a1}}{\kappa_7} + \frac{\eta_b + \eta_c}{\kappa_8} + \frac{\eta_{a1}}{\kappa_9} + \frac{\eta_c}{\kappa_3} + \frac{\eta_c + \eta_d}{\kappa_5} + \sum_i^{a1,a2,b,c,d} \frac{\eta_i}{\kappa_i}. \quad (S94)$$

φ_{py} is an energy demand coefficient (a constant), with

$$\varphi_{py} \equiv \eta_E + \beta_7 \cdot (1 - \eta_b + \eta_{a1}) + \beta_9 \cdot \eta_{a1} - \beta_8 \cdot (\eta_c + \eta_b) - \beta_3 \cdot \eta_c - \beta_{a1} \cdot \eta_{a1}, \quad (S95)$$

Evidently, Eq. S91 is identical in form with Eq. S29. The growth rate changes into κ_{py} dependent:

$$\lambda(\kappa_{py}) = \begin{cases} \frac{\phi_{\max}}{\varphi_{py}/\varepsilon_r^{(py)}(\kappa_{py}) + \psi_{py}(\kappa_{py})} & \varepsilon_r^{(py)}(\kappa_{py}) > \varepsilon_f^{(py)}(\kappa_{py}), \\ \frac{\phi_{\max}}{\varphi_{py}/\varepsilon_f^{(py)}(\kappa_{py}) + \psi_{py}(\kappa_{py})} & \varepsilon_r^{(py)}(\kappa_{py}) < \varepsilon_f^{(py)}(\kappa_{py}). \end{cases} \quad (S96)$$

When κ_{py} is very small, combined with Eq. S93, then,

$$\begin{cases} \varepsilon_r^{(\text{py})}(\kappa_{\text{py}} \rightarrow 0) \approx \beta_r^{(\text{py})} \cdot \kappa_{\text{py}}, \\ \varepsilon_f^{(\text{py})}(\kappa_{\text{py}} \rightarrow 0) \approx \beta_f^{(\text{py})} \cdot \kappa_{\text{py}}. \end{cases} \quad (\text{S97})$$

Obviously, $\beta_r^{(\text{py})} \gg \beta_f^{(\text{py})}$, and hence

$$\varepsilon_r^{(\text{py})}(\kappa_{\text{py}} \rightarrow 0) > \varepsilon_f^{(\text{py})}(\kappa_{\text{py}} \rightarrow 0). \quad (\text{S98})$$

As long as

$$\frac{\beta_r^{(\text{py})} - \beta_f^{(\text{py})}}{\kappa_{\text{py}}^{(\text{ST})}} < \beta_f^{(\text{py})} \left(\frac{1}{\kappa_8} + \frac{1}{\kappa_3} + \frac{1}{\kappa_4} \right) - \beta_r^{(\text{py})} \cdot \left(\frac{1}{\kappa_8} + \frac{1}{\kappa_6} \right), \quad (\text{S99})$$

where the superscript “(ST)” stands for the saturated concentration, then,

$$\varepsilon_r^{(\text{py})}(\kappa_{\text{py}}^{(\text{ST})}) < \varepsilon_f^{(\text{py})}(\kappa_{\text{py}}^{(\text{ST})}), \quad (\text{S100})$$

and there exists a critical value of κ_{py} , denoted as $\kappa_{\text{py}}^{(\text{C})}$, with

$$\begin{cases} \varepsilon_r^{(\text{py})}(\kappa_{\text{py}}^{(\text{C})}) = \varepsilon_f^{(\text{py})}(\kappa_{\text{py}}^{(\text{C})}) = \frac{\beta_r^{(\text{py})} - \beta_f^{(\text{py})}}{1/\kappa_3 + 1/\kappa_4 - 1/\kappa_6} = \frac{\beta_3 + \beta_4 - \beta_6}{1/\kappa_3 + 1/\kappa_4 - 1/\kappa_6}, \\ \lambda_{\text{C}}^{(\text{py})} \equiv \lambda(\kappa_{\text{py}}^{(\text{C})}) = \frac{\phi_{\text{max}}}{\varphi_{\text{py}} / \varepsilon_{r/f}^{(\text{py})}(\kappa_{\text{py}}^{(\text{C})}) + \psi_{\text{py}}(\kappa_{\text{py}}^{(\text{C})})}. \end{cases} \quad (\text{S101})$$

Here, $\lambda_{\text{C}}^{(\text{py})}$ is the growth rate at the transition point, and $\varepsilon_{r/f}^{(\text{py})}$ stands for either $\varepsilon_r^{(\text{py})}$ or $\varepsilon_f^{(\text{py})}$. In Appendix-fig. 2H, we show the dependencies of $\varepsilon_r^{(\text{py})}(\kappa_{\text{py}})$, $\varepsilon_f^{(\text{py})}(\kappa_{\text{py}})$ and $\lambda(\kappa_{\text{py}})$ on κ_{py} in a 3-dimensional form. In the homogeneous case, $J_f^{(\text{E,py})}$ and $J_r^{(\text{E,py})}$ follow:

$$\begin{cases} J_f^{(\text{E,py})} = \varphi_{\text{py}} \cdot \lambda \cdot \theta(\lambda - \lambda_{\text{C}}^{(\text{py})}), \\ J_r^{(\text{E,py})} = \varphi_{\text{py}} \cdot \lambda \cdot [1 - \theta(\lambda - \lambda_{\text{C}}^{(\text{py})})]. \end{cases} \quad (\text{S102})$$

Defining $\lambda_{\text{max}}^{(\text{py})} = \lambda(\kappa_{\text{py}}^{(\text{ST})})$, and then, $[0, \lambda_{\text{max}}^{(\text{py})}]$ is the relevant range of the x axis. To compare with experiments, we assume the same extent of extrinsic noise in k_i^{cat} as specified in Appendix 2.3. Then, $\lambda_{\text{C}}^{(\text{py})}$ approximately follows a Gaussian distribution:

$$\lambda_{\text{C}}^{(\text{py})} \sim \mathcal{N}\left(\mu_{\lambda_{\text{C}}^{(\text{py})}}, \sigma_{\lambda_{\text{C}}^{(\text{py})}}^2\right), \quad (\text{S103})$$

where $\mu_{\lambda_c^{(py)}}$ and $\sigma_{\lambda_c^{(py)}}$ stand for the mean and standard deviation of $\lambda_c^{(py)}$. Then, the relations between the normalized energy fluxes and growth rate are:

$$\begin{cases} J_f^{(E,py)}(\lambda) = \frac{1}{2} \varphi_{py} \cdot \lambda \cdot \left[\operatorname{erf} \left(\frac{\lambda - \mu_{\lambda_c^{(py)}}}{\sqrt{2} \sigma_{\lambda_c^{(py)}}} \right) + 1 \right], \\ J_r^{(E,py)}(\lambda) = \frac{1}{2} \varphi_{py} \cdot \lambda \cdot \left[1 - \operatorname{erf} \left(\frac{\lambda - \mu_{\lambda_c^{(py)}}}{\sqrt{2} \sigma_{\lambda_c^{(py)}}} \right) \right]. \end{cases} \quad (\text{S104})$$

Combined with Eq. S92, we have:

$$\begin{cases} J_f^{(N)}(\lambda) = \frac{\varphi_{py}}{2\beta_f^{(py)}} \cdot \lambda \cdot \left[\operatorname{erf} \left(\frac{\lambda - \mu_{\lambda_c^{(py)}}}{\sqrt{2} \sigma_{\lambda_c^{(py)}}} \right) + 1 \right], \\ J_r^{(N)}(\lambda) = \frac{\varphi_{py}}{2\beta_r^{(py)}} \cdot \lambda \cdot \left[1 - \operatorname{erf} \left(\frac{\lambda - \mu_{\lambda_c^{(py)}}}{\sqrt{2} \sigma_{\lambda_c^{(py)}}} \right) \right]. \end{cases} \quad (\text{S105})$$

In Fig. 3F, we show that the model predictions (Eq. S105) align quantitatively with the experimental results (Holms, 1996).

Appendix 4.2 Mixture of a Group A carbon source with extracellular amino acids

In the case of a Group A carbon source mixed with amino acids, the coarse-grained model is shown in Appendix-fig. 2A. This model can be used to analyze mixtures with one or multiple types of extracellular amino acids. Here, Eqs. S21, S22, S24 and S25 still apply, but Eq. S23 changes to (the case of $i = a1$ remains the same as Eq. S23):

$$\Phi_i \cdot \xi_i \cdot N_{EP_i}^{\text{carbon}} + \Phi'_i \cdot \xi'_i \cdot N_{P_i}^{\text{carbon}} = r_i \cdot J_{\text{BM}} \quad (i = a2, b, c, d). \quad (\text{S106})$$

Here, $N_{P_i}^{\text{carbon}}$ represents the number of carbon atoms in a molecule of Pool i . For simplicity, we assume:

$$N_{P_i}^{\text{carbon}} \approx N_{EP_i}^{\text{carbon}}. \quad (\text{S107})$$

In the case where all 21 types of amino acids are present and each is at saturated concentration (denoted as “21AA”), we have:

$$\left\{ \begin{array}{l}
\phi_A \cdot \kappa_A = \phi_1 \cdot \kappa_1 + \phi_{a1} \cdot \kappa_{a1}, \\
2\phi_1 \cdot \kappa_1 = \phi_2 \cdot \kappa_2 + \phi_5 \cdot \kappa_5 + \phi_{a2} \cdot \kappa_{a2}, \\
\phi_2 \cdot \kappa_2 = \phi_3 \cdot \kappa_3 + \phi_6 \cdot \kappa_6 + \phi_b \cdot \kappa_b, \\
\phi_5 \cdot \kappa_5 + \phi_4 \cdot \kappa_4 = \phi_3 \cdot \kappa_3 + \phi_d \cdot \kappa_d, \\
\phi_3 \cdot \kappa_3 = \phi_4 \cdot \kappa_4 + \phi_c \cdot \kappa_c, \\
\phi_{a1} \cdot \kappa_{a1} = \eta_{a1} \cdot \lambda, \phi_{a2} \cdot \kappa_{a2} + \phi_{a2}^{(21AA)} \cdot \kappa_{a2}^{(21AA)} = \eta_{a2} \cdot \lambda, \phi_b \cdot \kappa_b + \phi_b^{(21AA)} \cdot \kappa_b^{(21AA)} = \eta_b \cdot \lambda, \\
\phi_c \cdot \kappa_c + \phi_c^{(21AA)} \cdot \kappa_c^{(21AA)} = \eta_c \cdot \lambda, \phi_d \cdot \kappa_d + \phi_d^{(21AA)} \cdot \kappa_d^{(21AA)} = \eta_d \cdot \lambda, \\
\beta_1 \cdot \phi_1 \cdot \kappa_1 + \beta_2 \cdot \phi_2 \cdot \kappa_2 + \beta_3 \cdot \phi_3 \cdot \kappa_3 + \beta_4 \cdot \phi_4 \cdot \kappa_4 + \beta_6 \cdot \phi_6 \cdot \kappa_6 + \beta_{a1} \cdot \phi_{a1} \cdot \kappa_{a1} = J_E^{(N)}, \\
J_E^{(N)} = \eta_E \cdot \lambda, \lambda = \phi_R \cdot \kappa_R, J_r^{(N)} = \phi_4 \cdot \kappa_4, J_f^{(N)} = \phi_6 \cdot \kappa_6, \\
\phi_R + \phi_A + \sum_i^6 \phi_i + \sum_j^{a1,a2,b,c,d} \phi_j + \phi_{a2}^{(21AA)} + \phi_b^{(21AA)} + \phi_c^{(21AA)} + \phi_d^{(21AA)} = \phi_{\max},
\end{array} \right. \quad (S108)$$

where ϕ_i and κ_i are defined following Eqs. S9 and S12. Since the cell growth rate significantly increases with the mixture of amino acids, we deduce that Pools a2-d are supplied by amino acids in growth optimization, with

$$\phi_i = 0 \quad (i = a2, b, c, d). \quad (S109)$$

Amino acids should be more efficient in the supply of biomass synthesis than the Group A carbon source for Pools a2-d, i.e.,

$$\left\{ \begin{array}{l}
1/\kappa_{a2}^{(21AA)} < 1/\kappa_{a2} + 1/(2\kappa_1) + 1/(2\kappa_A), \\
1/\kappa_b^{(21AA)} < 1/\kappa_b + 1/\kappa_2 + 1/(2\kappa_1) + 1/(2\kappa_A), \\
1/\kappa_c^{(21AA)} < 1/\kappa_c + 1/\kappa_5 + 1/\kappa_3 + 1/\kappa_2 + 1/\kappa_1 + 1/\kappa_A, \\
1/\kappa_d^{(21AA)} < 1/\kappa_d + 1/\kappa_5 + 1/(2\kappa_1) + 1/(2\kappa_A).
\end{array} \right. \quad (S110)$$

In practice, the requirement for proteome efficiency when using amino acids is even higher, since the biomass synthesis pathway is accompanied by energy biogenesis for Group A carbon sources, but not for amino acids. Combining Eqs. S108 and S109, we have:

$$\left\{ \begin{array}{l}
J_r^{(E)} + J_f^{(E)} = \varphi_{21AA} \cdot \lambda, \\
\frac{J_r^{(E)}}{\varepsilon_r} + \frac{J_f^{(E)}}{\varepsilon_f} = \phi_{\max} - \psi_{21AA} \cdot \lambda,
\end{array} \right. \quad (S111)$$

where $J_r^{(E)}$, $J_f^{(E)}$ follow Eq. S30, while ε_r and ε_f follow Eq. S31. ψ_{21AA}^{-1} is the proteome efficiency for biomass generation in the biomass synthesis pathway under this nutrient condition, with

$$\psi_{21AA} = \frac{1}{\kappa_l} + \frac{\eta_{a1}}{\kappa_A} + \frac{\eta_{a1}}{\kappa_{a1}} + \frac{\eta_{a2}}{\kappa_{a2}^{(21AA)}} + \frac{\eta_b}{\kappa_b^{(21AA)}} + \frac{\eta_c}{\kappa_c^{(21AA)}} + \frac{\eta_d}{\kappa_d^{(21AA)}}. \quad (\text{S112})$$

φ_{21AA} is an energy demand coefficient, with

$$\varphi_{21AA} \equiv \eta_E - \beta_{a1} \cdot \eta_{a1}. \quad (\text{S113})$$

Combining Eqs. S111 and S31, the formula for the growth rate is:

$$\lambda(\kappa_A) = \begin{cases} \lambda_r^{(21AA)} \equiv \frac{\phi_{\max}}{\varphi_{21AA}/\varepsilon_r(\kappa_A) + \psi_{21AA}(\kappa_A)} & \varepsilon_r(\kappa_A) > \varepsilon_f(\kappa_A), \\ \lambda_f^{(21AA)} \equiv \frac{\phi_{\max}}{\varphi_{21AA}/\varepsilon_f(\kappa_A) + \psi_{21AA}(\kappa_A)} & \varepsilon_r(\kappa_A) < \varepsilon_f(\kappa_A). \end{cases} \quad (\text{S114})$$

In fact, Eqs. S37-S42 still apply. $\varepsilon_{r/f}(\kappa_A^{(C)})$ satisfies Eq. S43, while $\lambda_C^{(21AA)} \equiv \lambda(\kappa_A^{(C)})$ and $\lambda_{\max}^{(21AA)} \equiv \lambda(\kappa_A^{\max})$ are:

$$\begin{cases} \lambda_C^{(21AA)} = \frac{\phi_{\max}}{\varphi_{21AA}/\varepsilon_{r/f}(\kappa_A^{(C)}) + \psi_{21AA}(\kappa_A^{(C)})}, \\ \lambda_{\max}^{(21AA)} = \frac{\phi_{\max}}{\varphi_{21AA}/\varepsilon_f(\kappa_A^{\max}) + \psi_{21AA}(\kappa_A^{\max})}. \end{cases} \quad (\text{S115})$$

When extrinsic noise is taken into account, $\lambda_C^{(21AA)}$ approximately follows a Gaussian distribution:

$$\lambda_C^{(21AA)} \sim \mathcal{N}\left(\mu_{\lambda_C^{(21AA)}}, \sigma_{\lambda_C^{(21AA)}}^2\right), \quad (\text{S116})$$

and the normalized fluxes $J_r^{(N)}$, $J_f^{(N)}$ change to:

$$\begin{cases} J_f^{(N)}(\lambda) = \frac{\varphi_{21AA}}{\beta_f^{(A)}} \cdot \lambda \cdot \left[\text{erf}\left(\frac{\lambda - \mu_{\lambda_C^{(21AA)}}}{\sqrt{2}\sigma_{\lambda_C^{(21AA)}}}\right) + 1 \right], \\ J_r^{(N)}(\lambda) = \frac{\varphi_{21AA}}{\beta_r^{(A)}} \cdot \lambda \cdot \left[1 - \text{erf}\left(\frac{\lambda - \mu_{\lambda_C^{(21AA)}}}{\sqrt{2}\sigma_{\lambda_C^{(21AA)}}}\right) \right]. \end{cases} \quad (\text{S117})$$

The above analysis can be extended to cases where a Group A carbon source is mixed with arbitrary combinations of amino acids. Eqs. S111, S114-S117 would remain in a similar form, while Eqs. S112-S113 would change depending on the combinations of amino acid. In Appendix-fig. 2B-C, we compare model predictions (see also Appendix 7.2 and Eq. S157) with

experimental data (Basan et al., 2015; Wallden et al., 2016) from mixtures of 21 or 7 types of amino acids along with a Group A carbon source, demonstrating quantitative agreement. Additionally, the increase in the critical threshold of growth rate for the growth rate-dependent fermentation flux in mixtures with extracellular amino acids (i.e., $\lambda_c^{(21AA)}, \lambda_c^{(7AA)} > \lambda_c$, see Appendix-fig. 2C) has also been observed in other experimental findings (Peebo et al., 2015).

Appendix 5 Enzyme allocation upon perturbations

Appendix 5.1 Carbon limitation within Group A carbon sources

In Eq. S28, we present the model predictions for the dependencies of enzyme proteomic mass fractions on growth rate and energy fluxes. To compare with experiments, we assume the same extent of extrinsic noise in k_i^{cat} as specified in Appendix 2.3. Relative protein expression data for enzymes within glycolysis and the TCA cycle are available from existing studies and are comparable to the ϕ_1 - ϕ_4 enzymes of our model (Fig. 1B). Upon κ_A perturbation, κ_A is a variable while w_0 is fixed (see Appendix 1.5). Combining Eqs. S28 and S47 (with $w_0 = 0$), we obtain:

$$\begin{cases} \phi_1 = \frac{\lambda}{\kappa_1} \left\{ \frac{\varphi \cdot (\beta_r^{(A)} - \beta_f^{(A)})}{2\beta_r^{(A)} \cdot \beta_f^{(A)}} \cdot \left[\text{erf} \left(\frac{\lambda - \mu_{\lambda_c}}{\sqrt{2}\sigma_{\lambda_c}} \right) + 1 \right] + \frac{\varphi}{\beta_r^{(A)}} + \frac{\eta_{a2} + \eta_b + 2\eta_c + \eta_d}{2} \right\}, \\ \phi_2 = \frac{\lambda}{\kappa_2} \left\{ \frac{\varphi \cdot (\beta_r^{(A)} - \beta_f^{(A)})}{\beta_r^{(A)} \cdot \beta_f^{(A)}} \cdot \left[\text{erf} \left(\frac{\lambda - \mu_{\lambda_c}}{\sqrt{2}\sigma_{\lambda_c}} \right) + 1 \right] + \frac{2\varphi}{\beta_r^{(A)}} + \eta_b + \eta_c \right\}, \\ \phi_3 = \frac{\lambda}{\kappa_3} \left\{ \frac{\varphi}{\beta_r^{(A)}} \cdot \left[1 - \text{erf} \left(\frac{\lambda - \mu_{\lambda_c}}{\sqrt{2}\sigma_{\lambda_c}} \right) \right] + \eta_c \right\}, \\ \phi_4 = \frac{\lambda}{\kappa_4} \cdot \frac{\varphi}{\beta_r^{(A)}} \cdot \left[1 - \text{erf} \left(\frac{\lambda - \mu_{\lambda_c}}{\sqrt{2}\sigma_{\lambda_c}} \right) \right]. \end{cases} \quad (\text{S118})$$

In Appendix-fig. 3C-D, we show the comparisons between model predictions (Eq. S118, $w_0 = 0$) and experimental data (Hui et al., 2015), which are consistent overall. We then consider the influence of maintenance energy as specified in Appendix 3.2. Here, we continue to choose $w_0 = 2.5$ (h^{-1}) as previously adopted in Appendix 3.3. Thus, Eq. S28 still holds. Combined with Eq. S85 under the condition that $\iota = 0$, we have:

$$\left\{ \begin{aligned}
\phi_1 &= \frac{1}{2 \cdot \kappa_1} \left\{ \frac{\varphi \cdot \lambda + w_0}{\beta_f^{(A)}} \cdot \left[\operatorname{erf} \left(\frac{\lambda - \mu_{\lambda_c}}{\sqrt{2} \sigma_{\lambda_c}} \right) + 1 \right] + \frac{\varphi \cdot \lambda + w_0}{\beta_r^{(A)}} \cdot \left[1 - \operatorname{erf} \left(\frac{\lambda - \mu_{\lambda_c}}{\sqrt{2} \sigma_{\lambda_c}} \right) \right] + (\eta_{a_2} + \eta_b + 2\eta_c + \eta_d) \lambda \right\}, \\
\phi_2 &= \frac{1}{\kappa_2} \left\{ \frac{\varphi \cdot \lambda + w_0}{\beta_f^{(A)}} \cdot \left[\operatorname{erf} \left(\frac{\lambda - \mu_{\lambda_c}}{\sqrt{2} \sigma_{\lambda_c}} \right) + 1 \right] + \frac{\varphi \cdot \lambda + w_0}{\beta_r^{(A)}} \cdot \left[1 - \operatorname{erf} \left(\frac{\lambda - \mu_{\lambda_c}}{\sqrt{2} \sigma_{\lambda_c}} \right) \right] + (\eta_b + \eta_c) \lambda \right\}, \\
\phi_3 &= \frac{1}{\kappa_3} \left\{ \frac{\varphi \cdot \lambda + w_0}{\beta_r^{(A)}} \cdot \left[1 - \operatorname{erf} \left(\frac{\lambda - \mu_{\lambda_c}}{\sqrt{2} \sigma_{\lambda_c}} \right) \right] + \eta_c \cdot \lambda \right\}, \\
\phi_4 &= \frac{1}{\kappa_4} \cdot \frac{\varphi \cdot \lambda + w_0}{\beta_r^{(A)}} \cdot \left[1 - \operatorname{erf} \left(\frac{\lambda - \mu_{\lambda_c}}{\sqrt{2} \sigma_{\lambda_c}} \right) \right].
\end{aligned} \right. \tag{S119}$$

In Fig. 4A-B, we show that the model predictions (Eq. S119, $w_0 = 2.5 \text{ (} h^{-1} \text{)}$) generally agree with the experiments (Hui et al., 2015). However, there are different basal expressions of these enzymes, likely due to living demands other than cell proliferation, such as preparation for starvation (Mori et al., 2017) or changes in the type of the nutrient (Basan et al., 2020; Kussell and Leibler, 2005).

Appendix 5.2 Overexpression of useless proteins

In the case of ϕ_Z perturbation under each nutrient condition with fixed κ_A (see Appendix 3.1), we consider the same extent of extrinsic noise in k_i^{cat} as specified in Appendix 2.3. The relation between enzyme allocation and growth rate can be obtained by combining Eqs. S28 and S58 (with $w_0 = 0$):

$$\left\{ \begin{aligned}
\phi_1 &= \frac{\lambda}{2 \cdot \kappa_1} \left\{ \frac{\varphi}{\beta_r^{(A)}} \cdot \left[1 - \operatorname{erf} \left(\frac{\lambda(\kappa_A, 0) - \mu_{\lambda_c}(0)}{\sqrt{2} \sigma_{\lambda_c}(0)} \right) \right] + \frac{\varphi}{\beta_f^{(A)}} \cdot \left[\operatorname{erf} \left(\frac{\lambda(\kappa_A, 0) - \mu_{\lambda_c}(0)}{\sqrt{2} \sigma_{\lambda_c}(0)} \right) + 1 \right] + (\eta_{a_2} + \eta_b + 2\eta_c + \eta_d) \right\}, \\
\phi_2 &= \frac{\lambda}{\kappa_2} \left\{ \frac{\varphi}{\beta_r^{(A)}} \cdot \left[1 - \operatorname{erf} \left(\frac{\lambda(\kappa_A, 0) - \mu_{\lambda_c}(0)}{\sqrt{2} \sigma_{\lambda_c}(0)} \right) \right] + \frac{\varphi}{\beta_f^{(A)}} \cdot \left[\operatorname{erf} \left(\frac{\lambda(\kappa_A, 0) - \mu_{\lambda_c}(0)}{\sqrt{2} \sigma_{\lambda_c}(0)} \right) + 1 \right] + (\eta_b + \eta_c) \right\}, \\
\phi_3 &= \frac{\lambda}{\kappa_3} \left\{ \frac{\varphi}{\beta_r^{(A)}} \cdot \left[1 - \operatorname{erf} \left(\frac{\lambda(\kappa_A, 0) - \mu_{\lambda_c}(0)}{\sqrt{2} \sigma_{\lambda_c}(0)} \right) \right] + \eta_c \right\}, \\
\phi_4 &= \frac{\lambda}{\kappa_4} \left\{ \frac{\varphi}{\beta_r^{(A)}} \cdot \left[1 - \operatorname{erf} \left(\frac{\lambda(\kappa_A, 0) - \mu_{\lambda_c}(0)}{\sqrt{2} \sigma_{\lambda_c}(0)} \right) \right] \right\}.
\end{aligned} \right. \tag{S120}$$

Here $\lambda(\kappa_A, 0)$ is the growth rate for $\phi_Z = 0$, and thus it is a parameter rather than a variable. The growth rate is defined as $\lambda(\kappa_A, \phi_Z)$, which follows Eq. S50. Thus, ϕ_i is proportional to the growth rate λ . In Appendix-fig. 3E-F, we observe that the model predictions (Eq. S120) generally agree with the experiments (Basan et al., 2015). Next, we consider the influence of maintenance energy with $w_0 = 2.5$ (h^{-1}). Combining Eqs. S28, S58 and S85 (with $\iota = 0$), we get:

$$\begin{aligned}
\phi_1 &= \frac{w_0}{2\kappa_1} \left\{ \frac{1}{\beta_f^{(A)}} \cdot \left[\operatorname{erf} \left(\frac{\lambda(\kappa_A, 0) - \mu_{\lambda_c}(0)}{\sqrt{2}\sigma_{\lambda_c}(0)} \right) + 1 \right] + \frac{1}{\beta_r^{(A)}} \cdot \left[1 - \operatorname{erf} \left(\frac{\lambda(\kappa_A, 0) - \mu_{\lambda_c}(0)}{\sqrt{2}\sigma_{\lambda_c}(0)} \right) \right] \right\} \\
&+ \frac{\lambda}{2\kappa_1} \left\{ \frac{\varphi}{\beta_f^{(A)}} \cdot \left[\operatorname{erf} \left(\frac{\lambda(\kappa_A, 0) - \mu_{\lambda_c}(0)}{\sqrt{2}\sigma_{\lambda_c}(0)} \right) + 1 \right] + \frac{\varphi}{\beta_r^{(A)}} \cdot \left[1 - \operatorname{erf} \left(\frac{\lambda(\kappa_A, 0) - \mu_{\lambda_c}(0)}{\sqrt{2}\sigma_{\lambda_c}(0)} \right) \right] + (\eta_{a2} + \eta_b + 2\eta_c + \eta_d) \right\}, \\
\phi_2 &= \frac{w_0}{\kappa_2} \left\{ \frac{1}{\beta_f^{(A)}} \cdot \left[\operatorname{erf} \left(\frac{\lambda(\kappa_A, 0) - \mu_{\lambda_c}(0)}{\sqrt{2}\sigma_{\lambda_c}(0)} \right) + 1 \right] + \frac{1}{\beta_r^{(A)}} \cdot \left[1 - \operatorname{erf} \left(\frac{\lambda(\kappa_A, 0) - \mu_{\lambda_c}(0)}{\sqrt{2}\sigma_{\lambda_c}(0)} \right) \right] \right\} \\
&+ \frac{\lambda}{\kappa_2} \left\{ \frac{\varphi}{\beta_f^{(A)}} \cdot \left[\operatorname{erf} \left(\frac{\lambda(\kappa_A, 0) - \mu_{\lambda_c}(0)}{\sqrt{2}\sigma_{\lambda_c}(0)} \right) + 1 \right] + \frac{\varphi}{\beta_r^{(A)}} \cdot \left[1 - \operatorname{erf} \left(\frac{\lambda(\kappa_A, 0) - \mu_{\lambda_c}(0)}{\sqrt{2}\sigma_{\lambda_c}(0)} \right) \right] + (\eta_b + \eta_c) \right\}, \\
\phi_3 &= \frac{\lambda}{\kappa_3} \left\{ \frac{\varphi}{\beta_r^{(A)}} \cdot \left[1 - \operatorname{erf} \left(\frac{\lambda(\kappa_A, 0) - \mu_{\lambda_c}(0)}{\sqrt{2}\sigma_{\lambda_c}(0)} \right) \right] + \eta_c \right\} + \frac{w_0}{\kappa_3} \cdot \frac{1}{\beta_r^{(A)}} \cdot \left[1 - \operatorname{erf} \left(\frac{\lambda(\kappa_A, 0) - \mu_{\lambda_c}(0)}{\sqrt{2}\sigma_{\lambda_c}(0)} \right) \right], \\
\phi_4 &= \frac{\lambda}{\kappa_4} \cdot \frac{\varphi}{\beta_r^{(A)}} \cdot \left[1 - \operatorname{erf} \left(\frac{\lambda(\kappa_A, 0) - \mu_{\lambda_c}(0)}{\sqrt{2}\sigma_{\lambda_c}(0)} \right) \right] + \frac{w_0}{\kappa_4} \cdot \frac{1}{\beta_r^{(A)}} \cdot \left[1 - \operatorname{erf} \left(\frac{\lambda(\kappa_A, 0) - \mu_{\lambda_c}(0)}{\sqrt{2}\sigma_{\lambda_c}(0)} \right) \right].
\end{aligned} \tag{S121}$$

Here, the growth rate is defined as $\lambda(\kappa_A, \phi_Z)$, and $\lambda(\kappa_A, 0)$ is a parameter rather than a variable. Thus, ϕ_i is a linear function of the growth rate λ , with a positive slope and a positive y -intercept. In Fig. 4C-D and Appendix-fig. 3I-J, we show that the model predictions (Eq. S121) agree quantitatively with the experimental data (Basan et al., 2015).

Appendix 5.3 Energy dissipation

In the case of energy dissipation under each nutrient condition, w is perturbed while κ_A is fixed. The relation between protein allocation and growth rate can be obtained by combining Eqs. S28 and S70. However, since w is explicitly present in Eq. S70, it is necessary to reduce this variable to obtain the growth rate dependence of enzyme allocation. From Eq. S64, we have:

$$\lambda(\kappa_A, w) = \lambda(\kappa_A, 0) \left\{ 1 - \frac{w}{\phi_{\max}} \cdot \left[\frac{1}{\varepsilon_r(\kappa_A)} - \theta(\varepsilon_f(\kappa_A) - \varepsilon_r(\kappa_A)) \cdot \left(\frac{1}{\varepsilon_r(\kappa_A)} - \frac{1}{\varepsilon_f(\kappa_A)} \right) \right] \right\}. \tag{S122}$$

Here, $\lambda(\kappa_A, 0) \equiv \lambda(\kappa_A, w = 0)$ (satisfying Eq. S64) is a parameter rather than a variable. “ θ ” stands for the Heaviside step function. Thus, we have:

$$w(\lambda) = \frac{\phi_{\max} \cdot [1 - \lambda/\lambda(\kappa_A, 0)]}{\left[1/\varepsilon_r(\kappa_A) - \theta(\varepsilon_f(\kappa_A) - \varepsilon_r(\kappa_A)) \cdot (1/\varepsilon_r(\kappa_A) - 1/\varepsilon_f(\kappa_A))\right]}, \quad (\text{S123})$$

where the energy dissipation coefficient w is regarded as a function of the growth rate.

Combining Eqs. S28, S70 and S123, we get:

$$\left\{ \begin{aligned} \phi_1 &= \frac{1}{2\kappa_1} \left[\frac{\varphi \cdot \lambda + w(\lambda)}{\beta_f^{(A)}} - \frac{\varphi \cdot \lambda + w(\lambda)}{\beta_r^{(A)}} \right] \cdot \left[\operatorname{erf} \left(\frac{\lambda - \mu_{\lambda_c}(0) \left\{ 1 - w/\left[\varepsilon_{r/f}(\kappa_A^{(C)}) \phi_{\max} \right] \right\}}{\sqrt{2}\sigma_{\lambda_c}(0) \left\{ 1 - w/\left[\varepsilon_{r/f}(\kappa_A^{(C)}) \phi_{\max} \right] \right\}} \right) + 1 \right] + \frac{2[\varphi \cdot \lambda + w(\lambda)]}{\beta_r^{(A)}} + (\eta_{a2} + \eta_b + 2\eta_c + \eta_d) \cdot \lambda, \\ \phi_2 &= \frac{1}{\kappa_2} \left[\frac{\varphi \cdot \lambda + w(\lambda)}{\beta_f^{(A)}} - \frac{\varphi \cdot \lambda + w(\lambda)}{\beta_r^{(A)}} \right] \cdot \left[\operatorname{erf} \left(\frac{\lambda - \mu_{\lambda_c}(0) \left\{ 1 - w/\left[\varepsilon_{r/f}(\kappa_A^{(C)}) \phi_{\max} \right] \right\}}{\sqrt{2}\sigma_{\lambda_c}(0) \left\{ 1 - w/\left[\varepsilon_{r/f}(\kappa_A^{(C)}) \phi_{\max} \right] \right\}} \right) + 1 \right] + \frac{2[\varphi \cdot \lambda + w(\lambda)]}{\beta_r^{(A)}} + (\eta_b + \eta_c) \cdot \lambda, \\ \phi_3 &= \frac{1}{\kappa_3} \left(\frac{\varphi \cdot \lambda + w(\lambda)}{\beta_r^{(A)}} \cdot \left[1 - \operatorname{erf} \left(\frac{\lambda - \mu_{\lambda_c}(0) \left\{ 1 - w(\lambda)/\left[\varepsilon_{r/f}(\kappa_A^{(C)}) \phi_{\max} \right] \right\}}{\sqrt{2}\sigma_{\lambda_c}(0) \left\{ 1 - w(\lambda)/\left[\varepsilon_{r/f}(\kappa_A^{(C)}) \phi_{\max} \right] \right\}} \right) \right] + \eta_c \cdot \lambda \right), \\ \phi_4 &= \frac{1}{\kappa_4} \cdot \frac{\varphi \cdot \lambda + w(\lambda)}{\beta_r^{(A)}} \cdot \left[1 - \operatorname{erf} \left(\frac{\lambda - \mu_{\lambda_c}(0) \left\{ 1 - w(\lambda)/\left[\varepsilon_{r/f}(\kappa_A^{(C)}) \phi_{\max} \right] \right\}}{\sqrt{2}\sigma_{\lambda_c}(0) \left\{ 1 - w(\lambda)/\left[\varepsilon_{r/f}(\kappa_A^{(C)}) \phi_{\max} \right] \right\}} \right) \right], \end{aligned} \right. \quad (\text{S124})$$

where $w(\lambda)$ follows Eq. S123. When κ_A lies in the vicinity of $\kappa_A^{(C)}$ or w is small so that

$$\left(1 - \frac{w}{\varepsilon_{r/f}(\kappa_A) \cdot \phi_{\max}} \right) \bigg/ \left(1 - \frac{w}{\varepsilon_{r/f}(\kappa_A^{(C)}) \cdot \phi_{\max}} \right) \approx 1, \quad (\text{S125})$$

then we have:

$$\left\{ \begin{aligned} J_f^{(N)}(\lambda, w) &= \frac{\varphi \cdot \lambda + w}{\beta_f^{(A)}} \cdot \left[\operatorname{erf} \left(\frac{\lambda(\kappa_A, 0) - \mu_{\lambda_c}(0)}{\sqrt{2}\sigma_{\lambda_c}(0)} \right) + 1 \right], \\ J_r^{(N)}(\lambda, w) &= \frac{\varphi \cdot \lambda + w}{\beta_r^{(A)}} \cdot \left[1 - \operatorname{erf} \left(\frac{\lambda(\kappa_A, 0) - \mu_{\lambda_c}(0)}{\sqrt{2}\sigma_{\lambda_c}(0)} \right) \right], \end{aligned} \right. \quad (\text{S126})$$

and thus:

$$\left\{ \begin{aligned}
\phi_1 &= \frac{1}{2\kappa_1} \left\{ \left[\frac{\varphi \cdot \lambda + w(\lambda)}{\beta_f^{(A)}} - \frac{\varphi \cdot \lambda + w(\lambda)}{\beta_r^{(A)}} \right] \cdot \left[\operatorname{erf} \left(\frac{\lambda(\kappa_A, 0) - \mu_{\lambda_c}(0)}{\sqrt{2}\sigma_{\lambda_c}(0)} \right) + 1 \right] + \frac{2[\varphi \cdot \lambda + w(\lambda)]}{\beta_r^{(A)}} + (\eta_{a2} + \eta_b + 2\eta_c + \eta_d) \cdot \lambda \right\}, \\
\phi_2 &= \frac{1}{\kappa_2} \left[\left[\frac{\varphi \cdot \lambda + w(\lambda)}{\beta_f^{(A)}} - \frac{\varphi \cdot \lambda + w(\lambda)}{\beta_r^{(A)}} \right] \cdot \left[\operatorname{erf} \left(\frac{\lambda(\kappa_A, 0) - \mu_{\lambda_c}(0)}{\sqrt{2}\sigma_{\lambda_c}(0)} \right) + 1 \right] + \frac{2[\varphi \cdot \lambda + w(\lambda)]}{\beta_r^{(A)}} + (\eta_b + \eta_c) \cdot \lambda \right], \\
\phi_3 &= \frac{1}{\kappa_3} \left(\frac{\varphi \cdot \lambda + w(\lambda)}{\beta_r^{(A)}} \cdot \left[1 - \operatorname{erf} \left(\frac{\lambda(\kappa_A, 0) - \mu_{\lambda_c}(0)}{\sqrt{2}\sigma_{\lambda_c}(0)} \right) \right] + \eta_c \cdot \lambda \right), \\
\phi_4 &= \frac{1}{\kappa_4} \cdot \frac{\varphi \cdot \lambda + w(\lambda)}{\beta_r^{(A)}} \cdot \left[1 - \operatorname{erf} \left(\frac{\lambda(\kappa_A, 0) - \mu_{\lambda_c}(0)}{\sqrt{2}\sigma_{\lambda_c}(0)} \right) \right],
\end{aligned} \right. \tag{S127}$$

Note that in Eq. S123, w is a linear function of λ with a negative slope. Thus ϕ_i exhibits a linear relation with λ when Eq. S125 is satisfied (see Eq. S127). In fact, the slope of ϕ_4 is certainly negative (combining Eqs. S64, S123 and S127), while the sign of the slope for other ϕ_i depends on parameters. For a given nutrient, the enzymes corresponding to the same ϕ_i should exhibit the same slope sign. Another restriction is that if the slope sign of ϕ_1 is negative, then the slope sign of ϕ_2 is surely negative. In Appendix-fig. 3K-N, we show that our model results agree well with the experimental data (Basan et al., 2015) (Eq. S127).

Appendix 6 Other aspects of the model

Appendix 6.1 A coarse-grained model with more details

To compare with experiments, we consider a coarse-grained model with more details, as shown in Appendix-fig. 2F. Here, nodes M_6 , M_7 represent GA3P and DHAP, respectively. Other nodes follow the descriptions specified in Appendix 2.1. Each biochemical reaction follows Eq. S5 with $b_i = 1$ except that $M_1 \rightarrow M_6 + M_7$ and $M_3 + M_5 \rightarrow M_4$. By applying flux balance to the stoichiometric fluxes, combined with Eq. S8, we obtain:

$$\left\{ \begin{aligned}
\Phi_A \cdot \xi_A &= \Phi_1 \cdot \xi_1 + \Phi_{a1} \cdot \xi_{a1}, \\
\Phi_{11} \cdot \xi_{11} &= \Phi_{10} \cdot \xi_{10} + \Phi_1 \cdot \xi_1, \Phi_{10} \cdot \xi_{10} = \Phi_1 \cdot \xi_1, \\
\Phi_{11} \cdot \xi_{11} &= \Phi_2 \cdot \xi_2 + \Phi_5 \cdot \xi_5 + \Phi_{a2} \cdot \xi_{a2}, \\
\Phi_2 \cdot \xi_2 &= \Phi_3 \cdot \xi_3 + \Phi_6 \cdot \xi_6 + \Phi_b \cdot \xi_b, \\
\Phi_5 \cdot \xi_5 + \Phi_4 \cdot \xi_4 &= \Phi_3 \cdot \xi_3 + \Phi_d \cdot \xi_d, \\
\Phi_3 \cdot \xi_3 &= \Phi_4 \cdot \xi_4 + \Phi_c \cdot \xi_c.
\end{aligned} \right. \tag{S128}$$

While Eqs. S22-S25 still hold. By applying the substitutions specified in Eqs. S9, S12, S14-S18, combined with Eqs. S4, S10, S22-S25, S128, and the constraint of proteome resource allocation, we get:

$$\begin{cases}
\phi_A \cdot \kappa_A = \phi_1 \cdot \kappa_1 + \phi_{a1} \cdot \kappa_{a1}, \\
\phi_{11} \cdot \kappa_{11} = \phi_{10} \cdot \kappa_{10} + \phi_1 \cdot \kappa_1, \phi_{10} \cdot \kappa_{10} = \phi_1 \cdot \kappa_1, \\
\phi_{11} \cdot \kappa_{11} = \phi_2 \cdot \kappa_2 + \phi_5 \cdot \kappa_5 + \phi_{a2} \cdot \kappa_{a2}, \\
\phi_2 \cdot \kappa_2 = \phi_3 \cdot \kappa_3 + \phi_6 \cdot \kappa_6 + \phi_b \cdot \kappa_b, \\
\phi_5 \cdot \kappa_5 + \phi_4 \cdot \kappa_4 = \phi_3 \cdot \kappa_3 + \phi_d \cdot \kappa_d, \\
\phi_3 \cdot \kappa_3 = \phi_4 \cdot \kappa_4 + \phi_c \cdot \kappa_c, \\
\phi_{a1} \cdot \kappa_{a1} = \eta_{a1} \cdot \lambda, \phi_{a2} \cdot \kappa_{a2} = \eta_{a2} \cdot \lambda, \phi_b \cdot \kappa_b = \eta_b \cdot \lambda, \phi_c \cdot \kappa_c = \eta_c \cdot \lambda, \phi_d \cdot \kappa_d = \eta_d \cdot \lambda, \\
\beta_1 \cdot \phi_1 \cdot \kappa_1 + \beta_2 \cdot \phi_2 \cdot \kappa_2 + \beta_3 \cdot \phi_3 \cdot \kappa_3 + \beta_4 \cdot \phi_4 \cdot \kappa_4 + \beta_6 \cdot \phi_6 \cdot \kappa_6 + \beta_{a1} \cdot \phi_{a1} \cdot \kappa_{a1} = J_E^{(N)}, \\
J_E^{(N)} = \eta_E \cdot \lambda, \lambda = \phi_R \cdot \kappa_r, J_r^{(N)} = \phi_4 \cdot \kappa_4, J_f^{(N)} = \phi_6 \cdot \kappa_6, \\
\phi_R + \phi_A + \phi_1 + \phi_2 + \phi_3 + \phi_4 + \phi_5 + \phi_6 + \phi_7 + \phi_8 + \phi_{a1} + \phi_{a2} + \phi_b + \phi_c + \phi_d = \phi_{\max}.
\end{cases} \tag{S129}$$

Then, Eq. S28 still holds, while ϕ_{10} and ϕ_{11} are:

$$\begin{cases}
\phi_{10} = \left[J_r^{(N)} + J_f^{(N)} + (\eta_{a2} + \eta_b + 2\eta_c + \eta_d) \lambda \right] / (2 \cdot \kappa_{10}), \\
\phi_{11} = \left[J_r^{(N)} + J_f^{(N)} + (\eta_{a2} + \eta_b + 2\eta_c + \eta_d) \lambda \right] / \kappa_{11}.
\end{cases} \tag{S130}$$

By substituting Eqs. S28 and S130 into Eq. S129, we get:

$$\begin{cases}
J_r^{(E)} + J_f^{(E)} = \varphi \cdot \lambda, \\
\frac{J_r^{(E)}}{\varepsilon_r^{(dt)}} + \frac{J_f^{(E)}}{\varepsilon_f^{(dt)}} = \phi_{\max} - \psi_{dt} \cdot \lambda,
\end{cases} \tag{S131}$$

where “dt” stands for details. Eqs. S30 and S33 still hold. $\varepsilon_r^{(dt)}$ and $\varepsilon_f^{(dt)}$ represent the proteome efficiencies for energy biogenesis in the respiration and fermentation pathways, respectively, with

$$\begin{cases}
\varepsilon_r^{(dt)} = \frac{\beta_r^{(A)}}{1/\kappa_A + 1/\kappa_1 + 1/\kappa_{10} + 2/\kappa_{11} + 2/\kappa_2 + 2/\kappa_3 + 2/\kappa_4}, \\
\varepsilon_f^{(dt)} = \frac{\beta_f^{(A)}}{1/\kappa_A + 1/\kappa_1 + 1/\kappa_{10} + 2/\kappa_{11} + 2/\kappa_2 + 2/\kappa_6}.
\end{cases} \tag{S132}$$

ψ_{dt}^{-1} is the proteome efficiency for biomass generation in the biomass synthesis pathway, with

$$\psi_{dt}^{-1} = \frac{1}{\kappa_r} + \frac{1 + \eta_{a1} + \eta_c}{2\kappa_A} + (\eta_{a2} + \eta_b + 2\eta_c + \eta_d) \left(\frac{1}{2\kappa_1} + \frac{1}{2\kappa_{10}} + \frac{1}{\kappa_{11}} \right) + \frac{\eta_b + \eta_c}{\kappa_2} + \frac{\eta_c}{\kappa_3} + \frac{\eta_c + \eta_d}{\kappa_5} + \sum_i^{a1, a2, b, c, d} \frac{\eta_i}{\kappa_i}. \tag{S133}$$

Appendix 6.2 Estimation of the in vivo enzyme catalytic rates

We use the method introduced by Davidi *et al.* (Davidi et al., 2016), combined with proteome experimental data (Basan et al., 2015) (Appendix-table 2), to estimate the in vivo enzyme catalytic rates. Combining Eqs. S28 and S130, we have:

$$\left\{ \begin{array}{l} \kappa_1 = \left[J_r^{(N)} + J_f^{(N)} + (\eta_{a2} + \eta_b + 2\eta_c + \eta_d) \lambda \right] / (2 \cdot \phi_1), \\ \kappa_2 = \left[J_r^{(N)} + J_f^{(N)} + (\eta_b + \eta_c) \lambda \right] / \phi_2, \\ \kappa_3 = (J_r^{(N)} + \eta_c \cdot \lambda) / \phi_3, \kappa_4 = J_r^{(N)} / \phi_4, \\ \kappa_5 = (\eta_c + \eta_d) \lambda / \phi_5, \kappa_6 = J_f^{(N)} / \phi_6, \\ \kappa_{10} = \left[J_r^{(N)} + J_f^{(N)} + (\eta_{a2} + \eta_b + 2\eta_c + \eta_d) \lambda \right] / (2 \cdot \phi_{10}), \\ \kappa_{11} = \left[J_r^{(N)} + J_f^{(N)} + (\eta_{a2} + \eta_b + 2\eta_c + \eta_d) \lambda \right] / \phi_{11}. \end{array} \right. \quad (\text{S134})$$

Here, $J_r^{(N)}$, $J_f^{(N)}$, λ and ϕ_i ($i=1-6,10-11$) are measurable from experiments (see Appendix 8.1 and Appendix-table 2). Thus, we can obtain the in vivo values of κ_i from Eq. S134. Combined with Eqs. S17 and S20, we have

$$k_i^{\text{cat}} = \frac{r_{\text{carbon}}}{r_{\text{protein}}} \cdot \frac{m_{E_i}}{m_{\text{carbon}}} \cdot \kappa_i \cdot \left[\sum_i r_i / N_{\text{EP}_i}^{\text{carbon}} \right]. \quad (\text{S135})$$

Eq. S135 is the in vivo result for the enzyme catalytic rate. In Appendix-fig. 2G, we show a comparison between in vivo and in vitro results for k_{cat} values of enzymes within glycolysis and the TCA cycle, which are roughly consistent. In the applications, we prioritized the use of in vivo results for enzyme catalytic rates, and use in vitro data as a substitute when there were gaps.

Appendix 6.3 Comparison with existing models that illustrate experimental results

For the coarse-grained model described in Appendix 2, the normalized stoichiometric influx of a Group A carbon source is given by:

$$J_{in}^{(N)} \equiv J_A^{(N)} = \phi_A \cdot \kappa_A. \quad (\text{S136})$$

Combined with the first equation in Eq. S28 and Eq. S30, we obtain:

$$J_{in}^{(N)} - \mathcal{G} \cdot \lambda = \frac{J_r^{(E)}}{\beta_r^{(A)}} + \frac{J_f^{(E)}}{\beta_f^{(A)}}, \quad (\text{S137})$$

where $\mathcal{G} = \eta_{a1} + \eta_c + (\eta_{a2} + \eta_b + \eta_d) / 2$. Evidently, $\beta_r^{(A)}$, $\beta_f^{(A)}$ and \mathcal{G} are constant parameters. In this subsection, we highlight the major differences between our model presented in Appendix 2 and existing models that illustrate the growth rate dependence of fermentation flux in the standard picture of overflow metabolism (Basan et al., 2015; Holms, 1996; Meyer et al., 1984; Nanchen et al., 2006).

Based on the modeling principles rather than the detailed mechanisms, there are two major classes of existing models that can illustrate experimental results. Both classes of models regard the proteome efficiencies ε_r and ε_f as constants, with $\varepsilon_f > \varepsilon_r$ if used, or follow functionally equivalent propositions. However, in our model, ε_r and ε_f are both functions of κ_A , which vary significantly upon nutrient perturbation, with $\varepsilon_r(\kappa_A \rightarrow 0) > \varepsilon_f(\kappa_A \rightarrow 0)$ and $\varepsilon_r(\kappa_A^{\max}) < \varepsilon_f(\kappa_A^{\max})$ (see Eqs. S38, S40-S41). Furthermore, there are significant differences in the modeling and optimization principles, as listed below.

The first class of models (Chen and Nielsen, 2019; Majewski and Domach, 1990; Shlomi et al., 2011; Varma and Palsson, 1994; Vazquez et al., 2010; Vazquez and Oltvai, 2016; Zhuang et al., 2011) optimize the ratio of biomass outflow to carbon influx $\lambda/J_{in}^{(N)}$, either to optimize the growth rate for a given carbon influx or to minimize the carbon influx for a given growth rate. Since respiration is far more efficient than fermentation in terms of energy biogenesis per unit carbon, to optimize the ratio $\lambda/J_{in}^{(N)}$, cells would preferentially use respiration when the carbon influx is small. As carbon influx increases above a certain threshold, factors such as proteome allocation direct cells toward fermentation in a threshold-linear response, since they consider $\varepsilon_f > \varepsilon_r$. Our model is significantly different from this class of models in the optimization principle, as we purely optimize the cell growth rate for a given nutrient condition, without imposing a special constraint on the carbon influx.

The second class of models, represented by Basan *et al.* (Basan et al., 2015), also adopt the optimization of $\lambda/J_{in}^{(N)}$ in the interpretation of their model results. However, the growth rate dependence of fermentation flux was derived prior to the application of growth rate optimization (although it can be derived by optimizing $\lambda/J_{in}^{(N)}$). In fact, Eqs. S29 and S137 in our model are very similar in form to those in Basan *et al.* (Basan et al., 2015), yet there are critical differences, which we list below. In Eq. S29, by regarding $J_r^{(E)}$ and $J_f^{(E)}$ as the two variables in a system of linear equations, we obtain the following expressions:

$$\begin{cases} J_r^{(E)} = \frac{\phi_{\max} - (\psi + \varphi/\varepsilon_f) \cdot \lambda}{1/\varepsilon_r - 1/\varepsilon_f}, \\ J_f^{(E)} = \frac{(\psi + \varphi/\varepsilon_r) \cdot \lambda - \phi_{\max}}{1/\varepsilon_r - 1/\varepsilon_f}. \end{cases} \quad (\text{S138})$$

In Basan *et al.* (Basan et al., 2015), Eq. S138 is considered to be the relation between $J_{r/f}^{(E)}$ and λ upon nutrient (and thus $J_{in}^{(N)}$) perturbation, while ε_r and ε_f are regarded as constants throughout the perturbation. By contrast, in our model, Eq. S138 serves as a constraint under a given nutrient condition with fixed κ_A , and is not relevant to nutrient perturbation. For wild-type

strains, if $\varepsilon_r(\kappa_A) > \varepsilon_f(\kappa_A)$ (or vice versa), then the solution for optimal growth is

$$J_r^{(E)}(\kappa_A) = \varphi \cdot \lambda(\kappa_A) \text{ and } J_f^{(E)}(\kappa_A) = 0, \text{ with } \lambda(\kappa_A) = \frac{\varepsilon_r(\kappa_A) \cdot \phi_{\max}}{\varphi + \varepsilon_r(\kappa_A) \cdot \psi(\kappa_A)}. \text{ This solution, which}$$

satisfies Eq. S138, corresponds to a point rather than a line in the relation between growth rate λ and normalized energy flux $J_{r/f}^{(E)}$ upon κ_A perturbation.

Appendix 7 Probability density functions of variables and parameters

Appendix 7.1 Probability density function of κ_i

Enzyme catalysis is crucial for the survival of living organisms, as it significantly accelerates biochemical reactions by reducing the energy barrier between the substrate and product (Nelson et al., 2008). However, the maximal turnover rate of enzymes, k_{cat} , varies notably between in vivo and in vitro measurements (Davidi et al., 2016). Recent studies suggest that differences in the aquatic medium are the primary cause of this variation (Davidi et al., 2016; García-Contreras et al., 2012). In particular, potassium and phosphate concentrations have a significant influence on k_{cat} (García-Contreras et al., 2012), and these concentrations exhibit some degree of variation among cell populations under intracellular conditions (García-Contreras et al., 2012). For simplicity, we assume that the turnover rate of each enzyme E_i , k_i^{cat} , follows a Gaussian distribution $\mathcal{N}(\mu_{k_i^{\text{cat}}}, \sigma_{k_i^{\text{cat}}}^2)$ with $k_i^{\text{cat}} > 0$ among cells (representing extrinsic noise (Elowitz et al., 2002), denoted as χ_{ext}). The probability density function of k_i^{cat} is then given by:

$$k_i^{\text{cat}} \sim \mathcal{N}'(x; \mu_{k_i^{\text{cat}}}, \sigma_{k_i^{\text{cat}}}^2) = \begin{cases} \frac{1}{\sigma_{k_i^{\text{cat}}} \sqrt{2\pi}} e^{-\frac{1}{2} \left(\frac{x - \mu_{k_i^{\text{cat}}}}{\sigma_{k_i^{\text{cat}}}} \right)^2}, & x \geq 0. \\ 0, & x < 0. \end{cases} \quad (\text{S139})$$

When the CV of the k_i^{cat} distribution (i.e., $\sigma_{k_i^{\text{cat}}} / \mu_{k_i^{\text{cat}}}$) is less than 1/3, $\mathcal{N}'(x; \mu_{k_i^{\text{cat}}}, \sigma_{k_i^{\text{cat}}}^2)$ is almost identical to $\mathcal{N}(\mu_{k_i^{\text{cat}}}, \sigma_{k_i^{\text{cat}}}^2)$. In this case, $1/k_i^{\text{cat}}$ follows the positive inverse of Gaussian (IOG) distribution, and the probability density function is:

$$\text{IOG}(x; \mu_{1/k_i^{\text{cat}}}, \zeta_{1/k_i^{\text{cat}}}) = \begin{cases} \frac{1}{\sqrt{2\pi x^4}} \exp\left(-\frac{\zeta_{1/k_i^{\text{cat}}}}{2} \frac{(x - \mu_{1/k_i^{\text{cat}}})^2}{x^2 \mu_{1/k_i^{\text{cat}}}^2}\right), & x \geq 0, \\ 0, & x < 0, \end{cases} \quad (\text{S140})$$

where $\zeta_{1/k_i^{\text{cat}}} = 1/\sigma_{k_i^{\text{cat}}}^2$ is the shape parameter, and $\mu_{1/k_i^{\text{cat}}} = 1/\mu_{k_i^{\text{cat}}}$ is the mean.

Meanwhile, due to the stochastic nature of biochemical reactions, we apply Gillespie's chemical Langevin equation (Gillespie, 2000) to account for intrinsic noise (Elowitz et al., 2002) (denoted as χ_{int}). For cell size regulation of *E. coli* within a cell cycle, the cell mass at the initiation of DNA replication per chromosome origin remains constant (Donachie, 1968). Thus, the time required for enzyme E_i to complete a catalytic job (with a timescale of $1/k_i^{\text{cat}}$) can be approximated as the first passage time of a stochastic process, with

$$\begin{cases} X_i(t=0) = 0, \\ dX_i/dt = \alpha_i + \sqrt{\alpha_i} \Gamma_i(t), \\ T_{\Theta} = \inf \{t > 0 \mid X_i(t) = \Theta\}. \end{cases} \quad (\text{S141})$$

Here $\alpha_i \equiv k_i^{\text{cat}} \cdot \Theta$, where Θ is proportional to the cell volume, and $\Gamma_i(t)$ represents independent, temporally uncorrelated Gaussian white noise. Then, for a given value of k_i^{cat} , the first passage time T_{Θ} follows an Inverse Gaussian (IG) distribution (Folks and Chhikara, 1978):

$$\text{IG}\left(x; \mu'_{1/k_i^{\text{cat}}}, \zeta'_{1/k_i^{\text{cat}}}\right) = \begin{cases} \sqrt{\frac{\zeta'_{1/k_i^{\text{cat}}}}{2\pi x^3}} \exp\left(-\frac{1}{2} \frac{\zeta'_{1/k_i^{\text{cat}}} \left(x - \mu'_{1/k_i^{\text{cat}}}\right)^2}{x \mu'^2_{1/k_i^{\text{cat}}}}\right), & x \geq 0, \\ 0, & x < 0, \end{cases} \quad (\text{S142})$$

where $\zeta'_{1/k_i^{\text{cat}}} = \Theta/k_i^{\text{cat}}$ is the shape parameter, and $\mu'_{1/k_i^{\text{cat}}} = 1/k_i^{\text{cat}}$ represents the mean. The variance of this distribution is $\sigma'^2_{1/k_i^{\text{cat}}} \equiv \mu'^3_{1/k_i^{\text{cat}}} / \zeta'_{1/k_i^{\text{cat}}} = 1/\left[\Theta \cdot \left(k_i^{\text{cat}}\right)^2\right]$. Thus, we can obtain the CV:

$$\sigma'_{1/k_i^{\text{cat}}} / \mu'_{1/k_i^{\text{cat}}} = \Theta^{-\frac{1}{2}}, \quad (\text{S143})$$

which is inversely proportional to the square root of cell volume. Evidently, the intrinsic and extrinsic noise make orthogonal contributions to the total noise (Elowitz et al., 2002) (denoted as χ_{tot}):

$$\chi_{\text{tot}}^2 = \chi_{\text{int}}^2 + \chi_{\text{ext}}^2. \quad (\text{S144})$$

In fact, when the CV is small (i.e., $\text{CV} \ll 1$), both the IOG and IG distributions converge into Gaussian distributions (Appendix-fig. 4). In the back-of-the-envelope calculations, we approximate x in all denominator terms of $\text{IOG}(x, \mu, \zeta)$ and $\text{IG}(x, \mu, \zeta)$ as μ (since $\text{CV} \ll 1$). Then, both the IOG and IG distributions can be approximated as follows:

$$\text{IOG}\left(x; \mu_{1/k_i^{\text{cat}}}, \zeta_{1/k_i^{\text{cat}}}\right) \xrightarrow{\text{CV} \ll 1} \mathcal{N}\left(\mu_{1/k_i^{\text{cat}}}, \sigma^2_{1/k_i^{\text{cat}}}\right), \quad (\text{S145})$$

with a variance of $\sigma_{1/k_i^{\text{cat}}}^2 = \mu_{1/k_i^{\text{cat}}}^4 / \zeta_{1/k_i^{\text{cat}}}$, and

$$\text{IG}\left(x; \mu'_{1/k_i^{\text{cat}}}, \zeta'_{1/k_i^{\text{cat}}}\right) \xrightarrow{\text{CV} \ll 1} \mathcal{N}\left(\mu'_{1/k_i^{\text{cat}}}, \sigma_{1/k_i^{\text{cat}}}^2\right), \quad (\text{S146})$$

with a variance of $\sigma_{1/k_i^{\text{cat}}}^2 = \mu_{1/k_i^{\text{cat}}}^3 / \zeta'_{1/k_i^{\text{cat}}}$. Rigorously, we show below that $\text{IG}(x, \mu, \zeta)$ shrinks to be $\mathcal{N}(\mu, \mu^3/\zeta)$ when the CV is small. For the IG distribution, the characteristic function of the variable x is given by (Folks and Chhikara, 1978; Van Kampen, 1992):

$$G(k) = \int_{-\infty}^{\infty} e^{ikx} \cdot \text{IG}(x; \mu, \zeta) dx = \exp\left\{\frac{\zeta}{\mu} \left[1 - \sqrt{1 - \frac{2i\mu^2 k}{\zeta}}\right]\right\}, \quad (\text{S147})$$

and therefore,

$$\text{IG}(x; \mu, \zeta) = \frac{1}{2\pi} \int_{-\infty}^{\infty} e^{-ikx} \cdot G(k) dk. \quad (\text{S148})$$

When the variance $\sigma^2 \equiv \mu^3/\zeta$ is very small, we essentially require $2\mu^2 k/\zeta = 2\sigma^2 k/\mu \ll 1$, and then $\sqrt{1 - \frac{2i\mu^2 k}{\zeta}} \approx 1 - \frac{\mu^2}{\zeta} ki + \frac{\mu^4}{2\zeta^2} k^2$. Thus,

$$\begin{cases} G(k) \approx \exp\left(\mu ki - \frac{\mu^3}{2\zeta} k^2\right), \\ \text{IG}(x; \mu, \zeta) \approx \sqrt{\frac{\zeta}{2\pi\mu^3}} e^{-\frac{\zeta(x-\mu)^2}{2\mu^3}} = \mathcal{N}\left(\mu, \mu^3/\zeta\right). \end{cases} \quad (\text{S149})$$

This leads to:

$$\lim_{\sigma \rightarrow 0} \text{IG}(x; \mu, \zeta) = \mathcal{N}\left(\mu, \mu^3/\zeta\right). \quad (\text{S150})$$

In fact, intrinsic noise does affect the short-term measurement of enzyme catalytic rate and growth rate at the single-cell level. However, its contribution in the long term is averaged out and thus becomes negligible. For simplicity, we approximate $\chi_{\text{tot}} \approx \chi_{\text{ext}}$. Combined with Eqs. S145-S146, it is straightforward to verify that $1/k_i^{\text{cat}}$ shares roughly the same CV as k_i^{cat} :

$$\sigma_{1/k_i^{\text{cat}}} / \mu_{1/k_i^{\text{cat}}} = \sigma_{k_i^{\text{cat}}} / \mu_{k_i^{\text{cat}}}. \quad (\text{S151})$$

For convenience, in the model analysis, we approximate both IOG and IG distributions as Gaussian distributions. Then, all $1/k_i^{\text{cat}}$ are independent, normally distributed random variables following Gaussian distributions:

$$1/k_i^{\text{cat}} \sim \mathcal{N}\left(\mu_{1/k_i^{\text{cat}}}, \sigma_{1/k_i^{\text{cat}}}^2\right). \quad (\text{S152})$$

Using the properties of Gaussian distributions, for a series of constant real numbers γ_i , the summation of $\gamma_i/k_i^{\text{cat}}$, which we define as $\Xi \equiv \sum_{i=1}^n \gamma_i/k_i^{\text{cat}}$, follows a Gaussian distribution (Van Kampen, 1992):

$$\Xi \sim \mathcal{N}\left(\mu_{\Xi}, \sigma_{\Xi}^2\right), \quad (\text{S153})$$

with $\mu_{\Xi} = \sum_{i=1}^n \gamma_i \mu_{1/k_i^{\text{cat}}}$ and $\sigma_{\Xi}^2 = \sum_{i=1}^n \left(\gamma_i \sigma_{1/k_i^{\text{cat}}}\right)^2$. The relation between κ_i and k_i^{cat} is shown in Eq. S12. To optimize cell growth rate, each κ_i of the intermediate nodes satisfies Eq. S20, while κ_A satisfies Eq. S27. Thus, for a given nutrient condition ($[A]$ is fixed), all the ratios $k_i^{\text{cat}}/\kappa_i$ are constants. Combined with Eqs. S139, S145-S146, and S152, the distributions of all κ_i and $1/\kappa_i$ can be approximated as Gaussian distributions:

$$\begin{cases} \kappa_i \sim \mathcal{N}\left(\mu_{\kappa_i}, \sigma_{\kappa_i}^2\right), \\ 1/\kappa_i \sim \mathcal{N}\left(\mu_{1/\kappa_i}, \sigma_{1/\kappa_i}^2\right), \end{cases} \quad (\text{S154})$$

where μ_{κ_i} and μ_{1/κ_i} are the means of κ_i and $1/\kappa_i$, and σ_{κ_i} and σ_{1/κ_i} are their standard deviations. Using the properties of Gaussian distributions, combined with Eq. S31, S32, S36, S42-S43, S145-S146 and S153, ε_r , ε_f , ψ , λ_r , λ_f , $\kappa_A^{(C)}$ and λ_C also roughly follow Gaussian distributions.

Appendix 7.2 Probability density function of the growth rate λ

From Appendix 7.1, we note that λ_r and λ_f (see Eq. S36) roughly follow Gaussian distributions, with

$$\begin{cases} \lambda_r \sim \mathcal{N}\left(\mu_{\lambda_r}, \sigma_{\lambda_r}^2\right), \\ \lambda_f \sim \mathcal{N}\left(\mu_{\lambda_f}, \sigma_{\lambda_f}^2\right), \end{cases} \quad (\text{S155})$$

where $\mu_{\lambda_{r/f}}$ and $\sigma_{\lambda_{r/f}}$ represent the mean and standard deviation, respectively. We further assume that the correlation between λ_r and λ_f is ρ_{rf} . From Eq. S36, we see that the growth rate λ takes the maximum of λ_r and λ_f , i.e.,

$$\lambda = \max(\lambda_r, \lambda_f). \quad (\text{S156})$$

Then, the cumulative distribution function of λ is $P(\lambda \leq x) = \int_{-\infty}^x \int_{-\infty}^x f(x_1, x_2) dx_1 dx_2$, where

$$f(x_1, x_2) = \frac{(1 - \rho_{rf}^2)^{\frac{1}{2}}}{2\pi\sigma_{\lambda_r}\sigma_{\lambda_f}} \exp\left(-\frac{1}{2(1 - \rho_{rf}^2)} \left[\left(\frac{x_1 - \mu_{\lambda_r}}{\sigma_{\lambda_r}}\right)^2 - 2\rho_{rf} \left(\frac{x_1 - \mu_{\lambda_r}}{\sigma_{\lambda_r}}\right) \left(\frac{x_2 - \mu_{\lambda_f}}{\sigma_{\lambda_f}}\right) + \left(\frac{x_2 - \mu_{\lambda_f}}{\sigma_{\lambda_f}}\right)^2 \right]\right).$$

Thus, the probability density function of the growth rate λ is given by:

$$f_\lambda(x) = \frac{1}{2\sqrt{2\pi}\sigma_\lambda} e^{-\frac{1}{2}\left(\frac{x - \mu_\lambda}{\sigma_\lambda}\right)^2} \left[\operatorname{erf}\left(\frac{(x - \mu_{\lambda_f})\sigma_{\lambda_r} - \rho_{rf}\sigma_{\lambda_f}(x - \mu_{\lambda_r})}{\sigma_{\lambda_r}\sigma_{\lambda_f}\sqrt{2(1 - \rho_{rf}^2)}}\right) + 1 \right] + \frac{1}{2\sqrt{2\pi}\sigma_{\lambda_f}} e^{-\frac{1}{2}\left(\frac{x - \mu_{\lambda_f}}{\sigma_{\lambda_f}}\right)^2} \left[\operatorname{erf}\left(\frac{(x - \mu_{\lambda_r})\sigma_{\lambda_f} - \rho_{rf}\sigma_{\lambda_r}(x - \mu_{\lambda_r})}{\sigma_{\lambda_r}\sigma_{\lambda_f}\sqrt{2(1 - \rho_{rf}^2)}}\right) + 1 \right]. \quad (\text{S157})$$

In Appendix-fig. 2B, we show that Eq. S157 quantitatively matches the experimental data for *E. coli* under the relevant conditions.

Appendix 8 Model comparison with experiments on *E. coli*

Appendix 8.1 Flux comparison with experiments on *E. coli*

In Appendix 6.2, we see that the values of $J_f^{(N)}$ and $J_r^{(N)}$ are required to calculate the in vivo enzyme catalytic rates of the intermediate nodes. Here, we use J_{acetate} and $J_{\text{CO}_2,r}$ to represent the stoichiometric fluxes of acetate from the fermentation pathway and CO_2 from the respiration pathway, respectively. Combined with the stoichiometric coefficients of both pathways, we have:

$$\begin{cases} J_{\text{acetate}} = J_f, \\ J_{\text{CO}_2,r} = 3 \cdot J_r. \end{cases} \quad (\text{S158})$$

By further combining with Eqs. S16-S17, we get:

$$\begin{cases} J_f^{(N)} = J_{\text{acetate}} \cdot \frac{m_{\text{carbon}}}{M_{\text{carbon}}} \cdot \left[\sum_i r_i / N_{\text{EP}_i}^{\text{carbon}} \right]^{-1}, \\ J_r^{(N)} = \frac{1}{3} \cdot J_{\text{CO}_2,r} \cdot \frac{m_{\text{carbon}}}{M_{\text{carbon}}} \cdot \left[\sum_i r_i / N_{\text{EP}_i}^{\text{carbon}} \right]^{-1}. \end{cases} \quad (\text{S159})$$

In fact, the values of J_{acetate} and $J_{\text{CO}_2,r}$ scale with the mass of the “big cell”, which increases over time. In experiments, the measurable fluxes are typically expressed in the unit of mM/OD₆₀₀/h (Basan et al., 2015). Thus, we define $J_{\text{acetate}}^{(M)}$ and $J_{\text{CO}_2,r}^{(M)}$ as the fluxes of J_{acetate} and $J_{\text{CO}_2,r}$ (per biomass) in the unit of mM/OD₆₀₀/h, respectively. The superscript “(M)” represents the measurable flux in this unit. For *E. coli*, we use the following biochemical data collected from published literature: 1 OD₆₀₀ roughly corresponds to 6×10^8 cells/mL (Stevenson et al., 2016), the average mass of a cell is 1pg (Milo and Phillips, 2015), the biomass percentage of the cell weight is 30% (Neidhardt et al., 1990), the molar mass of carbon is 12g (Nelson et al., 2008),

$r_{\text{carbon}} = 0.48$ (Neidhardt et al., 1990) and $r_{\text{protein}} = 0.55$ (Neidhardt et al., 1990). Combined with the values of r_i (see Appendix 1.2) and $N_{\text{EP}_i}^{\text{carbon}}$, where $N_{\text{EP}_{a1}}^{\text{carbon}} = 6$, $N_{\text{EP}_{a2}}^{\text{carbon}} = 3$, $N_{\text{EP}_b}^{\text{carbon}} = 3$, $N_{\text{EP}_c}^{\text{carbon}} = 5$, and $N_{\text{EP}_d}^{\text{carbon}} = 4$ (Nelson et al., 2008), we have:

$$\begin{cases} J_f^{(N)} \approx J_{\text{acetate}}^{(M)} / 2, \\ J_r^{(N)} \approx J_{\text{CO}_2, r}^{(M)} / 6. \end{cases} \quad (\text{S160})$$

From Eq. S18, we obtain the values of η_i for each precursor pool: $\eta_{a1} = 0.15$, $\eta_{a2} = 0.30$, $\eta_b = 0.35$, $\eta_c = 0.09$, and $\eta_d = 0.11$. Still, the value of η_E is required to compare the growth rate dependence of fermentation/respiration fluxes between model results and experiments, which we will specify in Appendix 8.2.

Appendix 8.2 Model parameter settings using experimental data of *E. coli*

We have collected biochemical data for *E. coli*, as shown in Appendix-tables 1-2, to set the model parameters. This includes the molecular weight (MW) and in vitro k_{cat} values of the catalytic enzymes, as well as the proteome and flux data used to calculate the in vivo turnover numbers. To reduce measurement noise, we take the average rather than the maximum value of in vivo k_{cat} from calculations using data from four cultures (see Appendix-table 2). Here, we prioritize the use of in vivo k_{cat} wherever applicable unless there is a gap in the in vivo data (see Appendix-table 1).

Note that our models are coarse grained. For example, the flux J_3 shown in Fig. 1B actually corresponds to three different reactions in the metabolic network (see Fig. 1A and Appendix-table 1), which we label as $J_3^{(i)}$ ($i = 1, 2, 3$). For each $J_3^{(i)}$, there are corresponding variables/parameters of $\Phi_3^{(i)}$, $\xi_3^{(i)}$, $\phi_3^{(i)}$, $\kappa_3^{(i)}$ satisfying Eqs. S8, S9 and S12. Evidently, $J_3^{(i)} = J_3$ ($i = 1, 2, 3$), and it is straightforward to derive the following relation between $\kappa_3^{(i)}$ and κ_3 :

$$1/\kappa_3 = \sum_{i=1}^3 1/\kappa_3^{(i)}. \quad (\text{S161})$$

In fact, Eq. S161 can be generalized to determine the values of other κ_i in the coarse-grained models combined with the biochemical data. For the coarse-grained model of Group A carbon source utilization shown in Fig. 1B, we have the values for parameters κ_i ($i = 1, \dots, 6$), and then $\varepsilon_{r/f}(\kappa_A^{(C)}) = 122 \text{ (h}^{-1}\text{)}$. Evidently, $\varepsilon_r(\kappa_{\text{glucose}}^{(\text{ST})}) < \varepsilon_f(\kappa_{\text{glucose}}^{(\text{ST})})$, $\varepsilon_r(\kappa_{\text{lactose}}^{(\text{ST})}) < \varepsilon_f(\kappa_{\text{lactose}}^{(\text{ST})})$, and thus $\varepsilon_r(\kappa_A^{\text{max}}) < \varepsilon_f(\kappa_A^{\text{max}})$. For pyruvate, we have $\varepsilon_{r/f}^{(\text{py})}(\kappa_{\text{py}}^{(C)}) = \varepsilon_{r/f}(\kappa_A^{(C)}) = 122 \text{ (h}^{-1}\text{)}$ (see Eqs. S43 and S101), and it is easy to check that $\varepsilon_r(\kappa_{\text{py}}^{(\text{ST})}) < \varepsilon_f(\kappa_{\text{py}}^{(\text{ST})})$.

For the remaining model parameters, note that we have classified the inactive ribosomal-affiliated proteins into the Q-class, and then $\phi_{\max} = 48\%$ (Scott et al., 2010). The value of κ_i is obtainable from experiments: the translation speed is 20.1aa/s (Scott et al., 2010), with 7336 amino acids per ribosome (Neidhardt, 1996) and $\zeta \approx 1.67$ (Neidhardt, 1996; Scott et al., 2010) (see Appendix 1.1), hence $\kappa_i = 1/610$ (s^{-1}). However, there are insufficient data to determine the values of κ_i ($i = a1, a2, b, c, d$) for the metabolites between the entry point metabolites shown in Fig. 1A to the precursor pools. These processes involves many steps, so these values are expected to be quite large. Here, we combine the contributions of κ_i and η_i ($i = a1, a2, b, c, d$) by defining a composite parameter:

$$\Omega \equiv 1/\kappa_i + \sum_i^{a1,a2,b,c,d} \eta_i/\kappa_i. \quad (\text{S162})$$

We proceed to estimate the values of Ω and φ using experimental data (Basan et al., 2015) for wild-type strains on the $J_{\text{acetate}}^{(M)} - \lambda$ relation (Fig. 1C), and then all the remaining model parameters are set accordingly.

For the case of $w_0 = 0$, where all k_{cat} values follow a Gaussian distribution with an extrinsic noise of 25% CV (which is the general setting we use unless otherwise specified), we have $\varphi = 10.8$ and $\Omega = 1345$ (s). Accordingly, we obtain $\eta_E = 14.78$, $\mu_{\lambda_c} = 0.92$ (h^{-1}), and $\sigma_{\lambda_c} = 0.12\mu_{\lambda_c}$, where the CV of the extrinsic noise for Ω is estimated using the averaged CV of other κ_i . For the translation inhibition effect of Cm, we estimate the values for ι as $\iota_{w_0=0}^{(2\mu\text{m Cm})} = 1.15$, $\iota_{w_0=0}^{(4\mu\text{m Cm})} = 2.33$, and $\iota_{w_0=0}^{(8\mu\text{m Cm})} = 6.25$, where the superscript stands for the concentration of Cm, and the subscript represents the choice of w_0 .

For pyruvate, with the value of η_E , we get $\varphi_{\text{py}} = 14.82$. However, there is still a lack of proteome data to determine the value of κ_9 , which involves many steps in the metabolic network and thus can be considerably large. Here we define another composite parameter, $\Omega'_{\text{Gg}} \equiv (\eta_b + \eta_c)/\kappa_8 + \eta_{a1}/\kappa_9$, and estimate its value as $\Omega'_{\text{Gg}} = 690$ (s) from growth rate data for *E. coli* measured under the relevant nutrient conditions (Basan et al., 2015), where the subscript ‘‘Gg’’ stands for glucogenesis. Then, $\mu_{\lambda_c^{(\text{py})}} = 0.67$ (h^{-1}), and $\sigma_{\lambda_c^{(\text{py})}} = 0.10\mu_{\lambda_c^{(\text{py})}}$, where the same CV of extrinsic noise for Ω applies to Ω'_{Gg} .

For the case of a Group A carbon source mixed with 21 amino acids (21AA, with saturated concentrations), we have $\varphi_{21\text{AA}} = 14.2$. Comparing Eq. S32 with Eq. S112, the parameter Ω should change to $\Omega_{21\text{AA}} \equiv 1/\kappa_i + \eta_{a1}/\kappa_{a1} + \sum_i^{a2,b,c,d} \eta_i/\kappa_i^{(21\text{AA})}$. Obviously, $1/\kappa_i < \Omega_{21\text{AA}} < \Omega$, and we

estimate $\Omega_{21AA} = 1000$ (s) from the growth rate data for *E. coli* measured under the relevant nutrient conditions (Wallden et al., 2016). Then, we have $\mu_{\lambda_c^{(21AA)}} = 1.13$ (h^{-1}), and $\sigma_{\lambda_c^{(21AA)}} = 0.12\mu_{\lambda_c^{(21AA)}}$.

For the case of a Group A carbon source mixed with 7 amino acids (7AA: His, Iso, Leu, Lys, Met, Phe, and Val), similar to the roles of φ_{21AA} and Ω_{21AA} , we define φ_{7AA} and Ω_{7AA} . Using the mass fraction of the 7AA combined with Eq. S18, we have $\varphi_{7AA} = 11.6$. For the value of Ω_{7AA} , evidently, $\Omega_{21AA} < \Omega_{7AA} < \Omega$, and we estimate $\Omega_{7AA} = 1215$ (s) from growth rate data for *E. coli* measured under the relevant culture media (Basan et al., 2015). Then, $\mu_{\lambda_c^{(7AA)}} = 0.98$ (h^{-1}), and $\sigma_{\lambda_c^{(7AA)}} = 0.12\mu_{\lambda_c^{(7AA)}}$.

For the case of $w_0 = 2.5$ (h^{-1}), we have $\varphi = 8.3$, and thus $\eta_E = 12.28$, while other parameters such as Ω , μ_{λ_c} and σ_{λ_c} remain the same as for $w_0 = 0$. Nevertheless, the values for ι under translation inhibition by Cm are influenced by the choice of w_0 , where the values of ι change to $\iota_{w_0=2.5}^{(2\mu\text{m Cm})} = 1.05$, $\iota_{w_0=2.5}^{(4\mu\text{m Cm})} = 2.00$, and $\iota_{w_0=2.5}^{(8\mu\text{m Cm})} = 5.40$.

From Appendix 7.1-7.2, combined with Eq. S114, the distributions of $\lambda_r^{(21AA)}$ and $\lambda_f^{(21AA)}$ can be approximated by Gaussian distributions:

$$\begin{cases} \lambda_r^{(21AA)} \sim \mathcal{N}\left(\mu_{\lambda_r^{(21AA)}}, \sigma_{\lambda_r^{(21AA)}}^2\right), \\ \lambda_f^{(21AA)} \sim \mathcal{N}\left(\mu_{\lambda_f^{(21AA)}}, \sigma_{\lambda_f^{(21AA)}}^2\right), \end{cases} \quad (\text{S163})$$

where $\mu_{\lambda_r^{(21AA)}}$ and $\mu_{\lambda_f^{(21AA)}}$ stand for the mean values, while $\sigma_{\lambda_r^{(21AA)}}$ and $\sigma_{\lambda_f^{(21AA)}}$ represent the standard deviations. For the case of glucose mixed with 21AA (labeled as ‘‘Glucose+21AA’’), the distribution of the growth rate $\lambda_{\text{glucose}}^{(21AA)}$ follows Eq. S157. With $\Omega_{21AA} = 1000$ (s), we have $\mu_{\lambda_{\text{glucose},r}^{(21AA)}} = 1.34$ (h^{-1}), $\mu_{\lambda_{\text{glucose},f}^{(21AA)}} = 1.46$ (h^{-1}) (both definitions follow Eq. S163), and $\rho_{rf} \approx 1.0$ (obtained from numerical results).

For the case of succinate mixed with 21AA (labeled as ‘‘Succinate+21AA’’), the respiration pathway is always more efficient since succinate lies within the TCA cycle. Thus, the cell growth rate (defined as $\lambda_{\text{succinate}}^{(21AA)}$) would take the value of the respiration one and follows a Gaussian distribution:

$$\lambda_{\text{succinate}}^{(21AA)} \sim \mathcal{N}\left(\mu_{\lambda_{\text{succinate}}^{(21AA)}}, \sigma_{\lambda_{\text{succinate}}^{(21AA)}}^2\right). \quad (\text{S164})$$

For the case where acetate is the sole carbon source, the cells exclusively use the respiration pathway, and the growth rate (defined as λ_{acetate}) follows a Gaussian distribution:

$$\lambda_{\text{acetate}} \sim \mathcal{N}\left(\mu_{\lambda_{\text{acetate}}}, \sigma_{\lambda_{\text{acetate}}}^2\right). \quad (\text{S165})$$

Using the measured growth rate data (Wallden et al., 2016), we estimate $\mu_{\lambda_{\text{succinate}}^{(21\text{AA})}} = 0.67 \text{ (h}^{-1}\text{)}$ and $\mu_{\lambda_{\text{acetate}}} = 0.253 \text{ (h}^{-1}\text{)}$. To illustrate the distribution of growth rates $\lambda_{\text{glucose}}^{(21\text{AA})}$, $\lambda_{\text{succinate}}^{(21\text{AA})}$ and λ_{acetate} shown in Appendix-fig. 2B, if no other source of noise existed, extrinsic noise with a CV of 40% would be required for each k_{cat} value. Then, $\sigma_{\lambda_{\text{glucose},r}^{(21\text{AA})}} \approx 0.21\mu_{\lambda_{\text{glucose},r}^{(21\text{AA})}}$, $\sigma_{\lambda_{\text{glucose},f}^{(21\text{AA})}} \approx 0.23\mu_{\lambda_{\text{glucose},f}^{(21\text{AA})}}$, $\sigma_{\lambda_{\text{succinate}}^{(21\text{AA})}} = 0.22\mu_{\lambda_{\text{succinate}}^{(21\text{AA})}}$, and $\sigma_{\lambda_{\text{acetate}}} = 0.22\mu_{\lambda_{\text{acetate}}}$. Allowing for the possibility that intrinsic noise may also play a non-negligible role in the observed single-cell growth rate (which is not a long-term average), we still use extrinsic noise with a CV of 25% for the model results of *E.coli*, except for those shown in Appendix-fig. 2B.

Appendix 9 Explanation of the Crabtree effect in yeast and the Warburg effect in tumors

Our model, along with the analysis presented in Appendix 2, can be extended with modifications to explain the Crabtree effect in yeast and the Warburg effect in tumors. In both cases, the optimization objective remains maximizing the cell growth rate. Consequently, yeast and tumor cells use the most efficient pathway for ATP production at the single-cell level.

For model applications in yeast or tumor cell metabolism, the fermentation flux shifts from acetate secretion to ethanol and lactate secretion, respectively (see Appendix-fig. 5A-B). The respiration and biomass generation pathways remain largely similar to those of *E. coli*, except that the biochemical reactions within the TCA cycle and respiratory chain occur in the mitochondria (see Appendix-fig. 5C-D). This leads to an increased enzyme cost for the respiration pathway due to energy currency exchanges between NADH or FADH₂ and ATP in the mitochondria. The coarse-grained models for Group A carbon source utilization in yeast and mammalian cells are shown in Appendix-fig. 5E-F, where M_3 represents pyruvate. In yeast and mammalian cells, the stoichiometric coefficients for ATP production (i.e., β_i) are identical to each other but differ from those of *E. coli* (see Fig. 1B and Appendix-fig. 5C-D), with $\beta_1 = 5$, $\beta_2 = 1$, $\beta_3 = 5$, $\beta_4 = 7.5$, $\beta_6 = -2.5$, and $\beta_{a1} = 5$ (Nelson et al., 2008). Hence, the stoichiometric coefficients of ATP production per glucose in each pathway are $\beta_r^{(A)} = 32$ and $\beta_f^{(A)} = 2$, respectively, where $\beta_r^{(A)} = \beta_1 + 2(\beta_2 + \beta_3 + \beta_4)$ and $\beta_f^{(A)} = \beta_1 + 2(\beta_2 + \beta_6)$.

The impact of maintenance energy in yeast and tumor cells is significantly higher than that in *E. coli* (Locasale and Cantley, 2010). Therefore, Eq. S25 changes to (see Eq. S59):

$$J_E = r_E \cdot J_{\text{BM}} + w_0 \cdot \frac{M_{\text{carbon}}}{m_0}, \quad (\text{S166})$$

where w_0 is the aforementioned maintenance energy coefficient. Thus, we have (see Eq. S60):

$$J_E^{(N)} = \eta_E \cdot \lambda + w_0. \quad (\text{S167})$$

To account for the protein cost of energy currency exchanges in the mitochondria, we introduce ϕ_{MT} and κ_{MT} to represent the proteomic mass fraction of the enzymes and the effective substrate quality of related metabolites in the mitochondria, respectively. Note that the energy currency exchanges between NADH or FADH₂ and ATP only occur during respiration, as there is no net NADH or FADH₂ generation during fermentation (see Appendix-fig. 5C-D). Combined with Eq. S167, Eq. S25 changes to:

$$\left\{ \begin{array}{l} \phi_A \cdot \kappa_A = \phi_1 \cdot \kappa_1 + \phi_{a1} \cdot \kappa_{a1}, \\ 2\phi_1 \cdot \kappa_1 = \phi_2 \cdot \kappa_2 + \phi_3 \cdot \kappa_3 + \phi_{a2} \cdot \kappa_{a2}, \\ \phi_2 \cdot \kappa_2 = \phi_3 \cdot \kappa_3 + \phi_6 \cdot \kappa_6 + \phi_b \cdot \kappa_b, \\ \phi_5 \cdot \kappa_5 + \phi_4 \cdot \kappa_4 = \phi_3 \cdot \kappa_3 + \phi_d \cdot \kappa_d, \\ \phi_3 \cdot \kappa_3 = \phi_4 \cdot \kappa_4 + \phi_c \cdot \kappa_c, \\ \phi_{a1} \cdot \kappa_{a1} = \eta_{a1} \cdot \lambda, \phi_{a2} \cdot \kappa_{a2} = \eta_{a2} \cdot \lambda, \phi_b \cdot \kappa_b = \eta_b \cdot \lambda, \phi_c \cdot \kappa_c = \eta_c \cdot \lambda, \phi_d \cdot \kappa_d = \eta_d \cdot \lambda, \\ \beta_1 \cdot \phi_1 \cdot \kappa_1 + \beta_2 \cdot \phi_2 \cdot \kappa_2 + \beta_3 \cdot \phi_3 \cdot \kappa_3 + \beta_4 \cdot \phi_4 \cdot \kappa_4 + \beta_6 \cdot \phi_6 \cdot \kappa_6 + \beta_{a1} \cdot \phi_{a1} \cdot \kappa_{a1} = J_E^{(N)}, \\ J_E^{(N)} = \eta_E \cdot \lambda + w_0, \lambda = \phi_R \cdot \kappa_r, J_r^{(N)} = \phi_4 \cdot \kappa_4 = \phi_{\text{MT}} \cdot \kappa_{\text{MT}}, J_f^{(N)} = \phi_6 \cdot \kappa_6, \\ \phi_R + \phi_A + \phi_1 + \phi_2 + \phi_3 + \phi_4 + \phi_5 + \phi_6 + \phi_{\text{MT}} + \phi_{a1} + \phi_{a2} + \phi_b + \phi_c + \phi_d = \phi_{\text{max}}. \end{array} \right. \quad (\text{S168})$$

Here, Eq. S28 still holds, and we have:

$$\left\{ \begin{array}{l} J_r^{(E)} + J_f^{(E)} = \varphi \cdot \lambda + w_0, \\ \frac{J_r^{(E)}}{\varepsilon_r} + \frac{J_f^{(E)}}{\varepsilon_f} = \phi_{\text{max}} - \psi \cdot \lambda, \end{array} \right. \quad (\text{S169})$$

where $J_r^{(E)}$ and $J_f^{(E)}$ follow Eq. S30, and ψ and φ satisfy Eq. S32 and S33, respectively. The expression for ε_f follows Eq. S31. However, the expression for ε_r differs from that in Eq. S31. For yeast and mammalian cells, we have:

$$\left\{ \begin{array}{l} \varepsilon_r = \frac{\beta_r^{(A)}}{1/\kappa_A + 1/\kappa_1 + 2/\kappa_2 + 2/\kappa_3 + 2/\kappa_4 + 2/\kappa_{\text{MT}}}, \\ \varepsilon_f = \frac{\beta_f^{(A)}}{1/\kappa_A + 1/\kappa_1 + 2/\kappa_2 + 2/\kappa_6}. \end{array} \right. \quad (\text{S170})$$

At the single-cell level, from Eq. S169, and similar to Eq. S61-S63, if $\varepsilon_r > \varepsilon_f$, the optimal growth strategy is:

$$\begin{cases} J_f^{(E)} = 0, \\ J_r^{(E)} = \varphi \cdot \lambda + w_0, \end{cases} \quad \varepsilon_r > \varepsilon_f, \quad (\text{S171})$$

while if $\varepsilon_f > \varepsilon_r$, the optimal growth strategy is:

$$\begin{cases} J_f^{(E)} = \varphi \cdot \lambda + w_0, \\ J_r^{(E)} = 0. \end{cases} \quad \varepsilon_r < \varepsilon_f. \quad (\text{S172})$$

In both cases, the growth rate λ reaches its maximum value for a given nutrient condition with fixed κ_A :

$$\lambda(\kappa_A) = \begin{cases} \frac{\phi_{\max} - w_0/\varepsilon_r(\kappa_A)}{\varphi/\varepsilon_r(\kappa_A) + \psi(\kappa_A)} & \varepsilon_r(\kappa_A) > \varepsilon_f(\kappa_A), \\ \frac{\phi_{\max} - w_0/\varepsilon_f(\kappa_A)}{\varphi/\varepsilon_f(\kappa_A) + \psi(\kappa_A)} & \varepsilon_r(\kappa_A) < \varepsilon_f(\kappa_A). \end{cases} \quad (\text{S173})$$

From Eq. S170, when κ_A is very small such that $\kappa_A \rightarrow 0$, it is evident that for yeast and mammalian cells, we still have:

$$\begin{cases} \varepsilon_r(\kappa_A \rightarrow 0) \approx \beta_r^{(A)} \cdot \kappa_A, \\ \varepsilon_f(\kappa_A \rightarrow 0) \approx \beta_f^{(A)} \cdot \kappa_A. \end{cases} \quad (\text{S174})$$

Thus,

$$\varepsilon_r(\kappa_A \rightarrow 0) > \varepsilon_f(\kappa_A \rightarrow 0), \quad (\text{S175})$$

since $\beta_r^{(A)} \gg \beta_f^{(A)}$ still holds. Then, as long as $\varepsilon_r(\kappa_A^{\max}) < \varepsilon_f(\kappa_A^{\max})$, there exists a critical switching point for κ_A (denoted as $\kappa_A^{(C)}$, see Eq. S41), below which respiration is more efficient, while above $\kappa_A^{(C)}$, fermentation becomes more efficient in ATP production per proteome. Combined with Eq. S170, we have:

$$\kappa_A^{(C)} = \frac{\beta_r^{(A)} - \beta_f^{(A)}}{\beta_f^{(A)}(1/\kappa_1 + 2/\kappa_2 + 2/\kappa_3 + 2/\kappa_4 + 2/\kappa_{\text{MT}}) - \beta_r^{(A)}(1/\kappa_1 + 2/\kappa_2 + 2/\kappa_6)}. \quad (\text{S176})$$

Accordingly, we obtain the expressions for $\varepsilon_r(\kappa_A^{(C)})$, $\varepsilon_f(\kappa_A^{(C)})$ and λ_C (i.e., $\lambda(\kappa_A^{(C)})$):

$$\left\{ \begin{array}{l} \varepsilon_r(\kappa_A^{(C)}) = \varepsilon_f(\kappa_A^{(C)}) = \frac{\beta_r^{(A)} - \beta_f^{(A)}}{2(1/\kappa_3 + 1/\kappa_4 + 1/\kappa_{MT} - 1/\kappa_6)}, \\ \lambda_c = \frac{\phi_{\max} - w_0/\varepsilon_{r/f}(\kappa_A^{(C)})}{\varphi/\varepsilon_{r/f}(\kappa_A^{(C)}) + \psi(\kappa_A^{(C)})}, \end{array} \right. \quad (\text{S177})$$

Consequently, yeast and tumor cells would preferentially use respiration under starvation conditions (where $\varepsilon_r > \varepsilon_f$), yet switch to aerobic glycolysis when nutrients are abundant (where $\varepsilon_r < \varepsilon_f$) for optimal cell growth. This qualitatively illustrates the Crabtree effect in yeast and the Warburg effect in tumors.

At the cell population level, cell heterogeneity resulting from intrinsic and extrinsic noise causes the turnover numbers (i.e., k_{cat}) of enzymes and the critical growth rates at the transition point (λ_c) to follow distributions, which we assume to be Gaussian (see Eq. S45, Appendices 2.3 and 7.1). Due to the higher level of heterogeneity observed in tumor cells (Duraj et al., 2021; Hanahan and Weinberg, 2011; Hensley et al., 2016) and yeast (Bagamery et al., 2020) compared to *E. coli*, the extent of noise—and thus the CVs of k_{cat} and λ_c —in yeast and tumor cells are expected to be larger than those in *E. coli*. The growth rate dependence of the normalized energy fluxes is as follows:

$$\left\{ \begin{array}{l} J_f^{(E)}(\lambda) = \frac{1}{2}(\varphi \cdot \lambda + w_0) \cdot \left[\text{erf}\left(\frac{\lambda - \mu_{\lambda_c}}{\sqrt{2}\sigma_{\lambda_c}}\right) + 1 \right], \\ J_r^{(E)}(\lambda) = \frac{1}{2}(\varphi \cdot \lambda + w_0) \cdot \left[1 - \text{erf}\left(\frac{\lambda - \mu_{\lambda_c}}{\sqrt{2}\sigma_{\lambda_c}}\right) \right], \end{array} \right. \quad (\text{S178})$$

where μ_{λ_c} and σ_{λ_c} are the mean and standard deviation of λ_c , respectively, similar to the case of *E. coli*. Therefore, the growth rate dependence of the normalized fluxes is:

$$\left\{ \begin{array}{l} J_f^{(N)}(\lambda) = \frac{\varphi \cdot \lambda + w_0}{\beta_f^{(A)}} \cdot \left[\text{erf}\left(\frac{\lambda - \mu_{\lambda_c}}{\sqrt{2}\sigma_{\lambda_c}}\right) + 1 \right], \\ J_r^{(N)}(\lambda) = \frac{\varphi \cdot \lambda + w_0}{\beta_r^{(A)}} \cdot \left[1 - \text{erf}\left(\frac{\lambda - \mu_{\lambda_c}}{\sqrt{2}\sigma_{\lambda_c}}\right) \right]. \end{array} \right. \quad (\text{S179})$$

Combined with Eq. S160, Eq. S179 can be compared to experimental results, although in practice, it is difficult to tune the growth rate of tumor cells in vivo in experiments.

Recently, Shen et al. (Shen et al., 2024) reported that in many yeast and tumor cells, the measured proteome efficiencies in respiration at the cell population level are higher than the corresponding proteome efficiencies in fermentation, even though aerobic glycolysis fermentation fluxes still occur. This finding apparently contradicts prevalent explanations (Basan et al., 2015; Chen and Nielsen, 2019), which assert that overflow metabolism originates from the proteome efficiency in fermentation always being higher than in respiration.

Our model can resolve the puzzle above based on two important features: First, our model predicts that as long as ATP generation per glucose in respiration is higher than in fermentation (i.e., $\beta_r^{(A)} > \beta_f^{(A)}$), which definitely holds true for all organisms, the proteome efficiency in respiration is higher than that in fermentation when the nutrient quality κ_A is low (see Eqs. S37-S38 and S174-S175). Second, and importantly, due to cell heterogeneity at the population level, a subset of cells exhibiting greater proteome efficiency in fermentation compared to respiration could exist, even if the proteome efficiency at the cell population level in respiration is higher than in fermentation.

To facilitate comparison between our model and the experiments of Shen et al. (Shen et al., 2024), we define Pr_f as the proportion of ATP generated from fermentation, and $\bar{\Delta}$ as the proteome efficiency difference between respiration and fermentation, with

$$\text{Pr}_f \equiv \frac{J_f^{(E)}}{J_f^{(E)} + J_r^{(E)}}, \quad (\text{S180})$$

and

$$\bar{\Delta} \equiv 1/\varepsilon_r - 1/\varepsilon_f. \quad (\text{S181})$$

At the cell population level, ε_r , ε_f , $1/\varepsilon_r$ and $1/\varepsilon_f$ roughly follow Gaussian distributions (see Appendix 7.1 and Eq. S170), with

$$\begin{cases} \varepsilon_r \sim \mathcal{N}(\mu_{\varepsilon_r}, \sigma_{\varepsilon_r}^2), \varepsilon_f \sim \mathcal{N}(\mu_{\varepsilon_f}, \sigma_{\varepsilon_f}^2), \\ 1/\varepsilon_r \sim \mathcal{N}(\mu_{1/\varepsilon_r}, \sigma_{1/\varepsilon_r}^2), 1/\varepsilon_f \sim \mathcal{N}(\mu_{1/\varepsilon_f}, \sigma_{1/\varepsilon_f}^2). \end{cases} \quad (\text{S182})$$

Here, σ_{ε_r} , σ_{ε_f} , σ_{1/ε_r} , σ_{1/ε_f} , and μ_{ε_r} , μ_{ε_f} , μ_{1/ε_r} , μ_{1/ε_f} are the standard deviations and mean values of ε_r , ε_f , $1/\varepsilon_r$ and $1/\varepsilon_f$, respectively. Thus,

$$\begin{cases} \mu_{\varepsilon_r} = \langle \varepsilon_r \rangle, \\ \mu_{\varepsilon_f} = \langle \varepsilon_f \rangle, \end{cases} \quad (\text{S183})$$

where the angle bracket “ $\langle \rangle$ ” represents the average over the cell population, and $\langle \varepsilon_r \rangle$ and $\langle \varepsilon_f \rangle$ are the population-averaged values of ε_r and ε_f , respectively, which are both measurable in experiments. From the derivations shown in Appendix 7.1, we approximately have

$$\begin{cases} \mu_{1/\varepsilon_r} = 1/\mu_{\varepsilon_r} = 1/\langle \varepsilon_r \rangle, \\ \mu_{1/\varepsilon_f} = 1/\mu_{\varepsilon_f} = 1/\langle \varepsilon_f \rangle. \end{cases} \quad (\text{S184})$$

Here, we use χ_{ε_r} , χ_{ε_f} , χ_{1/ε_r} and χ_{1/ε_f} to represent the CVs of ε_r , ε_f , $1/\varepsilon_r$ and $1/\varepsilon_f$, respectively, with

$$\begin{cases} \chi_{\varepsilon_r} = \sigma_{\varepsilon_r} / \mu_{\varepsilon_r}, \chi_{\varepsilon_f} = \sigma_{\varepsilon_f} / \mu_{\varepsilon_f}, \\ \chi_{1/\varepsilon_r} = \sigma_{1/\varepsilon_r} / \mu_{1/\varepsilon_r}, \chi_{1/\varepsilon_f} = \sigma_{1/\varepsilon_f} / \mu_{1/\varepsilon_f}. \end{cases} \quad (\text{S185})$$

Similar to Eq. S151, the CVs of $1/\varepsilon_r$ and $1/\varepsilon_f$ are roughly equal to those of ε_r and ε_f , respectively. Thus,

$$\begin{cases} \chi_{1/\varepsilon_r} \approx \chi_{\varepsilon_r}, \\ \chi_{1/\varepsilon_f} \approx \chi_{\varepsilon_f}. \end{cases} \quad (\text{S186})$$

Combining Eqs. S181 and S182, and using the properties of Gaussian distributions, $\bar{\Delta}$ follows a Gaussian distribution:

$$\bar{\Delta} \sim \mathcal{N}(\mu_{\bar{\Delta}}, \sigma_{\bar{\Delta}}^2), \quad (\text{S187})$$

where $\mu_{\bar{\Delta}}$ and $\sigma_{\bar{\Delta}}$ are the mean and standard deviation of $\bar{\Delta}$, respectively. Evidently, we have

$$\begin{cases} \mu_{\bar{\Delta}} = \mu_{1/\varepsilon_r} - \mu_{1/\varepsilon_f}, \\ \sigma_{\bar{\Delta}}^2 = \sigma_{1/\varepsilon_r}^2 + \sigma_{1/\varepsilon_f}^2. \end{cases} \quad (\text{S188})$$

Then, we proceed to calculate the relation between Pr_f and $\bar{\Delta}$ using Eq. S187, and hence we obtain:

$$\text{Pr}_f = \int_0^{+\infty} \frac{1}{\sigma_{\bar{\Delta}} \sqrt{2\pi}} e^{-\frac{1}{2} \left(\frac{x - \mu_{\bar{\Delta}}}{\sigma_{\bar{\Delta}}} \right)^2} dx = \frac{1}{2} \left[\text{erf} \left(\frac{\mu_{\bar{\Delta}}}{\sqrt{2}\sigma_{\bar{\Delta}}} \right) + 1 \right]. \quad (\text{S189})$$

Combining Eqs. S180, S183-S185, and S188-S189, we have:

$$\frac{J_f^{(E)}}{J_f^{(E)} + J_r^{(E)}} = \frac{1}{2} \left[\operatorname{erf} \left(\frac{1 - \langle \varepsilon_r \rangle / \langle \varepsilon_f \rangle}{\sqrt{2} \cdot \sqrt{\chi_{\varepsilon_r}^2 + \chi_{\varepsilon_f}^2 \cdot (\langle \varepsilon_r \rangle / \langle \varepsilon_f \rangle)^2}} \right) + 1 \right]. \quad (\text{S190})$$

Note that the normalized energy fluxes $J_r^{(E)}$ and $J_f^{(E)}$ are proportional to the measured ATP fluxes generated in respiration and fermentation, respectively. Hence, Eq. S190 can be directly compared to experimental data. For yeast and tumor cells, due to a higher level of heterogeneity, the CVs of ε_r and ε_f , i.e., χ_{ε_r} and χ_{ε_f} , could be significantly higher than the corresponding values in *E. coli*, though their exact values are unknown. Consequently, we plot theoretical results with the values of χ_{ε_r} and χ_{ε_f} chosen as 0.25, 0.40, and 0.58 to compare with the experimental data for yeast and in vivo mouse tumors (Bartman et al., 2023; Shen et al., 2024). In Fig. 5A-B, we observe that the theoretical results using $\chi_{\varepsilon_r} = \chi_{\varepsilon_f} = 0.58$ agree well with the experimental data (Bartman et al., 2023; Shen et al., 2024), both on a log scale and linear scale. This demonstrates that our model has the potential to quantitatively illustrate the Crabtree effect in yeast and the Warburg effect in tumors.

Appendix 10 Notes on the application of reference data

Data calibration: Throughout our manuscript, we use experimental data from the original references, except for two calibrations. The first calibration is noted in the footnote of Appendix-table 2. With this calibration, the $J_{\text{acetate}}^{(M)} - \lambda$ data for *E. coli* (Basan et al., 2015) in Appendix-table 2 align with the curve shown in Fig. 1C, which includes experimental data for *E. coli* from other sources. The second calibration applies to the data shown in Figs. 3F and 1C (chemostat data for *E. coli*). The unit in the original reference (Holms, 1996) is mmol/(dry mass)g/h. To convert this to the unit mM/OD₆₀₀/h, used in our text, the conversion factor should be 0.18. Here, we deduce that only 60% of the measured dry biomass in centrifuged material is effective when calibrating with other experimental results. Therefore, there is a calibration factor of 0.6, and the conversion factor changes to 0.3.

Data from the inducible strains: Some of the experimental data in the original references (Basan et al., 2015; Hui et al., 2015) were obtained using *E. coli* strains with titratable systems (e.g., titratable ptsG, LacY). The $J_{\text{acetate}}^{(M)} - \lambda$ relation of these inducible strains generally aligns with the same curve as that of wild-type *E. coli* (Fig. 1C). Since evolutionary treatment was not applied to the inducible strains, we approximate titration perturbation as a technique that mimics culturing the strains in a less efficient Group A carbon source.

Experimental data sources: The batch culture data for *E. coli* shown in Fig. 1C (labeled as minimum/rich media or inducible strains) and Appendix-fig. 2C were taken from the source data of the reference's figure 1 (Basan et al., 2015). The chemostat data for *E. coli* shown in Fig. 1C were taken from the reference's table 7 (Holms, 1996). The data for *E. coli* shown in Fig. 1D

were taken from the reference's extended data figure 3a (Basan et al., 2015), with the calibration specified in the footnote to Appendix-table 2.

The data for *E. coli* shown in Fig. 2A were adopted from the reference's extended data figure 4a-b (Basan et al., 2015). The data for *E. coli* shown in Fig. 2B were taken from the source data of the reference's figure 2a (Basan et al., 2015). The data for *E. coli* shown in Fig. 2C were taken from the source data of the reference's figure 3a (Basan et al., 2015). The data for *E. coli* shown in Fig. 3A-B were taken from the source data of the reference's figure 3d (Basan et al., 2015).

The data for *E. coli* shown in Fig. 3C-D and Appendix-fig. 2D-E were taken from the source data of the reference's figure 3c (Basan et al., 2015). The data for *E. coli* shown in Fig. 3F were taken from the reference's table 7 (Holms, 1996), with a calibration factor specified in the above paragraph ("Data calibration").

The data for *E. coli* shown in Fig. 4A-B and Appendix-fig. 3A-D were taken from the reference's table S2 with the label "C-lim" (Hui et al., 2015). We excluded the reference's data with $\lambda = 0.45205 \text{ h}^{-1}$ as there are other unconsidered factors involved during slow growth (Dai et al., 2017) (for $\lambda < 0.5 \text{ h}^{-1}$), and we suspect that unknown calibration factors may exist. The data for *E. coli* shown in Fig. 4C-D and Appendix-fig. 3E-N were adopted from the reference's extended data figure 6-7 (Basan et al., 2015).

The batch culture data for yeast shown in Fig. 5 were derived from the source data of the reference's extended figure 4c-d (Shen et al., 2024). The chemostat data for yeast shown in Fig. 5 were derived from the source data of the reference's figure 3d-e (Shen et al., 2024), where glucose is the limiting nutrient. We excluded the reference's data for *I. orientalis* under condition C2, where the ATP flux was abnormally small. The mouse tumor in vivo data shown in Fig. 5 were derived from the source data of the reference's figure 4e-g (Shen et al., 2024), which were originally reported by Bartman et al. (Bartman et al., 2023), the same research group as Shen et al. (Shen et al., 2024). We did not include the cancer cell line data shown in figure 4a-c of Shen et al. (Shen et al., 2024) since it appears that the proteomic data and flux data were obtained from two different references with inconsistent culturing conditions.

The gene names of *E. coli* depicted in Appendix-fig. 1B were identified using the KEGG database. The data for *E. coli* shown in Appendix-fig. 2G were drawn from Appendix-table 1, which includes the original references themselves. The flux data for *E. coli* presented in Appendix-table 2 were obtained from the reference's extended data figure 3a (Basan et al., 2015), with the calibration specified in the footnote. The proteome data for *E. coli* shown in Appendix-table 2 were taken from the reference's supplementary Table N5 (Basan et al., 2015).

Appendix Tables

Appendix-table 1. Molecular weight (MW) and in vivo/ in vitro k_{cat} data for *E. coli*.

No.*	Reaction	Enzyme	Gene name	EC	MW (kDa)	In vitro k_{cat} (s^{-1})	References	In vivo† k_{cat} (s^{-1})	Chosen k_{cat} (s^{-1})
J_1	Glucose-6P \leftrightarrow Fructose-6P	Glucose-6-phosphate isomerase	pgi	EC:5.3.1.9	1.2×10^2	2.6×10^2	PMID: 7004378; DOI:10.1016/j.ijms.2004.09.017	8.7×10^2	8.7×10^2
	Fructose-6P \rightarrow Fructose-1,6P	Phosphofructokinase	pfkA‡	EC:2.7.1.11	1.4×10^2	4.4×10^2	PMID: 6218375; 70226	1.7×10^3	1.7×10^3
	Fructose-1,6P \leftrightarrow Glyceraldehyde 3-phosphate+Dihydroxy acetone phosphate	Fructose-bisphosphate aldolase	fbaA‡	EC:4.1.2.13	7.8×10	1.4×10	PMID: 8939754; 15531627	1.6×10^2	1.6×10^2
	Dihydroxyacetone phosphate \leftrightarrow Glyceraldehyde 3-phosphate	Triosephosphate Isomerase	tpiA	EC:5.3.1.1	5.4×10	4.3×10^2	PMID: 3887397; 6092857	2.7×10^2	2.7×10^2
	Glyceraldehyde 3-phosphate \leftrightarrow 1,3-Bisphosphoglycerate	Glyceraldehyde-3-phosphate dehydrogenase	gapA	EC:1.2.1.12	1.4×10^2	9.5×10	PMID: 4932978; 2200929	1.5×10^2	1.5×10^2
	1,3-Bisphosphoglycerate \leftrightarrow 3-Phosphoglycerate	Phosphoglycerate kinase	pgk	EC:2.7.2.3	4.4×10	3.5×10^2	PMID: 367367; 166274	1.9×10^2	1.9×10^2
	3-Phosphoglycerate \leftrightarrow 2-Phosphoglycerate	Phosphoglycerate mutase	gpmA‡	EC:5.4.2.11	4.9×10	3.3×10^2	PMID: 10437801	4.5×10^2	4.5×10^2
	2-Phosphoglycerate \leftrightarrow Phosphoenolpyruvate	Enolase	eno	EC:4.2.1.11	9.0×10	2.2×10^2	PMID: 1094232; 4942326	1.7×10^2	1.7×10^2
J_2	Phosphoenolpyruvate \rightarrow Pyruvate	Pyruvate kinase	pykF‡	EC:2.7.1.40	2.4×10^2	5.0×10^2	PMID: 6759852	1.6×10^3	1.6×10^3
	Pyruvate \rightarrow Acetyl-CoA	Pyruvate dehydrogenase	aceE‡	EC:1.2.4.1	1.0×10^2	1.2×10^2	PMID: 23088422	3.4×10^2	3.4×10^2
J_3	Oxaloacetate +Acetyl-CoA \rightarrow Citrate	Citrate synthase	gltA	EC:2.3.3.1	9.7×10	2.4×10^2	PMID: 4900996; 23954305	7.1×10	7.1×10
	Citrate \leftrightarrow Isocitrate	Aconitate hydratase	acnB‡	EC:4.2.1.3	9.4×10	7.0×10	PMID:15963579; 12473114	6.3×10	6.3×10
	Isocitrate \rightarrow α -Ketoglutarate	Isocitrate dehydrogenase	icd	EC:1.1.1.42	9.5×10	2.0×10^2	PMID: 8141; 36923; 2200929	3.3×10	3.3×10
J_4	α -Ketoglutarate \rightarrow Succinyl-CoA	α -Ketoglutarate dehydrogenase complex E1 component	suc A suc B‡	EC:1.2.4.2, EC:2.3.1.61	1.9×10^2	1.5×10^2	PMID: 6380583; 4588679	1.3×10^2	1.3×10^2
	Succinyl-CoA \leftrightarrow Succinate	Succinyl-CoA synthetase	suc C suc D	EC:6.2.1.5	1.6×10^2	9.1×10	PMID: 5338130	1.0×10^2	1.0×10^2
	Succinate \rightarrow Fumarate	Succinate dehydrogenase	sdh A sdh B‡	EC:1.3.5.1	1.0×10^2	1.1×10^2	PMID: 4334990; 16484232	1.1×10^2	1.1×10^2
	Fumarate \leftrightarrow Malate	Fumarase	fumA‡	EC:4.2.1.2	2.0×10^2	1.2×10^3	PMID: 3282546; 12021453	4.9×10^2	4.9×10^2
	Malate \leftrightarrow Oxaloacetate	Malate dehydrogenase	mdh	EC:1.1.1.37	6.1×10	5.5×10^2	doi:10.1016/0076-6879(69)13029-3	6.6×10	6.6×10
J_5	Phosphoenolpyruvate \rightarrow Oxaloacetate	Phosphoenolpyruvate carboxylase	ppc	EC:4.1.1.31	4.0×10^2	1.5×10^2	PMID: 9927652; 4932977	/	1.5×10^2
J_6	Acetyl-CoA \leftrightarrow Acetyl phosphate	Phosphate acetyltransferase	pta	EC:2.3.1.8	7.7×10	3.0×10	PMID:20236319	3.7×10^2	3.7×10^2
	Acetyl phosphate \leftrightarrow Acetate	Acetate kinase	ackA	EC:2.7.2.1	4.3×10	3.6×10^3	EcoCyc: EG10027; PMID: 24801996	3.3×10^2	3.3×10^2
	Acetate (intracellular) \leftrightarrow Acetate (extracellular)	Acetate transporter	actP	/	2×10	4.7×10^2	PMID: 31405984 (Estimated)	/	4.7×10^2
J_7	Pyruvate \rightarrow Phosphoenolpyruvate	Pyruvate, water dikinase	ppsA	EC:2.7.9.2	2.5×10^2	3.5×10	PMID: 4319237	/	3.5×10

J_{Λ}	Glucose-6P (extracellular) → Glucose-6P (intracellular)	Glucose-6- phosphate transporter	UhpT	/	5×10	2×10^2	PMID: 3283129; 2197272; 20018695 (Estimated)	/	2×10^2
	Glucose (extracellular) → Glucose-6P	Glucose-specific PTS enzyme	ptsG	EC: 2.7.1.199	5×10	1×10^2	PMID: 9575173; 20018695; 12146972	/	1×10^2
	Lactose (extracellular) → Lactose (intracellular)	Lactose transporter	lacY	/	4.6×10	6×10	PMID: 6444453; 20018695	/	6×10
	Lactose → Glucose + Galactose	β -galactosidase	lacZ	EC:3.2.1.23	4.6×10^2	6.4×10^2	PMID: 8008071; 23011886 (Estimated)	/	6.4×10^2
J_{py}	Pyruvate (extracellular) → Pyruvate (intracellular)	Pyruvate transporter	btsT CstA	/	8×10	6×10	PMID:20018695; 33260635; EcoCyc: G7942; EG10167 (Estimated)	/	6×10

* The classification of J_i follows the coarse-grained models shown in Figs. 1B and 3E.

† In vivo k_{cat} values were obtained using the experimental data shown in Appendix-table 2, combined with Eqs. S134-S135.

‡ See Appendix-fig. 1B for additional genes that may play a secondary role.

Appendix-table 2. Proteome and flux data (Basan et al., 2015) used to calculate the in vivo k_{cat} of *E. coli*.

	Culture 1	Culture 2	Culture 3	Culture 4
Growth rate λ (h^{-1}) *	0.82	0.87	0.97	1.03
J_{acetate} ($\text{mM OD}_{600}^{-1} \text{h}^{-1}$) †	0.39	1.18	2.68	2.84
$J_{\text{CO}_2, r}$ ($\text{mM OD}_{600}^{-1} \text{h}^{-1}$) †	7.44	6.05	4.30	3.04
Gene name	Proteomic mass fractions obtained using absolute abundance (ϕ_i)			
pgi	0.09%	0.09%	0.10%	0.11%
pfkA	0.06%	0.06%	0.06%	0.06%
fbaA	0.32%	0.35%	0.35%	0.39%
tpiA	0.12%	0.15%	0.13%	0.18%
gapA	1.19%	1.29%	1.33%	1.47%
pgk	0.30%	0.31%	0.32%	0.36%
gpmA	0.15%	0.15%	0.15%	0.16%
eno	0.63%	0.70%	0.75%	0.83%
pykF	0.15%	0.15%	0.18%	0.21%
aceE	0.30%	0.32%	0.34%	0.41%
gltA	0.88%	0.80%	0.61%	0.48%
acnB	0.92%	0.84%	0.66%	0.57%
icd	1.55%	1.55%	1.31%	1.39%
suc A suc B	0.71%	0.75%	0.64%	0.55%
suc C suc D	0.88%	0.84%	0.66%	0.52%
sdh A sdh B	0.49%	0.45%	0.42%	0.35%
fumA	0.24%	0.21%	0.17%	0.13%
mdh	0.45%	0.45%	0.41%	0.39%
pta	0.10%	0.10%	0.10%	0.10%
ackA	0.06%	0.07%	0.06%	0.06%

* For calibration purposes, a factor of 1.03/0.97 was multiplied by the reference data (Basan et al., 2015)‡.

† For calibration purposes, a factor of 2.84/3.24 was multiplied by the reference data (Basan et al., 2015)‡.

‡ Here, (1.03, 2.84) and (0.97, 3.24) are both the data points for (λ (h^{-1}), J_{acetate} ($\text{mM OD}_{600}^{-1} \text{h}^{-1}$)) for *E. coli* strain NCM3722 cultured with lactose in the same reference (Basan et al., 2015). The former is specified in the source data of the reference's figure 1 (Basan et al., 2015), while the latter is recorded in the reference's extended data figure 3a (Basan et al., 2015). With the calibrations above, the data for the $J_{\text{acetate}}^{(M)} - \lambda$ relation shown here align with the curve depicted in Fig. 1C.

Appendix-table 3. Illustrations of symbols in this manuscript.

Symbols	Illustrations / Definitions	Model variable / parameter settings for <i>E.coli</i> *
A (in the figures)	A Group A carbon source joining the metabolic network from the upper part of glycolysis.	NA**
M_i (in the figures)	A metabolite in the metabolic network that serve as intermediate node.	NA
J_i (in the figures)	The stoichiometric flux delivering carbon flux, an extensive variable†; see Eq. S7.	see Eqs. S7-S8.
r_i (in the figures)	The mass fraction of carbon flux drawn from a precursor pool.	$r_{a1}=24\%$, $r_{a2}=24\%$, $r_b=28\%$, $r_c=12\%$, $r_d=12\%$ (Nelson et al., 2008).
λ	Growth rate of the cell population; see Eq. S36 for the optimal model solution.	see Eqs. S4 and S36.
J_r, J_f	J_r and J_f are stoichiometric fluxes of respiration and fermentation, extensive variables.	$J_r=J_4$; $J_f=J_6$ (see Eq. S22)
m_0	The weighted average carbon mass of metabolite molecules at the entrance of precursor pools.	See Eq. S17.
M_{carbon}	The carbon mass of the cell population, an extensive variable.	NA
$M_{protein}$	The protein mass of the cell population; an extensive variable.	NA
$M_Q^{(P)}, M_R^{(P)}, M_C^{(P)}$	The mass of Q-class, R-class, or C-class proteome.	See Eq. S2.
f_Q, f_R, f_C	The ribosome allocation fraction for protein synthesis of Q-class, R-class, or C-class.	$f_Q=\phi_Q$.
m_{AA}	The average molecular weight of amino acids.	A reducible parameter for the results.
k_T	Translation speed of ribosomes.	$k_T=20.1$ aa/s (Scott et al., 2010).
ϕ_Q, ϕ_R, ϕ_C	The mass fraction of Q-class, R-class, or C-class proteome; see Appendix 1.1.	$\phi_Q=52\%$ (Scott et al., 2010).
ϕ_{max}	The maximum proteomic mass fraction of proteome allocation for fermentation, respiration, and biomass generation, with $\phi_{max} \equiv 1 - \phi_Q$.	$\phi_{max}=48\%$ (Scott et al., 2010).
m_R	The protein mass of a single ribosome.	$m_R=7336 m_{AA}$ (Neidhardt et al., 1990).
V_{cell}	The cell volume of the cell population (the “big cell”); an extensive variable.	NA
$N_R, M_{rp}^{(P)}$	The number or the total protein mass of ribosomes in the big cell; extensive variables.	NA
ζ	The ratio of the mass of R-class proteome to the protein mass of ribosomes: $\zeta \equiv M_R^{(P)} / M_{rp}^{(P)}$.	$\zeta=1.67$ (Scott et al., 2010).
$[E_i], [S_i]$	The concentration of enzyme E_i or substrate S_i ; intensive variables.	NA
a_i, d_i, b_i, c_i	a_i and d_i are reaction parameters; b_i and c_i are stoichiometric coefficients. See Appendix 1.3.	NA
K_i	The Michaelis constant, defined as $K_i=(d_i+k_i^{cat})/a_i$.	Obtainable from Bennett et al. (Bennett et al., 2009), yet unused in practice since $[S_i] > K_i$ (see Appendix 1.5).
v_i	The reaction rate per volume of a biochemical reaction catalyzed by E_i ; an intensive variable.	See Eq. S6.
N_{E_i}, M_{E_i}	The copy number or the total weight enzyme E_i in the cell population; extensive variables.	$N_{E_i} = V_{cell} \cdot [E_i]$; $M_{E_i} = N_{E_i} \cdot m_{E_i}$.
m_{carbon}	The mass of a carbon atom.	$m_{carbon} = \frac{12}{N_{Avogadro}}$ g, where g represents gram and $N_{Avogadro}$ is the Avogadro constant.
Φ_i	The enzyme cost of all E_i molecules in the cell population; an extensive variable.	$\Phi_i \equiv N_{E_i} \cdot n_{E_i}$.
ξ_i	ξ_i is defined such that $\xi_i = J_i / \Phi_i$.	$\xi_i \equiv \frac{k_i^{cat} \cdot [S_i]}{n_{E_i} \cdot [S_i] + K_i}$.
$J_i^{(N)}$	The normalized flux, i.e., flux per unit of biomass; an intensive variable†.	$J_i^{(N)} \equiv J_i \cdot m_0 / M_{carbon}$ see Eqs. S15-S16.
$J_r^{(N)}, J_f^{(N)}$	$J_r^{(N)}$ and $J_f^{(N)}$ are the normalized fluxes of respiration and fermentation, intensive variables.	$J_r^{(N)}=J_4^{(N)}$; $J_f^{(N)}=J_6^{(N)}$.
$N_{EP_i}^{carbon}$	The number of carbon atoms in the entry point metabolite molecule of Precursor Pool i .	$N_{EP_{a1}}^{carbon}=6$, $N_{EP_{a2}}^{carbon}=3$, $N_{EP_b}^{carbon}=3$, $N_{EP_c}^{carbon}=5$, $N_{EP_d}^{carbon}=4$ (Nelson et al., 2008).
k_{cat}, k_i^{cat}	The turnover number of a catalytic enzyme.	See Appendix-table 1.
m_{E_i}, n_{E_i}	m_{E_i} and n_{E_i} are the molecular weight and the enzyme cost of an E_i molecule, respectively.	See Appendix-table 1.
$r_{carbon}, r_{protein}$	r_{carbon} and $r_{protein}$ are the mass fractions of all carbon and protein within a cell, respectively.	$r_{protein}=0.55$; $r_{carbon}=0.48$ (Neidhardt et al., 1990).
κ_i	Substrate quality of a metabolite in a biochemical reaction; see Eq. S12 and S20.	Calculated from the values of k_i^{cat} , m_{E_i} , m_0 , $r_{protein}$, r_{carbon} .
κ_A	Substrate quality of a Group A carbon source; see Eq. S27.	Calculated from the values of k_A^{cat} , m_{E_A} , m_0 , $r_{protein}$, r_{carbon} , K_A and the concentration of the Group A carbon source $[A]$.
ϕ_i	The proteomic mass fraction of enzyme E_i : $\phi_i \equiv M_{E_i} / M_{protein}$; an intensive variable.	See Eq. S9.
η_i	The fraction of stoichiometric flux drawn from a precursor pool; see Eqs. S13, S14 and S18.	$\eta_{a1}=15\%$, $\eta_{a2}=30\%$, $\eta_b=35\%$, $\eta_c=9\%$, $\eta_d=11\%$ (calculated from the values of r_i and $N_{EP_i}^{carbon}$).
$\phi_r, \phi_f, \phi_{BM}$	ϕ_r , ϕ_f , ϕ_{BM} are the proteomic mass fraction of enzymes dedicated to fermentation, respiration, and biomass generation, respectively.	NA

κ_t	A parameter determined by the translation rate, defined as $\kappa_t \equiv k_T \cdot m_{AA} / (\zeta \cdot m_R)$.	$\kappa_t = 1/610 \text{ (s}^{-1}\text{)}$ (calculated from the values of k_T , ζ and m_R).
J_{BM}	The carbon flux of biomass production; an extensive variable.	See Eq. S10.
J_E	The energy demand for cell growth, expressed as the stoichiometric energy flux in ATP; an extensive variable.	See Eq. S25.
$J_E^{(N)}$	The normalized flux of energy demand in ATP; an intensive variable.	$J_E^{(N)} \equiv J_E \cdot m_0 / M_{carbon}$.
r_E, η_E	r_E and η_E are energy coefficients. r_E is the slope of J_E versus J_{BM} ; $\eta_E = r_E \cdot [\sum_i r_i / N_{EP_i}^{carbon}]$.	See Appendix 8.2.
β_i	The stoichiometric coefficient of ATPs in biochemical reactions shown in Figs. 1B and 3E (for <i>E. coli</i>) or Appendix-fig. 5E-F (for yeast and mammalian cells).	$\beta_1=4; \beta_2=3; \beta_3=2; \beta_4=6; \beta_6=1;$ $\beta_{a1}=4; \beta_7=1; \beta_8=2; \beta_9=6 \text{ (E.coli)}$ $\beta_1=5; \beta_2=1; \beta_3=5; \beta_4=7.5;$ $\beta_6=2.5; \beta_{a1}=5 \text{ (eukaryotic cells)}$ (Neidhardt et al., 1990; Sauer et al., 2004)
$\beta_r^{(A)}, \beta_f^{(A)}$	$\beta_r^{(A)}$ and $\beta_f^{(A)}$ are the stoichiometric coefficients of ATP production per glucose in respiration and fermentation, respectively.	$\beta_r^{(A)}=26, \beta_f^{(A)}=12 \text{ (E.coli)}$; $\beta_r^{(A)}=32, \beta_f^{(A)}=2 \text{ (eukaryotic cells)}$ (Neidhardt et al., 1990).
$J_r^{(E)}, J_f^{(E)}$	$J_r^{(E)}$ and $J_f^{(E)}$ are normalized energy fluxes of respiration and fermentation, intensive variables.	$J_r^{(E)} \equiv \frac{\beta_r^{(A)}}{2} \cdot J_r^{(N)}$; $J_f^{(E)} \equiv \frac{\beta_f^{(A)}}{2} \cdot J_f^{(N)}$.
$\varepsilon_r, \varepsilon_f$ $\varepsilon_r^{(dt)}, \varepsilon_f^{(dt)}$	ε_r (or $\varepsilon_r^{(dt)}$) and ε_f (or $\varepsilon_f^{(dt)}$) are the proteome efficiencies for energy biogenesis in the respiration and fermentation pathways: $\varepsilon_r \equiv J_r^{(E)} / \phi_r$ and $\varepsilon_f \equiv J_f^{(E)} / \phi_f$.	Calculated from the values of κ_A , κ_t , $\beta_r^{(A)}$ and $\beta_f^{(A)}$ with Eq. S132 and S161.
φ	φ is an energy demand coefficient, defined in Eq. S33 and mainly determined by η_E .	Calculated from the values of η_E , β_i , η_i with Eq. S33. See Appendix 8.2.
ψ, ψ_{dt}	ψ^{-1} (or ψ_{dt}^{-1}) is the proteome efficiency for biomass generation in the biomass pathway, with $\psi^{-1} \equiv \lambda / \phi_{BM}$.	Calculated from the values of η_i , κ_A , κ_t , Ω , κ_t with Eqs. S133 and S162.
$\kappa_r^{(A)}, \kappa_f^{(A)}$	$\kappa_r^{(A)}$ and $\kappa_f^{(A)}$ are parameters defined as $\kappa_r^{(A)} \equiv \left[\frac{1}{\kappa_1} + \frac{2}{\kappa_2} + \frac{2}{\kappa_3} + \frac{2}{\kappa_4} \right]^{-1}$ and $\kappa_f^{(A)} \equiv \left[\frac{1}{\kappa_1} + \frac{2}{\kappa_2} + \frac{2}{\kappa_6} \right]^{-1}$.	Calculated from the values of κ_i .
Ω	Ω is a composite parameter defined as $\Omega \equiv 1 / \kappa_t + \sum_i^{a1,a2,b,c,d} \eta_i / \kappa_i$.	See Appendix 8.2.
$\kappa_{glucose}^{(ST)}, \kappa_{lactose}^{(ST)}$	The substrate quality of glucose or lactose at saturated concentration.	Calculated using Eq. S27 and the approximation used in Eq. S20.
Δ	Δ is a function of κ_A defined as $\Delta(\kappa_A) \equiv \varepsilon_f(\kappa_A) / \varepsilon_r(\kappa_A)$.	$\Delta \equiv \varepsilon_f / \varepsilon_r$.
$\kappa_A^{(C)}$	The critical value of κ_A which satisfy $\Delta(\kappa_A)=1$ and thus $\varepsilon_f(\kappa_A)=\varepsilon_r(\kappa_A)$; See Eqs. S42 (for <i>E. coli</i>) and S176 (for yeast and mammalian cells).	Calculated from the values of β_i and κ_i with Eq. S42.
λ_C	The critical growth rate at the transition point: $\lambda_C \equiv \lambda(\kappa_A^{(C)})$; See Eqs. S43 and S177.	Calculated from the values of ϕ_{max} , φ , β_i , κ_i , $\kappa_A^{(C)}$, Ω , η_i with Eqs. S43, S32 and S162.
θ	The Heaviside step function.	NA
$J_{acetate}, J_{CO_2,r}$	$J_{acetate}$ and $J_{CO_2,r}$ are the stoichiometric fluxes of acetate from the fermentation pathway and CO2 from the respiration pathway; extensive variables.	$J_{acetate} = J_f$; $J_{CO_2,r} = 3 \cdot J_{CO_2,r}$. See Appendix 8.1 and Eq. S158.
$J_{acetate}^{(M)}, J_{CO_2,r}^{(M)}$	$J_{acetate}^{(M)}$ and $J_{CO_2,r}^{(M)}$ are the fluxes of $J_{acetate}$ and $J_{CO_2,r}$ (per biomass) in the unit of mM/OD600/h, which are measurable in experiment. Intensive variables.	$J_{acetate}^{(M)} \approx 2 \cdot J_f^{(N)}$; $J_{CO_2,r}^{(M)} \approx 6 \cdot J_r^{(N)}$. See Appendix 8.1 and Eq. S160.
κ_A^{max}	The maximum value of κ_A available across different Group A carbon sources.	Approximated by the max κ_A across Group A carbon sources, calculated with Eq. S27 and the approximation used in Eq. S20.
λ_{max}	The population cell growth rate for the maximum value of κ_A : $\lambda_{max} = \lambda(\kappa_A^{max})$.	Calculated from the maximum of Eq. 36 with the values of β_i , κ_i , κ_A^{max} , φ , Ω , κ_t , and Eqs. S32, S132, S161 and S162.
$\mathcal{N}(\mu, \sigma^2)$	A Gaussian distribution with a mean of μ and a standard deviation of σ .	The probability density function is $f(x) = \frac{1}{\sigma\sqrt{2\pi}} e^{-\frac{1}{2}\left(\frac{x-\mu}{\sigma}\right)^2}$.
$\mu_{\lambda_C}, \sigma_{\lambda_C}$	μ_{λ_C} and σ_{λ_C} are the mean and standard deviation of λ_C , respectively.	μ_{λ_C} is approximated by the deterministic value of λ_C ; see Appendix 2.3 for σ_{λ_C} settings. See Appendix 8.2 for the values.
erf	The error function in mathematics.	$\text{erf}(x) = \frac{2}{\sqrt{\pi}} \int_0^x \exp(-t^2) dt$
ϕ_Z	The proteomic mass fraction of useless proteins encoded by the LacZ gene.	See Appendix 3.1.
w	An energy dissipation coefficient.	See Appendix 3.2.
w_0	The maintenance energy coefficient.	$w_0=0$ or $2.5 \text{ (h}^{-1}\text{)}$ as specified in Figs.3-4, S2-S3. See Appendices 3.3 and 8.2.
l	l is the inhibition coefficient such that $(1+l)^{-1}$ represents the translation efficiency.	See Appendices 3.3 and 8.2.

$(2\mu\text{m Cm})$; $(4\mu\text{m Cm})$; $l_{w_0=0}^{(2\mu\text{m Cm})}$; $l_{w_0=0}^{(4\mu\text{m Cm})}$; $(8\mu\text{m Cm})$; $(2\mu\text{m Cm})$; $l_{w_0=0}^{(8\mu\text{m Cm})}$; $l_{w_0=2.5}^{(2\mu\text{m Cm})}$; $(4\mu\text{m Cm})$; $(8\mu\text{m Cm})$; $l_{w_0=2.5}^{(4\mu\text{m Cm})}$; $l_{w_0=2.5}^{(8\mu\text{m Cm})}$	The values for l in the cases with $2\mu\text{m}$, $4\mu\text{m}$, or $8\mu\text{m}$ of chloramphenicol and the maintenance energy coefficient w_0 chosen as 0 or 2.5 (h^{-1}).	$l_{w_0=0}^{(2\mu\text{m Cm})}=1.15$; $l_{w_0=0}^{(4\mu\text{m Cm})}=2.33$; $l_{w_0=0}^{(8\mu\text{m Cm})}=6.25$; $l_{w_0=2.5}^{(2\mu\text{m Cm})}=1.05$; $l_{w_0=2.5}^{(4\mu\text{m Cm})}=2.00$; $l_{w_0=2.5}^{(8\mu\text{m Cm})}=5.40$. See Appendix 8.2.
κ_{py}	The substrate quality of pyruvate; see Eq. S89.	Calculated from the values of k_A^{cat} , m_{E_A} , m_0 , $r_{protein}$, r_{carbon} , K_A and the external concentration of pyruvate [py].
$\beta_r^{(py)}$, $\beta_f^{(py)}$	$\beta_r^{(py)}$ and $\beta_f^{(py)}$ are the stoichiometric coefficients of ATP production per pyruvate in respiration and fermentation, respectively.	$\beta_r^{(A)}=10$; $\beta_f^{(A)}=3$. (Neidhardt et al., 1990).
$J_r^{(E,py)}$, $J_f^{(E,py)}$	$J_r^{(E,py)}$ and $J_f^{(E,py)}$ are the normalized energy fluxes of respiration and fermentation for pyruvate utilization; intensive variables.	The corresponding variables of $J_r^{(E)}$ and $J_f^{(E)}$ in the case of pyruvate utilization.
$\varepsilon_r^{(py)}$, $\varepsilon_f^{(py)}$	$\varepsilon_r^{(py)}$ and $\varepsilon_f^{(py)}$ are the proteome efficiencies for energy biogenesis using pyruvate in the respiration and fermentation pathways.	The corresponding variables of ε_r and ε_f in the case of pyruvate utilization.
Ω'_{Gg}	Ω'_{Gg} is a composite parameter defined as $\Omega'_{Gg} \equiv (\eta_b + \eta_c)/\kappa_B + \eta_{a1}/\kappa_9$.	See Appendix 8.2.
ψ_{py} , φ_{py} , $\kappa_{py}^{(ST)}$, $\kappa_{py}^{(C)}$, $\kappa_{py}^{(C)}$, $\lambda_{max}^{(py)}$	ψ_{py} , φ_{py} , $\kappa_{py}^{(ST)}$, $\kappa_{py}^{(C)}$ and $\lambda_{max}^{(py)}$ are the corresponding variables/parameters of ψ , φ , κ_A^{max} , $\kappa_A^{(C)}$ and λ_{max} in the case of pyruvate utilization.	See Appendices 4.1 and 8.2.
$\lambda_C^{(py)}$, $\mu_{\lambda_C}^{(py)}$, $\sigma_{\lambda_C}^{(py)}$	$\lambda_C^{(py)}$, $\mu_{\lambda_C}^{(py)}$ and $\sigma_{\lambda_C}^{(py)}$ are the corresponding variables/parameters of λ_C , μ_{λ_C} and σ_{λ_C} in the case of pyruvate utilization.	See Appendices 4.1 and 8.2.
$N_{P_i}^{carbon}$	The number of carbon atoms in a molecule of Pool i .	The value of $N_{P_i}^{carbon}$ is approximated by $N_{EP_i}^{carbon}$ (Eq. S107).
$\kappa_i^{(21AA)}$	The substrate quality of the external supplied amino acids identical to those in Pool i .	See Appendices 4.2 and 8.2.
Ω_{21AA}	Ω_{21AA} is a composite parameter defined as $\Omega_{21AA} \equiv 1/\kappa_t + \eta_{a1}/\kappa_{a1} + \sum_i^{a2,b,c,d} \eta_i/\kappa_i^{(21AA)}$.	See Appendices 4.2 and 8.2.
ψ_{21AA} , φ_{21AA} , $\lambda_{max}^{(21AA)}$, $\lambda_C^{(21AA)}$, $\mu_{\lambda_C}^{(21AA)}$, $\sigma_{\lambda_C}^{(21AA)}$	ψ_{21AA} , φ_{21AA} , $\lambda_{max}^{(21AA)}$, $\lambda_C^{(21AA)}$, $\mu_{\lambda_C}^{(21AA)}$ and $\sigma_{\lambda_C}^{(21AA)}$ are the corresponding variables/parameters of ψ , φ , λ_{max} , λ_C , μ_{λ_C} and σ_{λ_C} in the case of a Group A carbon source is mixed with 21 types of amino acids at saturated concentrations.	See Appendices 4.2 and 8.2.
Ω_{7AA} , φ_{7AA} , $\mu_{\lambda_C}^{(7AA)}$, $\sigma_{\lambda_C}^{(7AA)}$	Ω_{7AA} , φ_{7AA} , $\mu_{\lambda_C}^{(7AA)}$ and $\sigma_{\lambda_C}^{(7AA)}$ are the corresponding parameters of Ω , φ , μ_{λ_C} and σ_{λ_C} in the case of a Group A carbon source is mixed with 7 types of amino acids.	See Appendices 4.2 and 8.2.
$J_{in}^{(N)}$, ϑ	$J_{in}^{(N)}$ is the normalized stoichiometric influx of a Group A carbon source (Eq. S136). ϑ is a parameter defined as $\vartheta = \eta_{a1} + \eta_c + (\eta_{a2} + \eta_b + \eta_d)/2$ for the model shown in Fig. 1B.	See Appendix 6.3
χ_{ext} , χ_{int} , χ_{tot}	χ_{ext} , χ_{int} and χ_{tot} are the level of extrinsic noise, intrinsic noise and total noise in a system.	See Appendix 7.1
$\mu_{k_i^{cat}}$, $\sigma_{k_i^{cat}}$, $\mu_{1/k_i^{cat}}$, $\sigma_{1/k_i^{cat}}$, $\mu'_{1/k_i^{cat}}$, $\sigma'_{1/k_i^{cat}}$	$\mu_{k_i^{cat}}$ and $\sigma_{k_i^{cat}}$ are the mean and standard deviation of k_i^{cat} ; $\mu_{1/k_i^{cat}}$ (or $\mu'_{1/k_i^{cat}}$) and $\sigma_{1/k_i^{cat}}$ (or $\sigma'_{1/k_i^{cat}}$) are the mean and standard deviation of $1/k_i^{cat}$. See Appendix 7.1.	$\mu_{k_i^{cat}}$ is approximated by the deterministic value of k_i^{cat} . The CV of k_i^{cat} is set to 25%. $\mu_{1/k_i^{cat}} \approx 1/\mu_{k_i^{cat}}$; $\sigma_{1/k_i^{cat}}/\mu_{1/k_i^{cat}} \approx \sigma_{k_i^{cat}}/\mu_{k_i^{cat}}$.
$IG(x; \mu, \zeta)$	The inverse Gaussian (IG) distribution: variable $x>0$ with parameters μ and ζ . See Eq. S142.	The probability density function is $\sqrt{\frac{\zeta}{2\pi x^3}} \exp\left(-\frac{\zeta(x-\mu)^2}{2\mu^2 x}\right)$.
$IOG(x; \mu, \zeta)$	The positive inverse of Gaussian (IOG) distribution: variable $x>0$ with parameters μ and ζ . See Eq. S140 and Appendix 7.1.	The probability density function is $\sqrt{\frac{\zeta}{2\pi x^4}} \exp\left(-\frac{\zeta(x-\mu)^2}{2\mu^2 x^2}\right)$.
$\zeta_{1/k_i^{cat}}$, $\zeta'_{1/k_i^{cat}}$	Distributional parameters of $1/k_i^{cat}$ corresponding to ζ in an IG or IOG distribution.	See Appendix 7.1
$G(k)$	The characteristic function of IG distribution. See Eq. S147.	$G(k) = \int_{-\infty}^{\infty} e^{ikx} \cdot IG(x; \mu, \zeta) dx$
X_i , α_i , θ , T_θ , $\Gamma_i(t)$	X_i , α_i , θ and $\Gamma_i(t)$ are variables and parameters used to calculate the first passage time T_θ of a stochastic process that mimics the duration of an enzyme to finishing a catalytic job.	See Appendix 7.1.
γ_i , ε , μ_ε , σ_ε	γ_i is a real number; ε is a variable defined as $\varepsilon \equiv \sum_{i=1}^n \gamma_i/k_{cat}^i$; μ_ε and σ_ε are the mean and standard deviation of ε .	See Eq. S153 and Appendix 7.1.
μ_{κ_i} , σ_{κ_i} , μ_{1/κ_i} , σ_{1/κ_i}	μ_{κ_i} and σ_{κ_i} are the mean and standard deviation of κ_i ; μ_{1/κ_i} and σ_{1/κ_i} are the mean and standard deviation of $1/\kappa_i$.	See Eq. S154 and Appendices 7.1 and 8.2.
λ_r , λ_f , μ_{λ_r} , σ_{λ_r} , μ_{λ_f} , σ_{λ_f} , ρ_{rf}	λ_r and λ_f are the growth rates when cells choose respiration or fermentation; μ_{λ_r} , μ_{λ_f} and σ_{λ_r} , σ_{λ_f} are the means and standard deviations of λ_r and λ_f ; ρ_{rf} is the correlation of λ_r and λ_f .	See Eq. S36 and Appendices 7.1 and 8.2.
$\lambda_{succinate}^{(21AA)}$, $\lambda_{acetate}^{(21AA)}$, $\mu_{\lambda_{succinate}^{(21AA)}}$, $\mu_{\lambda_{acetate}^{(21AA)}}$, $\sigma_{\lambda_{succinate}^{(21AA)}}$, $\sigma_{\lambda_{acetate}^{(21AA)}}$	$\lambda_{succinate}^{(21AA)}$ and $\lambda_{acetate}^{(21AA)}$ are the growth rates for succinate mixed with 21AA or acetate as the sole carbon source; $\mu_{\lambda_{succinate}^{(21AA)}}$, $\mu_{\lambda_{acetate}^{(21AA)}}$ and $\sigma_{\lambda_{succinate}^{(21AA)}}$, $\sigma_{\lambda_{acetate}^{(21AA)}}$ are the means and standard deviations of $\lambda_{succinate}^{(21AA)}$ and $\lambda_{acetate}^{(21AA)}$.	See Appendix 8.2.

ϕ_{MT}, κ_{MT}	ϕ_{MT} and κ_{MT} are the proteomic mass fraction of the enzymes and the effective substrate quality of related metabolites in the mitochondria for yeast and mammalian cells, respectively.	NA
Pr_f	The proportion of ATP generated from fermentation: $Pr_f \equiv \frac{j_f^{(E)}}{j_f^{(E)} + j_r^{(E)}}$.	See Eqs. S180, S189 and Appendix 9.
$\bar{\Delta}$	The proteome efficiency difference between respiration and fermentation: $\bar{\Delta} \equiv 1/\varepsilon_r - 1/\varepsilon_f$.	See Eqs. S181, S187 and Appendix 9.
$\mu_{\varepsilon_r}, \mu_{\varepsilon_f}, \mu_{1/\varepsilon_r}, \mu_{1/\varepsilon_f}$	$\mu_{\varepsilon_r}, \mu_{\varepsilon_f}, \mu_{1/\varepsilon_r}$ and μ_{1/ε_f} are the mean values of $\varepsilon_r, \varepsilon_f, 1/\varepsilon_r$ and $1/\varepsilon_f$, respectively.	See Eqs. S182-S184 and Appendix 9.
$\sigma_{\varepsilon_r}, \sigma_{\varepsilon_f}, \sigma_{1/\varepsilon_r}, \sigma_{1/\varepsilon_f}$	$\sigma_{\varepsilon_r}, \sigma_{\varepsilon_f}, \sigma_{1/\varepsilon_r}$ and σ_{1/ε_f} are the standard deviations of $\varepsilon_r, \varepsilon_f, 1/\varepsilon_r$ and $1/\varepsilon_f$, respectively.	See Eqs. S182, S185 and Appendix 9.
$\chi_{\varepsilon_r}, \chi_{\varepsilon_f}, \chi_{1/\varepsilon_r}, \chi_{1/\varepsilon_f}$	$\chi_{\varepsilon_r}, \chi_{\varepsilon_f}, \chi_{1/\varepsilon_r}$ and χ_{1/ε_f} are the coefficients of variation of $\varepsilon_r, \varepsilon_f, 1/\varepsilon_r$ and $1/\varepsilon_f$, respectively.	See Eqs. S185-S186 and Appendix 9.
$\mu_{\bar{\Delta}}, \sigma_{\bar{\Delta}}$	$\mu_{\bar{\Delta}}$ and $\sigma_{\bar{\Delta}}$ are the mean and standard deviation of $\bar{\Delta}$, respectively.	See Eqs. S187-S188 and Appendix 9.
$\langle \varepsilon_r \rangle, \langle \varepsilon_f \rangle$	$\langle \varepsilon_r \rangle$ and $\langle \varepsilon_f \rangle$ are the population-averaged values of ε_r and ε_f , respectively.	Measurable from experiments. See Eqs. S183-S184 and Appendix 9.

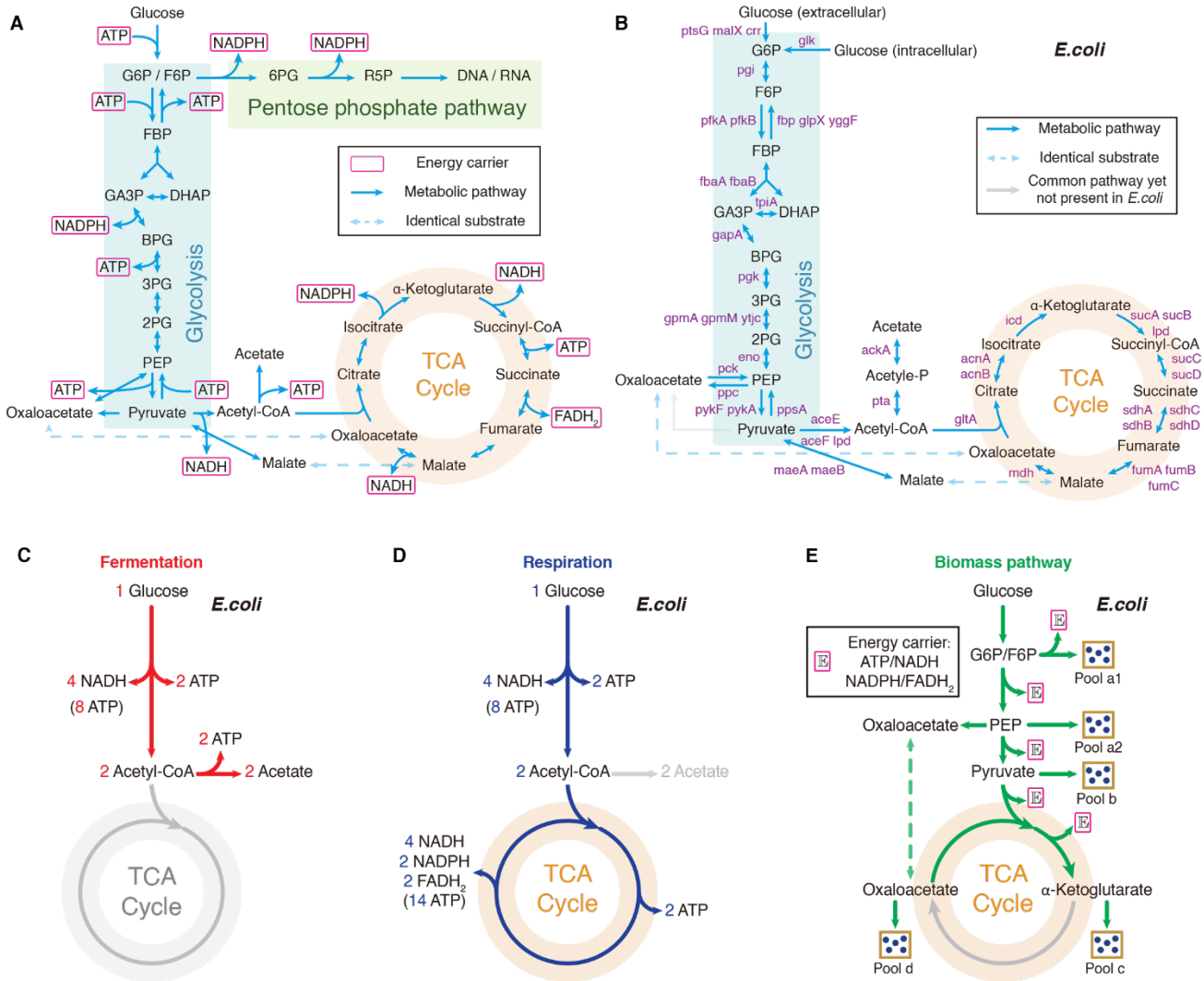
* Parameter settings for yeast and mammalian cells are specifically labeled as “eukaryotic cells”.

**“NA” represents “Not applicable”.

† Extensive variables scale with the size of the cell population.

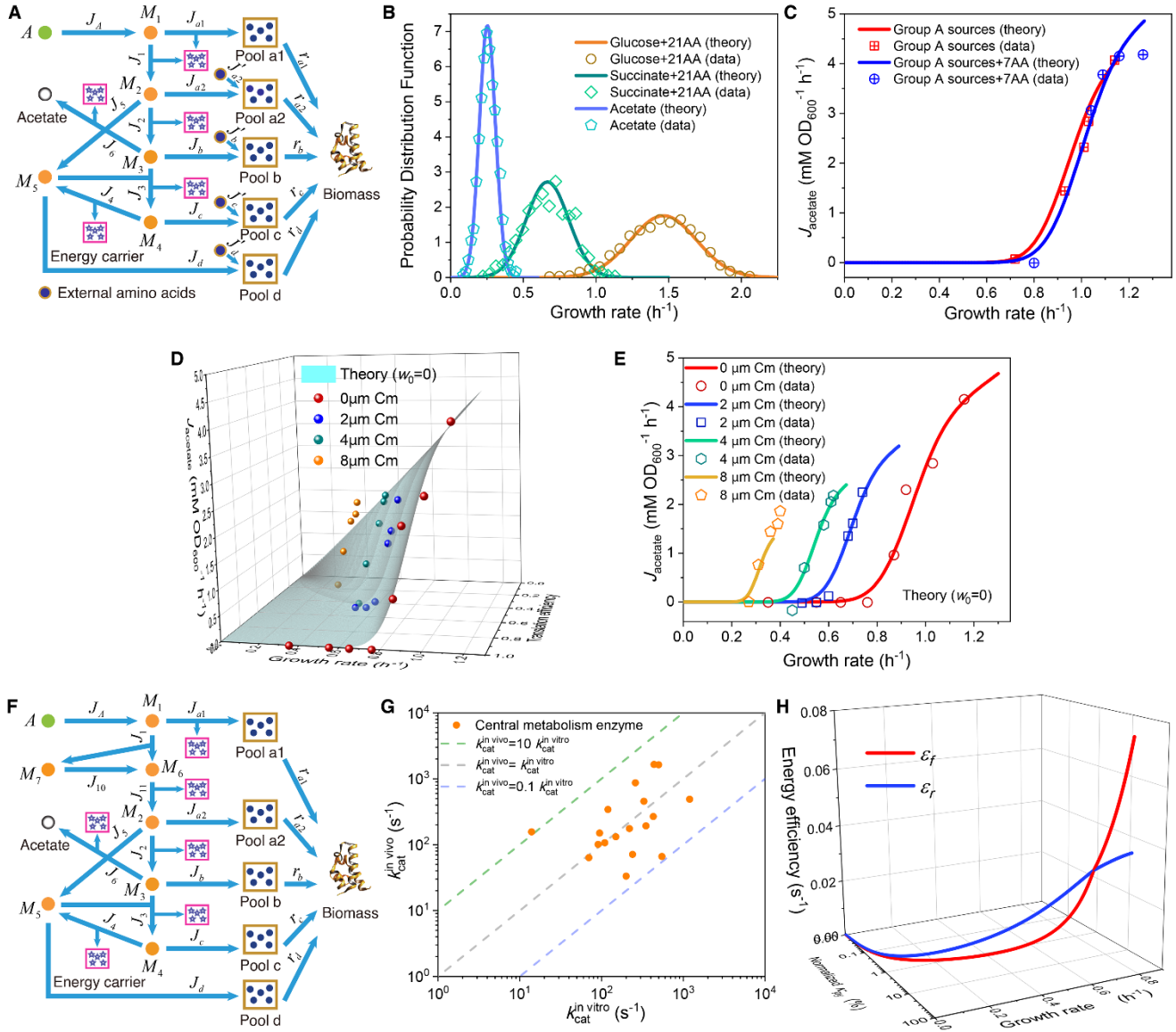
‡ Intensive variables are scale-invariant with respect to the cell population.

Appendix Figures



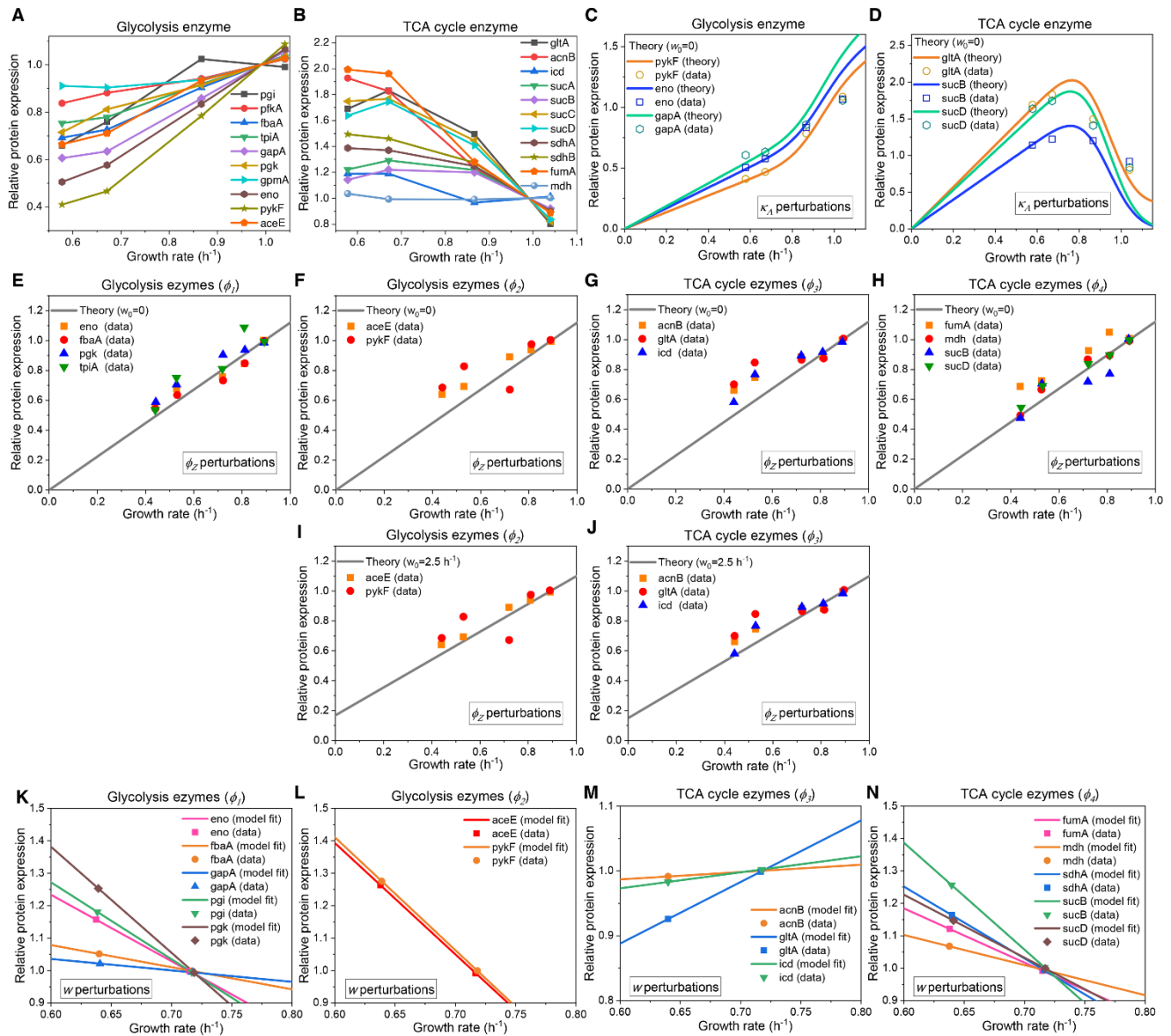
Appendix-figure 1. Central metabolic network and carbon utilization pathways of *E. coli*.

(A) Energy biogenesis details in the central metabolic network. In *E. coli*, NADPH and NADH are interconvertible (Sauer et al., 2004), and all energy carriers can be converted to ATP through ADP phosphorylation. The conversion factors are: NADH = 2ATP, NADPH = 2ATP, FADH₂ = 1ATP (Neidhardt et al., 1990). (B) Relevant genes encoding enzymes in the central metabolic network of *E. coli*. (C-E) Three independent fates of glucose metabolism in *E. coli*. (C) For energy biogenesis through fermentation, a molecule of glucose generates 12 ATPs. (D) For energy biogenesis via respiration, a molecule of glucose generates 26 ATPs. (E) For biomass synthesis, glucose is converted into precursors of biomass. Note that biomass synthesis is accompanied by ATP production (see Appendix 2.1).



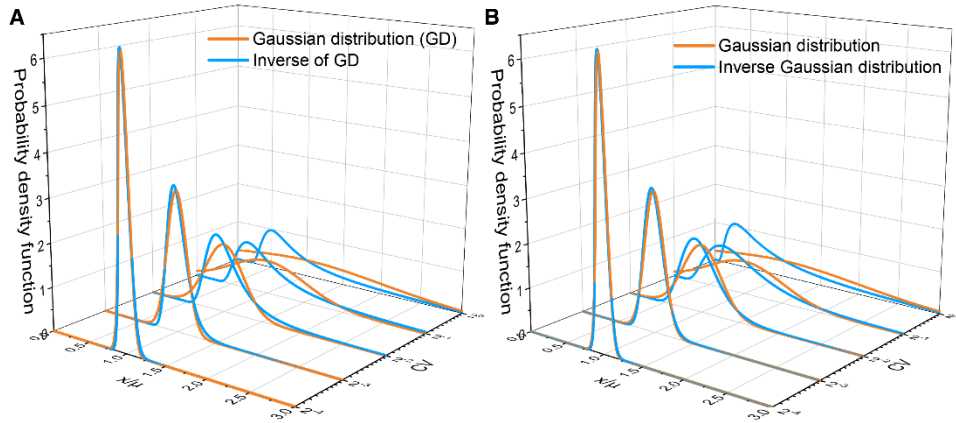
Appendix-figure 2. Model and results for experimental comparison of *E. coli*. (A-C) Model analysis for carbon utilization in mixtures with amino acids. (A) Coarse-grained model for the case of a Group A carbon source mixed with extracellular amino acids. (B) Model predictions (Eqs. S157, S164-S165) and single-cell reference experimental results (Wallden et al., 2016) showing growth rate distributions for *E. coli* in three culturing conditions. (C) Comparison of the growth rate-fermentation flux relation for *E. coli* in Group A carbon sources between minimal media and enriched media (those with 7AA). (D-E) Influence of translation inhibition on overflow metabolism in *E. coli*. (D) A 3D plot illustrating the relations among fermentation flux, growth rate, and translation efficiency (Eqs. 79 and S160). (E) Growth rate dependence of acetate excretion rate as κ_A varies, with each fixed dose of Cm. Translation efficiency is tuned by the dose of Cm, and the maintenance coefficient is set to 0 (i.e., $w_0 = 0$). (F) Coarse-grained model for Group A carbon source utilization, which includes more details to compare

with experiments. **(G)** Comparison of in vivo and in vitro catalytic rates for enzymes of *E. coli* within glycolysis and the TCA cycle (see Appendix-table 1 for details). **(H)** The proteome efficiencies for energy biogenesis in the respiration and fermentation pathways vary with growth rate as functions of the substrate quality of pyruvate (Eqs. S93 and S96).

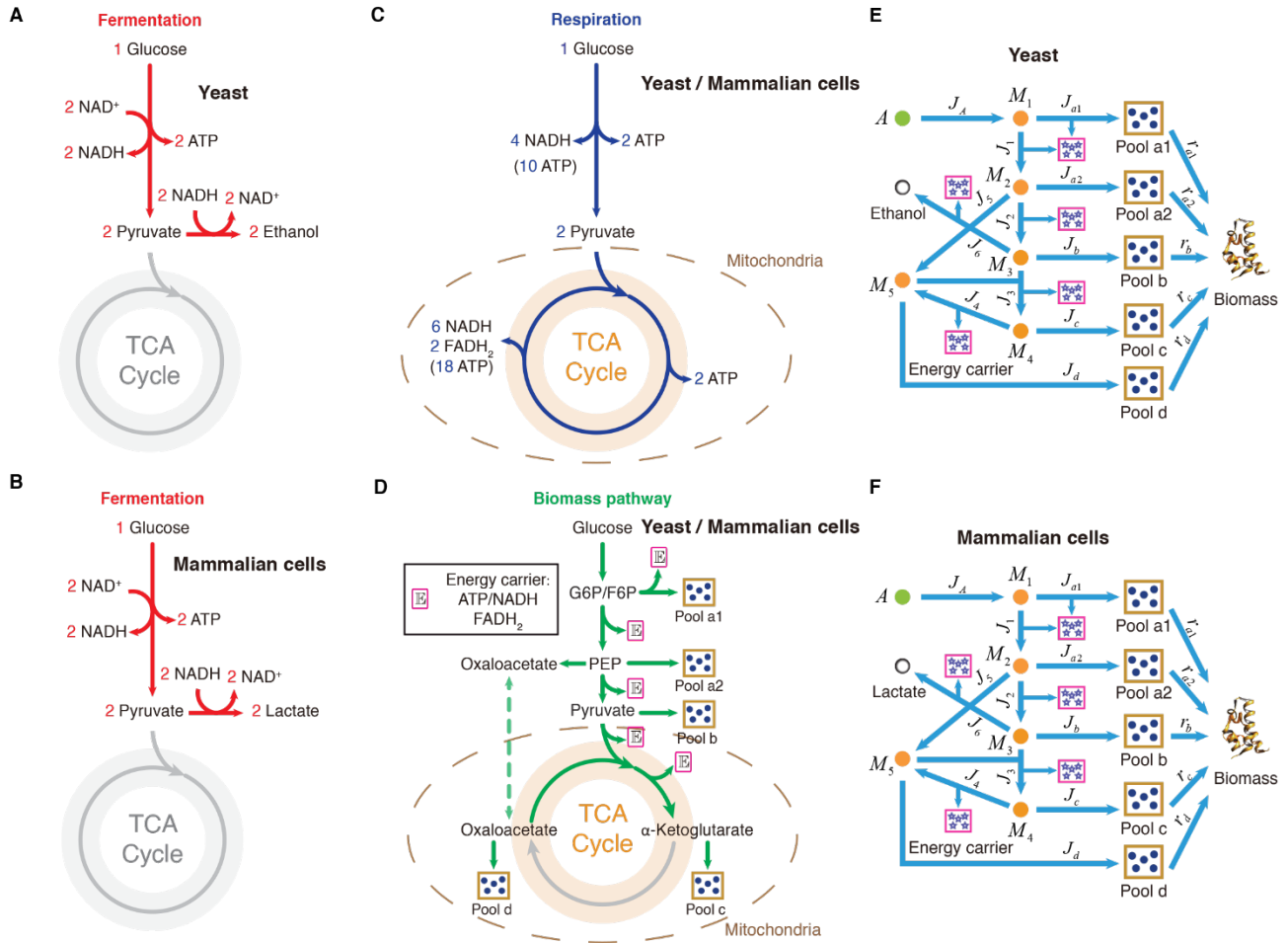


Appendix-figure 3. Relative protein expression of central metabolic enzymes in *E. coli* under various types of perturbations. (A-D) Relative protein expression under κ_A perturbation. (A) Experimental data (Hui et al., 2015) for the catalytic enzymes at each step of glycolysis. (B) Experimental data (Hui et al., 2015) for the catalytic enzymes at each step of the TCA cycle. (C) Model predictions (Eq. S118, with $w_0 = 0$) and experimental data (Hui et al., 2015) for representative glycolytic genes. (D) Model predictions (Eq. S118, with $w_0 = 0$) and experimental data (Hui et al., 2015) for representative genes from the TCA cycle. (E-J) Relative protein expression under ϕ_Z perturbation. (E, F, I) Model predictions and experimental data (Basan et al., 2015) for representative glycolytic genes. (G, H, J) Model predictions and experimental data (Basan et al., 2015) for representative genes from the TCA cycle. (E-H) Results of ϕ_Z

perturbation with $w_0 = 0$ (Eq. S120). **(I-J)** Results of ϕ_z perturbation with $w_0 = 2.5$ (h^{-1}) (Eq. S121). **(K-N)** Relative protein expression upon energy dissipation. **(K-L)** Model fits (Eqs. S127 and S123) and experimental data (Basan et al., 2015) for representative glycolytic genes. **(M-N)** Model fits (Eqs. S127 and S123) and experimental data (Basan et al., 2015) for representative genes from the TCA cycle.



Appendix-figure 4. Asymptotic distributions of inverse Gaussian distribution and the inverse of Gaussian distribution. (A) Comparison between the inverse of Gaussian distribution and the corresponding Gaussian distribution for various values of the coefficient of variation (CV) (Eqs. S140 and S145). (B) Comparison between the inverse Gaussian distribution and the corresponding Gaussian distribution for various values of CV (Eqs. S142 and S146). Both the inverse Gaussian distribution and the inverse of Gaussian distribution converge to Gaussian distributions when CV is small.



Appendix-figure 5. Carbon utilization in yeast and mammalian cells. (A-D) Three independent fates of glucose metabolism in yeast and mammalian cells. (A-B) For energy biogenesis through fermentation, one molecule of glucose generates 2 ATPs. (C) For energy biogenesis through respiration, one molecule of glucose generates 32 ATPs. (D) For biomass synthesis, glucose is converted into biomass precursors, with ATP produced as a byproduct. In yeast and mammalian cells, the energy stored in NADH and FADH₂ converts ADP into ATP in the mitochondria, with higher conversion factors than in *E. coli*: NADH = 2.5 ATP, FADH₂ = 1.5 ATP (Nelson et al., 2008). (E) Coarse-grained model for Group A carbon source utilization in yeast. (F) Coarse-grained model for Group A carbon source utilization in mammalian cells.

Appendix References

- Bagamery, L.E., Justman, Q.A., Garner, E.C., and Murray, A.W. (2020). A putative bet-hedging strategy buffers budding yeast against environmental instability. *Current Biology* 30, 4563-4578.
- Bartman, C.R., Weilandt, D.R., Shen, Y., Lee, W.D., Han, Y., TeSlaa, T., Jankowski, C.S.R., Samarah, L., Park, N.R., da Silva-Diz, V., et al. (2023). Slow TCA flux and ATP production in primary solid tumours but not metastases. *Nature* 614, 349-357.
- Basan, M., Honda, T., Christodoulou, D., Hörl, M., Chang, Y.-F., Leoncini, E., Mukherjee, A., Okano, H., Taylor, B.R., Silverman, J.M., et al. (2020). A universal trade-off between growth and lag in fluctuating environments. *Nature* 584, 470-474.
- Basan, M., Hui, S., Okano, H., Zhang, Z., Shen, Y., Williamson, J.R., and Hwa, T. (2015). Overflow metabolism in *Escherichia coli* results from efficient proteome allocation. *Nature* 528, 99-104.
- Bennett, B.D., Kimball, E.H., Gao, M., Osterhout, R., Van Dien, S.J., and Rabinowitz, J.D. (2009). Absolute metabolite concentrations and implied enzyme active site occupancy in *Escherichia coli*. *Nature Chemical Biology* 5, 593-599.
- Chen, Y., and Nielsen, J. (2019). Energy metabolism controls phenotypes by protein efficiency and allocation. *Proceedings of the National Academy of Sciences* 116, 17592-17597.
- Dai, X., Zhu, M., Warren, M., Balakrishnan, R., Patsalo, V., Okano, H., Williamson, J.R., Fredrick, K., Wang, Y.-P., and Hwa, T. (2017). Reduction of translating ribosomes enables *Escherichia coli* to maintain elongation rates during slow growth. *Nature Microbiology* 2, 16231.
- Davidi, D., Noor, E., Liebermeister, W., Bar-Even, A., Flamholz, A., Tumbler, K., Barenholz, U., Goldenfeld, M., Shlomi, T., and Milo, R. (2016). Global characterization of in vivo enzyme catalytic rates and their correspondence to in vitro kcat measurements. *Proceedings of the National Academy of Sciences* 113, 3401-3406.
- Donachie, W.D. (1968). Relationship between cell size and time of initiation of DNA replication. *Nature* 219, 1077-1079.
- Duraj, T., García-Romero, N., Carrión-Navarro, J., Madurga, R., Ortiz de Mendivil, A., Prat-Acin, R., Garcia-Cañamaque, L., and Ayuso-Sacido, A. (2021). Beyond the Warburg effect: Oxidative and glycolytic phenotypes coexist within the metabolic heterogeneity of glioblastoma. *Cells* 10, 202.
- Elowitz, M.B., Levine, A.J., Siggia, E.D., and Swain, P.S. (2002). Stochastic gene expression in a single cell. *Science* 297, 1183-1186.
- Folks, J.L., and Chhikara, R.S. (1978). The inverse Gaussian distribution and its statistical application—a review. *Journal of the Royal Statistical Society: Series B* 40, 263-275.
- García-Contreras, R., Vos, P., Westerhoff, H.V., and Booger, F.C. (2012). Why in vivo may not equal in vitro—new effectors revealed by measurement of enzymatic activities under the same in vivo-like assay conditions. *The FEBS Journal* 279, 4145-4159.
- Gillespie, D.T. (2000). The chemical Langevin equation. *The Journal of Chemical Physics* 113, 297-306.

Hanahan, D., and Weinberg, R.A. (2011). Hallmarks of cancer: the next generation. *Cell* *144*, 646-674.

Hensley, C.T., Faubert, B., Yuan, Q., Lev-Cohain, N., Jin, E., Kim, J., Jiang, L., Ko, B., Skelton, R., Loudat, L., et al. (2016). Metabolic heterogeneity in human lung tumors. *Cell* *164*, 681-694.

Holms, H. (1996). Flux analysis and control of the central metabolic pathways in *Escherichia coli*. *FEMS Microbiology Reviews* *19*, 85-116.

Hui, S., Silverman, J.M., Chen, S.S., Erickson, D.W., Basan, M., Wang, J., Hwa, T., and Williamson, J.R. (2015). Quantitative proteomic analysis reveals a simple strategy of global resource allocation in bacteria. *Molecular Systems Biology* *11*, 784.

Kiviet, D.J., Nghe, P., Walker, N., Boulineau, S., Sunderlikova, V., and Tans, S.J. (2014). Stochasticity of metabolism and growth at the single-cell level. *Nature* *514*, 376-379.

Kussell, E., and Leibler, S. (2005). Phenotypic diversity, population growth, and information in fluctuating environments. *Science* *309*, 2075-2078.

Li, S.H.-J., Li, Z., Park, J.O., King, C.G., Rabinowitz, J.D., Wingreen, N.S., and Gitai, Z. (2018). *Escherichia coli* translation strategies differ across carbon, nitrogen and phosphorus limitation conditions. *Nature Microbiology* *3*, 939-947.

Locasale, J.W., and Cantley, L.C. (2010). Altered metabolism in cancer. *BMC Biology* *8*, 88.

Majewski, R., and Domach, M. (1990). Simple constrained-optimization view of acetate overflow in *E. coli*. *Biotechnology and Bioengineering* *35*, 732-738.

Meyer, H.-P., Leist, C., and Fiechter, A. (1984). Acetate formation in continuous culture of *Escherichia coli* K12 D1 on defined and complex media. *Journal of Biotechnology* *1*, 355-358.

Milo, R., and Phillips, R. (2015). *Cell biology by the numbers*. (Garland Science).

Molenaar, D., Van Berlo, R., De Ridder, D., and Teusink, B. (2009). Shifts in growth strategies reflect tradeoffs in cellular economics. *Molecular Systems Biology* *5*, 323.

Mori, M., Schink, S., Erickson, D.W., Gerland, U., and Hwa, T. (2017). Quantifying the benefit of a proteome reserve in fluctuating environments. *Nature Communications* *8*, 1225.

Nanchen, A., Schicker, A., and Sauer, U. (2006). Nonlinear dependency of intracellular fluxes on growth rate in miniaturized continuous cultures of *Escherichia coli*. *Applied and Environmental Microbiology* *72*, 1164-1172.

Neidhardt, F.C. (1996). *Escherichia coli* and *Salmonella*: cellular and molecular biology. (Washington, DC: ASM Press).

Neidhardt, F.C., Ingraham, J.L., and Schaechter, M. (1990). *Physiology of the bacterial cell*. (Sinauer associates).

Nelson, D.L., Lehninger, A.L., and Cox, M.M. (2008). *Lehninger principles of biochemistry*. (Macmillan).

Park, J.O., Rubin, S.A., Xu, Y.-F., Amador-Noguez, D., Fan, J., Shlomi, T., and Rabinowitz, J.D. (2016). Metabolite concentrations, fluxes and free energies imply efficient enzyme usage. *Nature Chemical Biology* *12*, 482-489.

Pavlou, A., Cinquemani, E., Pinel, C., Giordano, N., Mathilde, V.M.-G., Mihalcescu, I., Geiselmann, J., and de Jong, H. (2025). Single-cell data reveal heterogeneity of investment in ribosomes across a bacterial population. *Nature Communications* *16*, 285.

Peebo, K., Valgepea, K., Maser, A., Nahku, R., Adamberg, K., and Vilu, R. (2015). Proteome reallocation in *Escherichia coli* with increasing specific growth rate. *Molecular BioSystems* *11*, 1184-1193.

Sauer, U., Canonaco, F., Heri, S., Perrenoud, A., and Fischer, E. (2004). The soluble and membrane-bound transhydrogenases UdhA and PntAB have divergent functions in NADPH metabolism of *Escherichia coli*. *Journal of Biological Chemistry* *279*, 6613-6619.

Scott, M., Gunderson, C.W., Mateescu, E.M., Zhang, Z., and Hwa, T. (2010). Interdependence of cell growth and gene expression: origins and consequences. *Science* *330*, 1099-1102.

Shen, Y., Dinh, H.V., Cruz, E.R., Chen, Z., Bartman, C.R., Xiao, T., Call, C.M., Ryseck, R.-P., Pratas, J., Weilandt, D., et al. (2024). Mitochondrial ATP generation is more proteome efficient than glycolysis. *Nature Chemical Biology* *20*, 1123-1132.

Shlomi, T., Benyamini, T., Gottlieb, E., Sharan, R., and Ruppin, E. (2011). Genome-scale metabolic modeling elucidates the role of proliferative adaptation in causing the Warburg effect. *PLoS Computational Biology* *7*, e1002018.

Stevenson, K., McVey, A.F., Clark, I.B., Swain, P.S., and Pilizota, T. (2016). General calibration of microbial growth in microplate readers. *Scientific Reports* *6*, 38828.

Towbin, B.D., Korem, Y., Bren, A., Doron, S., Sorek, R., and Alon, U. (2017). Optimality and sub-optimality in a bacterial growth law. *Nature Communications* *8*, 14123.

Valgepea, K., Adamberg, K., Nahku, R., Lahtvee, P.-J., Arike, L., and Vilu, R. (2010). Systems biology approach reveals that overflow metabolism of acetate in *Escherichia coli* is triggered by carbon catabolite repression of acetyl-CoA synthetase. *BMC Systems Biology* *4*, 166.

Van Kampen, N.G. (1992). *Stochastic processes in physics and chemistry*. (Elsevier).

Vander Heiden, M.G., Cantley, L.C., and Thompson, C.B. (2009). Understanding the Warburg effect: the metabolic requirements of cell proliferation. *Science* *324*, 1029-1033.

Varma, A., and Palsson, B.O. (1994). Stoichiometric flux balance models quantitatively predict growth and metabolic by-product secretion in wild-type *Escherichia coli* W3110. *Applied and Environmental Microbiology* *60*, 3724-3731.

Vazquez, A., Liu, J., Zhou, Y., and Oltvai, Z.N. (2010). Catabolic efficiency of aerobic glycolysis: the Warburg effect revisited. *BMC Systems Biology* *4*, 58.

Vazquez, A., and Oltvai, Z.N. (2016). Macromolecular crowding explains overflow metabolism in cells. *Scientific Reports* *6*, 31007.

Wallden, M., Fange, D., Lundius, E.G., Baltekin, Ö., and Elf, J. (2016). The synchronization of replication and division cycles in individual *E. coli* cells. *Cell* *166*, 729-739.

Wang, X., Xia, K., Yang, X., and Tang, C. (2019). Growth strategy of microbes on mixed carbon sources. *Nature Communications* *10*, 1279.

Wehrens, M., Krah, L.H., Towbin, B.D., Hermsen, R., and Tans, S.J. (2023). The interplay between metabolic stochasticity and cAMP-CRP regulation in single E. coli cells. *Cell Reports* 42, 113284.

Zhuang, K., Vemuri, G.N., and Mahadevan, R. (2011). Economics of membrane occupancy and respiration-fermentation. *Molecular Systems Biology* 7, 500.